All-Optical Processing for Terabit/s Wavelength Division Multiplexed systems using Two-Photon Absorption in a Semiconductor Micro-cavity

A thesis submitted in partial fulfillment of the requirements
for the degree of Doctor of Philosophy
(Electronic Engineering)

By
Krzysztof Bondarczuk
B. Eng., M.Sc., MIEEE

School of Electronic Engineering
Dublin City University

Research Supervisor
Prof. Liam P. Barry

March 2009

Declaration

I hereby certify that this material, which I now submit for assessment on the programme of study leading to the award of Doctor of Philosophy is entirely my own work and has not been taken from the work of others save and to the extent that such work has been cited and acknowledged within the text of my work.

Signed: _____

ID No.: _____

Date: _____

Acknowledgments

I would like to take this opportunity to thank all those who supported me in carrying out this work. Firstly, I would like to extend my gratitude to my supervisor Prof. Liam Barry for his guidance throughout my PhD study, and for all the time he has afforded me. His constructive advice and encouragement have made this work possible and enjoyable.

Thanks are also due to Dr Paul Maguire who introduced me into the Radio and Optical Communications Laboratory and guided during the first months of my work. His support and patience helped make this work much more manageable.

Special appreciation is due to Dr Prince Anandarajah for his openhearted assistance and professional advice throughout my time in the lab. Prince's door has always been open and his help very much appreciated.

I am grateful for the cooperation and support from the Semiconductor Optronics Group, University of Dublin, Trinity College, in particular John O'Dowd and Wei-Hua Guo. Many thanks to the technical support staff in the Departament of Electronic Engineering, especially Robert Clare. I would also like to thank the past, present and honorary members of the lab for their positive attitude and stimulating discussions: Ola, Aisling, Jennifer, Brendan, Frank, Eoin, Damien, Marc, Rob, Sylwester, Karl, Doug, Elif, Haymen, Kai, Kevin.

Finally, special thanks have to go to all my friends and family, in particular my parents and Dorota who have helped me to stay on track during this whole journey.

Krzysztof Bondarczuk

January 2009

Abstract

Chromatic Dispersion Monitoring for high-speed WDM systems using Two-Photon Absorption in a Semiconductor Microcavity

Due to continued growth of the Internet and the introduction of new broadband services, such as video-on-demand and mobile telephony, there is a constant requirement for higher speed communications. It is expected that next generation optical communications systems will evolve towards higher capacities by increasing individual line rates rather than the number of wavelength channels. To implement these high-speed optical networks operating at individual channel rates above 100 Gb/s, all-optical processing techniques are necessary. A novel approach based on two-photon absorption nonlinearity within a resonance cavity enhanced structure is explored within this thesis.

High-speed transmission is severely limited by optical impairments requiring frequent and expensive signal regeneration. Chromatic dispersion, considered as one of the main limiting factors, has to be mitigated in order to achieve satisfactory system performance. Continuous monitoring and adaptive compensation of accumulated dispersion fluctuations within a transmission line is likely to be necessary in future systems. Asynchronous all-optical nonlinear techniques can be utilized for high-speed signal temporal characterization and monitoring without the necessity of timing extraction, or optical to electrical conversion. Two-photon absorption within a resonant micro-cavity is an ideal candidate for high-speed transmission line performance monitoring, and can be easily integrated with a dispersion compensation module. The major advantage of using a micro-cavity structure is that the signal is only enhanced over a narrow wavelength range, which is defined by the structure and design of the micro-cavity. In addition, by varying the angle of the incident signal, the resonance response peak of the device can be tuned, thereby isolating individual wavelength channels without the need for external optical filtering.

The novelty of this work lies in the ability of using a single photodetector for sequential monitoring of different wavelength channels, operating at line rates exceeding conventional electrical processing-speeds limits. Experimental work included characterization and testing of the fabricated TPA micro-cavities for 160 Gb/s OTDM chromatic dispersion monitoring. A theoretical model explaining the cavity influence on the nonlinear detection is introduced. The main attribute of this work is the experimental investigation of the performance TPA based micro-cavities laboratory prototype, in a multi-wavelength high-speed optical system. The results have demonstrated the applicability of the TPA micro-cavity to monitor accumulated dispersion fluctuations in future high speed optical networks.

Table of Contents

List of Figures

List of Acronyms

AC	Alternating Current
AMI	Alternate Mark Inversion
ANSI	American National Standards Institute
AP-OOK	Alternating-Phase On-Off Keing
ASE	Amplified Spontaneous Emission
BRB	Bit-Rate-Bandwidth
BW	Transmission bandwidth
CD	Chromatic Dispersion
CRZ	Chirped Return-to-Zero
CSRZ	Carrier-Suppressed Return-to-Zero
CW	Continuous Waveform
DC	Direct Current
DFB-LD	Distributed Feedback Laser Diode
DFF	Dispersion Flattened Fiber
DGD	Differential Group Delay
DPSK	Differential Phase Shift Keying
DQPSK	Differential Quadrature Phase-Shift Keying
DSF	Dispersion Shifted Fiber
DWDM	Dense Wavelength Division Multiplexing
E/O	Electrical-to-Optical
EDFA	Erbium Doped Fiber Amplifiers
FBG	Fiber Bragg Gratings
FDM	Frequency Division Multiplexing
FP	Fabry-Perot
FRAC	Fringe-resolved Autocorrelation
FROG	Frequency Resolved Optical Gating
FSK	Frequency Shift Keying
FSR	Free Spectral Range
FTL	Fourier Transform-Limited
FWHM	Full Width ar Half Maximum
FWM	Four Wave Mixing
GVD	Group Velocity Dispersion
ITU	International Telecommunication Union
LO	Local Oscillator
MBE	Molecular Beam Epitaxy
MUX	Multiplexer
NRZ	Non-Return to Zero
NZ-DSF	Non-Zero Dispersion Shifted Fiber
OA	Optical Amplifier
OAM&P	Operational, Administration, Maintenance and Provisioning
OC	Optical Carriers
ODL	Optical Delay Line

OE	optical-to-electrical
OOK	On-Off Keying
OPM	Optical Performance Monitoring
OR	Optical Regenerator
OSA	Optical Spectrum Analyser
OSNR	Optical Signal to Noise Ratio
OTDM	Optical Time Division Multiplexing
PC	polarization controller
PDSR	Pedestal Suppression Ratio
PLL	Phase-Locked Loop
PMD	Polarisation Mode Dispersion
PPG	Pulse Pattern Generator
PRBS	Pseudo Random Beat Sequence
PSK	Phase Shift Keying
RCE	Resonant Cavity Enhancement
rms	root-mean-square
RZ	Return to Zero
SBS	Stimulated Brillouin Scattering
SDH	Synchronous Digital Hierarchy
SFG	Sum-Frequency Generation
SHG	Second-Harmonic Generation
SI-APD	Silicon Avalanche-Photodiode
SMF	Single Mode Fiber
SNR	Signal-to-Noise Ratio
SOA	Semiconductor Optical Amplifiers
SONET	Synchronous Optical NETwork
SPA	Single-Photon Absorption
SPM	Self Phase Modulation
SRS	Stimulated Raman Scattering
STM	Synchronous Transport Module
STS	Synchronous Transport Signal
TDM	Time Division Multiplexing
TIA	Trans-Impedance Amplifier
TMLL	Tunable Mode Locked Laser
TMM	transfer matrix method
TOAD	Terahertz Optical Asymetric Demultiplexer
TPA	Two Photon Absorption
TUG	Transport Unit Groups
TW-SOA	Travelling Wave Semiconductor Optical Amplifier
VC	Virtual Containers
VCO	Voltage-Controlled Oscillator
VT	Virtual Tributaries
VTG	Virtual Tributaries Groups
WDM	Wavelength Division Multiplexing
XPM	Cross-Phase Modulation

Introduction

Communication is an important part of our life, fundamental for our development. Cultural evolution or technological progress would not be possible without efficient information exchange. The requirement for higher amounts of information transfer stimulates the technological development. Today a physical transport layer of communication networks is realized optically, utilizing light as a carrier for data transmission within an optical fiber.

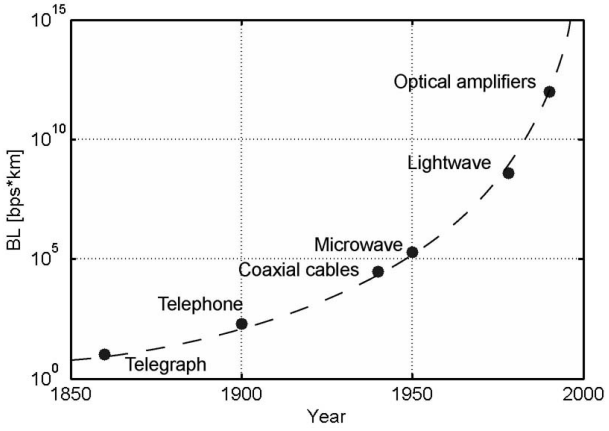

Figure 1 Increase in bit rate–distance product BL during the period 1850 – 2000. Circles point emergence of new technologies.

A commonly used figure of merit for communication systems is the *bit rate-distance product* BL where B is the system operating bit rate and L the repeater spacing. The telecommunication technology development can be viewed on Figure 1, where increase in BL product over 150 years is shown, with points representing the emergence of the most important technologies. It is expected that systems speed will develop following the exponential tendency marked with the dashed line. Current optical systems utilize Time Division Multiplexing (TDM) scheme to pack large amount of voice channels or data traffic into serial sequence of bits operating at line-rates up to 10 Gb/s. Various services are mapped together and multiplexed up utilizing synchronous hierarchies. Fiber capacity can be increased by transmitting a number of serial channels in parallel at different wavelengths, using Wavelength Division Multiplexing (WDM) Scheme. An optical fiber is used as a transmission medium however signal processing is done electrically above the optical/WDM layer. State-of-the-art electronic signal processing currently tops out around 50 Gb/s speeds. To overcome this limit and operate at higher line rates, novel ultra-fast signal processing techniques are required. Promising, intensively investigated techniques are based on nonlinear light interaction with optical materials. Ultra-fast nonlinear all-optical signal processing refers to techniques of optical signal manipulation to achieve processing speeds exceeding electronics limits. These techniques are crucial for operation of ultra-fast optical systems. All-optical techniques can be

utilized for intelligent signal routing through the optical network or real-time signal impairments monitoring. The impairments may occur due to Chromatic Dispersion (CD), Polarisation Mode Dispersion (PMD), nonlinear effects and others. These impairments are difficult to handle in high data-rates systems since their variations due to temporal fluctuation of environmental conditions are no longer negligible. The continuous system performance monitoring and adaptive impairments compensation, preferably on a wavelength-channel basis, will become one of the most challenging tasks for future ultra-fast communication systems.

This work investigates the use of Two Photon Absorption (TPA) in semiconductor material for all-optical signal processing. The thesis is divided into 5 chapters. Chapter 1 discusses the principles of optical communication technology. Development of successive signal multiplexing schemes is discussed according to historical increase in demand for higher capacity systems. Various ultra-short pulse generation techniques and high speed optical fiber transmission are discussed with the main limitations overviewed. Chapter 2 overviews the main optical nonlinearities, and discusses various all-optical signal processing techniques. Nonlinear optical signal performance monitoring is discussed in great detail including signal dispersion, Optical Signal to Noise Ratio (OSNR) and extinction ratio measurements. Chapter 3 introduces the principles of TPA process within a resonance microcavity structure with detailed description and characterization of fabricated devices. Chapter 4 presents experimental results of chromatic dispersion monitoring using TPA microcavity device. A theoretical model is introduced in order to describe pulse overlapping-induced monitoring limit, and cavity influence on the monitoring performance. Device wavelength selectivity is discussed in great detail both theoretically and experimentally for practical applications above 100 Gb/s rates. Chapter 5 summarizes the carried out work and discusses a future outlook of high-speed systems performance monitoring using TPA detection.

The main contribution of this work is a theoretical and experimental investigation into the use of a TPA microcavity photodetector for high-speed, WDM channel performance monitoring. A single device was used to monitor selectively a number of different wavelength channels, operating at line-rates up to 160 Gb/s. A Simulation model describing the cavity monitoring performance for a variety of cavity bandwidths, pulse shapes and durations, and spacing between adjacent wavelength channels was also developed.

CHAPTER 1. Optical Communications

1.1. Introduction

A communications network is a system allowing for information exchange between end users that might be human beings, applications run on a computer or devices such as printer or measurement equipment. A communication network can be divided into access and backbone network sections. Access network links end users premises equipment to the service provider's appropriate counterpart. Backbone network aggregates a huge number of voice or data signal for long-distance transport between access networks. The basic transport layer of a backbone network, also called a physical layer, is realized optically utilizing optical fiber as a transport medium spanning distributed nodes. The amount of information transmitted in optical networks around the globe has increased exponentially since early telecommunication systems, driving a development of the communications technology. Link capacities are successively increased using novel multiplexing schemes and signal processing techniques.

This Chapter discusses the development and current state of the optical communications technology. Section 1.1 overviews multiplexing techniques developed and implemented up to date. Section 1.2 describes main short-pulse generation techniques, having a potential to be used in future high-speed transmission systems. Section 1.3 discusses the principles of optical fiber transmission and main fiber impairments limiting system performance in high capacity optical communication systems.

1.2. Need for Multiplexing

Signal multiplexing refers to the techniques of combining a number of transmitted information channels in a single link. Since the invention of Bell's telephone (1876) [1], the early communication systems used an analog amplitude modulation of an electrical carrier signal, in order to transmit human voice over a twisted pair of copper wire. First multiplexing schemes utilised different carrier frequencies to transmit simultaneously a number of voice channels. This is called Frequency Division Multiplexing and was intensively used till the 1970s. The main problem with the analog systems was an electrical noise that was amplified right along with the signal at every repeater point. This problem was resolved with the digital representation of data signals. A human voice was sampled at 8 kHz rate with each sample encoded using 8 bits resulting in 64 kb/s bit stream. This basic digital channel, known as DS-0, became a fundamental level of Time Division Multiplexing (TDM) hierarchy. TDM multiplexes a number of digital channels in the time domain by dividing the base time slot into the desired number of recurrent sub-slots, one for every

transmitted voice channel. The first TDM-T1 multiplexing hierarchy was introduced in 1962 by AT&T. This however suffered from lack of equipment synchronisation severely limiting transmitted signal bit-rates. The synchronisation became essential with the introduction of new optical-fiber transmission technology in 1980s, where optical fiber was used instead of copper wire in long-haul communication networks. Synchronous optical networking allowed for the realisation of high speed links (up to 10 Gb/s). The following sections overview principles of synchronous multiplexing and subsequent Wavelength Division Multiplexing (WDM) technologies. Possible implementation of novel Optical Time Division Multiplexing (OTDM) and hybrid OTDM/WDM configurations in future telecommunication systems are also discussed.

1.2.1. SONET/SDH

With the introduction of the optical fiber transmission technology American National Standards Institute (ANSI), Bellcore and International Telecommunication Union (ITU) began work on standardisation of novel optical TDM hierarchies. This resulted in synchronous optical multiplexing standards: SONET (1984) in North America and SDH (1988) used in the rest of the world. Synchronization means that each connection achieves a constant bit rate and delay, and may be utilized to allow several service providers to share the same optical fiber, without being affected by each other's traffic load. Only certain integer multiples of 64 kbit/s are possible bit rates, with common data rates listed in Table 1.1. The hierarchies define optical levels called Optical Carriers (OC-n) and adequate electrical level, called the Synchronous Transport Signal (STS-n) in SONET and Synchronous Transport Module (STM-n) in SDH. The order number n can take on values between 1 and 255, but not all values are supported. Both standards are to be used by equipment vendors and service providers at or above a basic optical transmission rate of 51.84 Mb/s (SONET), and 155.52 Mb/s (SDH). Non-synchronous TDM hierarchies are accommodated by dividing STS/STM synchronous payload into smaller components called Virtual Tributaries (VT) in SONET, or Virtual Containers (VC) in SDH. All services below DS-3 rates are transported in the VT/VC structures combined into Virtual Tributaries Groups (VTG) or Transport Unit Groups (TUG) in SONET and SDH respectively. VTG and TUG are then combined and mapped into STS-1 and STM-1 appropriately.

Electrical/Optical Level	Line Rate (Mb/s)	SDH Equivalent
STS/OC-1	51.840	-
STS/OC-3	155.520	STM-1
STS/OC-9	466.560	STM-3
STS/OC-12	622.080	STM-4
STS/OC-18	933.120	STM-6
STS/OC-24	1244.160	STM-8
STS/OC-36	1866.240	STM-13
STS/OC-48	2488.320	STM-16
STS/OC96	4976.640	STM-32
STS/OC-192	9953.280	STM-64

Table 1.1 Common data rates supported by SONET and SDH

The principle of operation is that the electrical multiplexer aggregates various kinds of low bit-rate services, maps them together and multiplexes up using a TDM scheme to a higher bit-rate STS/STM signal. An Electrical-to-Optical (E/O) converter is used to convert the electrical signal into adequate OC level. The link capacity (or speed) is measured in transmitted bits per second (b/s), commonly referred to as the link bandwidth in networking terminology. In principle, the signal bandwidth in optical communication systems can exceed 1 THz due to large carrier bandwidth. Practically the signal bit rate rarely exceeds 10 Gb/s due to limitations imposed by the speed of electronic components. The optical signal is transmitted over optical fiber and then is converted back into electrical signal using Optical-to-Electrical (O/E) conversion and demultiplexed down to the original low bit rate services.

SONET/SDH was very quickly perceived to be an efficient way of deploying optical networks. The main benefits are the firm standards for vendor interoperability, Operational, Administration, Maintenance and Provisioning (OAM&P) feasibility, several ways to support data more effectively, and scaleable speeds from 155 Mb/s to 10 Gb/s, as needed. SONET/SDH was adopted by the large national and international telecommunication carriers for voice and data transmission. The only problem was the speed of electronic processing techniques that limited single-line link speed to approximately 10 Gb/s. This problem was overridden using a multi-wavelength transmission through a single fiber link, significantly increasing the link capacity. The multi-wavelength transmission is discussed in the following section.

1.2.2. WDM

Initially SONET/SDH hierarchies were defined to operate at a single wavelength. This was simply to minimize the number of factors that vendors and operators had to deal with. The capacities were more than sufficient at the time (late 1980s), however with the increased demand for higher capacities a multi-wavelength operation was successively implemented [2][3]. The principal idea was based on the fact that optical fiber can transmit a wide range of optical wavelengths thanks to the wide transmission bandwidth (BW) available. The available BW is largely determined by those wavelengths which experience low losses in the fiber. The fiber losses results from material absorption and Rayleigh scattering. Typical fiber losses are plotted on Figure 1-1.

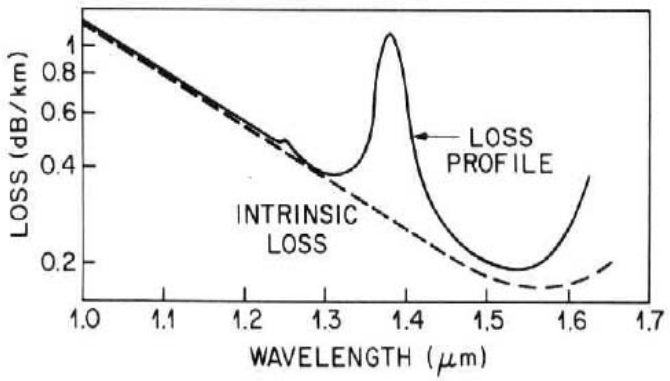

Figure 1-1 Loss in optical fiber

The peak absorption around 1400nm occurs due to OH impurities in glass. This might be removed by using rigorously pure fabrication technology resulting in Low Water Peak Fibers [4]. The fiber bandwidth is divided into number of different bands that various technologies use for transmission. Bands symbols, names and ranges can be viewed in Table 1.2.

Band	Name	Range (nm)
O	Original	1260-1360
E	Extended	1360-1460
S	Short Wavelength	1460-1530
C	Conventional	1530-1565
L	Long Wvelength	1565-1625
U	Ultra-Long Wavelength	1625-1675

Table 1.2 Spectral-band classification scheme

Multi-wavelength operation was a step for better utilization of fiber bandwidth. A number of SONET/SDH signals transmitted over a single fiber link were multiplexed, each operating at different optical wavelength/frequency. This approach called Wavelength Division Multiplexing

(WDM) in principle is identical to Frequency Division Multiplexing (FDM), the only difference is that multiplexing is carried out optically and the carrier frequencies are in the optical range. The first experiments of sending multiple beams of light over long distances in optical fiber were undertaken in the late 1960's [5]. The WDM technology exploded in the 1990s with the invention of wide-band Erbium Doped Fiber Amplifiers (EDFA) [6][7]. EDFA's allowed for aggregated WDM signal re-amplification without demultiplexing and converting back to electronic domain. This was the first all-optical signal processing technique offering a simple and cost-effective possibility to upgrade bandwidth of installed long-distance SONET/SDH transmission links. Most of the deployed systems operate in the C-band in order to take an advantage of EDFA gain bandwidth. The transmission band is divided into a number of narrow-wavelength channels each transmitting separate optical data signal. A typical WDM system configuration is shown in Figure 1.2.

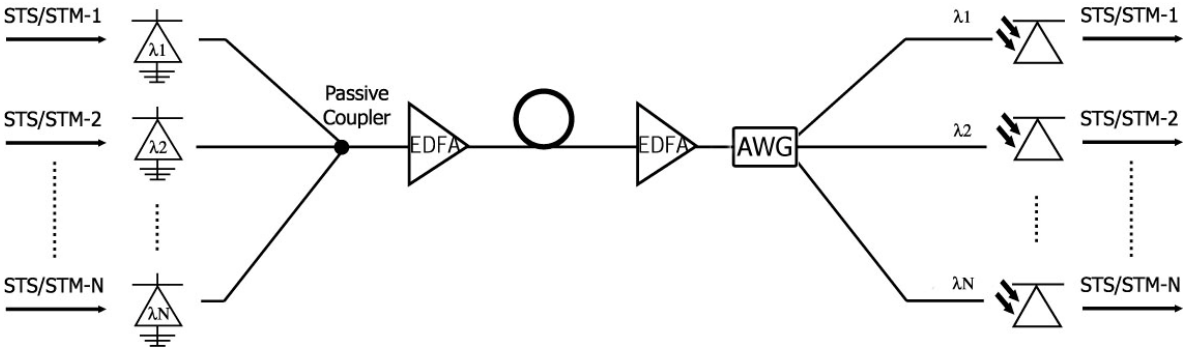

Figure 1-2 Schematic of basic WDM optical communication system

Electrical TDM STS/STM data signals are converted into optical OC signals using a set of directly modulated, or externally modulated lasers. Each laser operates at the appropriate wavelength depending on system transmission band and channel separation. All wavelength channels are combined (multiplexed) using passive optics, thus the multiplexing process does not require electrical power. The WDM multiplexing process is fully transparent to modulation format and repetition rate. The aggregated optical signal is guided in an optical fiber periodically amplified using EDFAs to compensate for the transmission losses. At the receiver side the WDM signal is split into number of copies corresponding to the number of wavelength channels. Commonly Arrayed Waveguide Gratings (AWG) is used [8] capable to separate the all power of the individual wavelength channels. Each channel is then incident on a photodetector to generate the original electrical data.

Continuous effort for denser wavelength channel packing resulted in Dense Wavelength Division Multiplexing (DWDM) technology. DWDM operates in C- and L-bands with channel frequency separations of 12.5GHz, 25GHz, 50GHz, 100GHz. The important advantage of WDM/DWDM is

the capacity of the link that can be scaled by adding additional wavelengths channels. This can be done simply by upgrading the transmitter and receiver without the necessity of replacing the existing fiber infrastructure. This feasibility is called system scalability on demand.

Development of DWDM technology resulted in high systems complexity. This can be visualized assuming a system operating in both C- and L-bands with 50 GHz spacing. In this scenario over 200 different wavelength channels could be transmitted. This requires adequate set of low-jitter transmitters, narrow-band filters and optical detectors. Expensive tunable lasers are also required at each node for channel add/drop operation. Alternative solutions are investigated to obtain high capacities with lower system complexity, easier network management and lower overall expenses. This might be accomplished utilizing Optical Time Division Multiplexing Technology discussed in the following section.

1.2.3. OTDM

Optical link capacity can be increased ether by multiplexing a number of wavelength channels or by increasing channel bit-rates. The main drivers for deployment of higher bit-rates per channel are lower cost per managed bit per km, better bandwidth efficiency, easier management and lower footprint [9][10]. Novel signal processing techniques are required however, in order to overcome slow electronic processing limits, including high speed multiplexing techniques. A potential candidate is Optical Time Division Multiplexing (OTDM) of multiple data streams (time-division-channels) together using passive-time interleaving multiplexers. The OTDM scheme was proposed for the first time in 1988 [11], and in principle is identical to TDM except the multiplexing is carried out optically. Figure 1-3 displays a typical OTDM configuration. Usually a mode-locked or gain-switched laser, generates short pulses and splits the clock signal into the desired number of channels, and subsequently encodes data on each of them. All channels are then time interleaved in optical combiners with appropriate time delays between each channel. In its simplest form OTDM can be realized utilising Return to Zero On-Off Keying (RZ OOK) modulation format however, more advanced schemes such as Differential Phase Shift Keying (DPSK) [12] or Differential Quadrature Phase-Shift Keying (DQPSK) [13] may be applied to improve system performance. Various modulation formats are discussed in section 1.4. Alternatively slotted OTDM can be implemented to improve system flexibility for burst traffic [14]. Unlike a bit-interleaved OTDM in which each user is allocated a particular bit slot in each frame, the slotted scheme uses the whole frame to transmit the user data. Incoming bits are stored and packaged with a header in optical buffers and are then transmitted at a higher output speed.

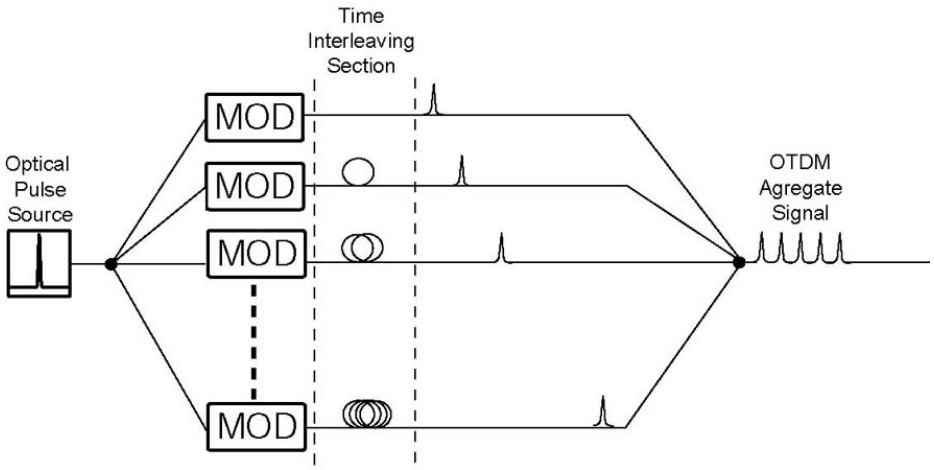

Figure 1-3 Schematic of Optical Time Division Multipexing

The highest OTDM single-line rate reported to date is 1.28Tb/s[15], however this high capacity transmission similarly to the high capacity WDM systems is extremely complex and requires careful system control and design, including high order dispersion effects and fiber nonlinearity compensation. Another solution to achieve high capacity system in a cost-effective manner is a combination of both technologies. OTDM gives a possibility of multiplexing the transmitted signal to the rates above the electronic limits, therefore the number of WDM channel might be reduced, resulting in less system complexity and easier system performance control. This combination of technologies is known as hybrid OTDM/WDM configuration and will be discussed in the following section.

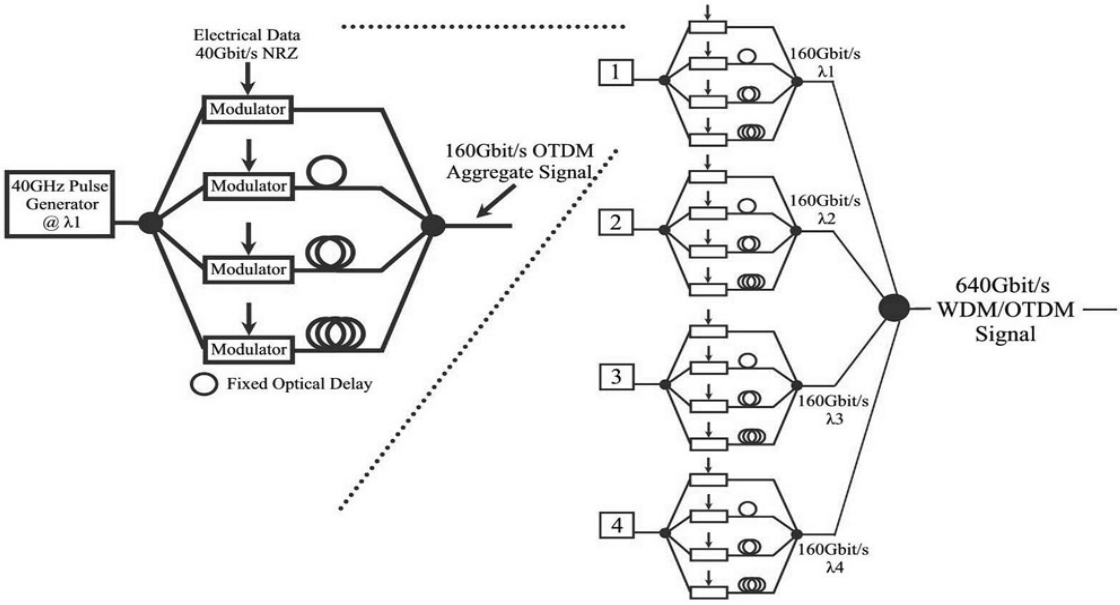

Figure 1-4 Schematic of the possible configuration of 640 Gb/s WDM/OTDM system

1.2.4. Hybrid OTDM/WDM

OTDM might be employed to increase individual line-rates of a WDM system, and in one such example a 10x320Gb/s transmission system over standard Single Mode Fiber (SMF) was demonstrated [16]. A schematic model for a 4 channel hybrid WDM/OTDM system is shown after [17] in Figure 1-4. This hybrid configuration has several advantages over pure WDM. The overall system capacity is a product of individual signal rates and number of wavelength channels. However, line-rate and wavelength density have their physical limits that can not be exceeded. This is due to the fact that wavelength-channel bandwidth increases with increased line-rate. Consequently higher line-rates require wider wavelength channel separation, and vice versa higher wavelength-channel density requires lower channel line-rate. This can be described using Fourier analysis where a temporal optical signal amplitude A(t) is decomposed into an infinite series of sinusoidal functions of different amplitudes A_m, frequencies ω_m, and phases φ_m:

$$A(t) = \sum_{m=-\infty}^{\infty} A_m \sin(\varpi_m t + \varphi_m) \tag{1-1}$$

The decomposed sinusoidal functions are commonly referred to as spectral components of the optical signal. Any optical signal can be then represented in the frequency domain as a plot of the spectral component's amplitudes versus its frequencies. Commonly the squared spectral amplitude is plotted which corresponds to the measurable optical spectral intensity. Spectral representation has its width parameter commonly measured as a Full Width at Half Maximum (FWHM). The Frequency representation width is commonly referred to as the signal bandwidth. The relation between signal temporal and frequency representations is given by a Fourier Transform. Directly from the Fourier analysis higher-bit rate corresponds to the wider signal bandwidth. Consequently there is a balance between a number of wavelength-channels and the channel's line-rate in WDM system. This means that for given system transmission band (e.g. C-Band) there is a maximum capacity that might be achieved either by small number of fast WDM channels or large number of relatively slow WDM channels. An example of the first approach might be a single line 1.28Tb/s transmission reported in [15]. The second approach is in some extent implemented in today's DWDM systems, where typically 40-80 wavelength channels with individual channel rates rarely exceeding 10 Gb/s are transmitted. At the time of writing (December, 2008) 40G technology is still in development stage with the first commercial implementation being just reported (August, 2008) by Huawei Technologies [18].

In principle both approaches are equivalent for high capacity transmission. Other factors such as transmitter jitter, transmission impairments, clock recovery facility, system complexity and others decide which approach is more efficient and simple to implement. Optical systems are evaluated

using a Bit-Rate-Bandwidth (BRB) factor defined as a ratio between system overall capacity and occupied transmission band. It is believed [19] that hybrid OTDM/WDM configuration will allow for higher BRB ratios at lower costs. It is because the high capacity hybrid transmission is easier to implement and control then pushing pure OTDM or WDM technologies to its limits. Additionally the high speed line accommodates naturally high bit rate payloads with easier supervision of the multiplexed line.

A meaningful advantage of OTDM/WDM is a reduction of the required number of optical sources, filters and detectors in the whole system. This reduces system complexity and simplifies its management. Such a hybrid OTDM/WDM configuration has a potential of offering highly compact optical systems with minimised footprint, reduced power consumption and maximised cost-per-bit efficiency. The following section will concern one of the key components in an OTDM system, namely the optical pulse sources.

1.3. Short-Pulse Generation

High-speed optical transmission requires short optical pulses either to carry the digital information, or for high speed optical signal processing techniques. Ultra-short pulse generation is critical for future communications systems. Common pulse generation techniques are gating of Continuous Waveform (CW) signal, passive/active mode locking, and gain-switching. Additional techniques may be used to compress pulses, these include the use of fiber Bragg gratings [20][21][22], Soliton-effect [23] and others. Various techniques result in different pulse temporal and spectral profiles. This section describes the most common short pulse generation techniques.

1.3.1. Mode Locking

Mode locking is achieved by modulating the loss or gain of a diode laser at a frequency that is equal to the intermodal spacing of the cavity modes. In this case each spectral mode is driven by the modulation sidebands of its neighbours [24]. As a result, phases of modes are locked by the external modulation. Commonly the cavity length is increased by placing the laser diode into an external resonator or by using an extend-up-to-several-millimetres monolithic cavity resulting in internal mode spacing within 0.3 to 20 GHz. The laser resonator contains either an active element: an optical modulator (active mode locking) or a nonlinear passive element: a saturable absorber (passive modelocking), which causes the formation of an ultra-short pulse circulating in the laser resonator [25]. Each time the pulse hits the output coupler mirror, a usable pulse is emitted, so that a regular pulse train leaves the laser. Assuming a single circulating pulse, the pulse repetition period corresponds to the resonator round-trip time, whereas the pulse duration is much lower, typically between 30fs and 30ps, in extreme cases down to 5fs.

In the absence of a frequency–selective element, a laser operates simultaneously in a large number of longitudinal modes supported by the cavity. The frequency spacing among the modes is given by:

$$\Delta\nu = c / L_{opt} \tag{1-2}$$

where c is the free space speed of light and L_{opt} is the optical length during one round trip inside the cavity. Multimode operation is due to a wide gain bandwidth compared with the longitudinal-mode spacing. Since thousands of modes may fit within the gain profile, modes located in the vicinity of the gain peak experience the same gain and reach threshold simultaneously. The total optical field can be written as [26],[31]:

$$E(t) = \sum_{m=-M}^{M} E_m \exp(i\phi_m - i\varpi_m t) \tag{1-3}$$

where E_m, Φ_m and ω_m are the amplitude, the phase and the frequency of m-th mode and 2M+1 represents the total number of modes. If all modes operate independently of each other with no definite phase relationship among them, the interference terms in the total intensity $|E(t)|^2$ vanish, making it time independent. This is the situation for multimode CW lasers. Mode-locking occurs when phases of various longitudinal modes are synchronized such that the phase difference between any two neighboring modes is locked to a constant value Φ such that Φ_m-Φ_{m-1}=Φ. This can be achieved by modulating the gain (or loss) section with frequency equal to the intermodal spacing of the cavity modes, resulting in the modes being locked by side bands of the neighboring modes. Alternatively saturable absorber with recovery time corresponding to the cavity frequency can be used to obtain passive mode locking. If the phase difference between the neighboring modes is fixed the sum in (7) can be carried out analytically. Here for simplicity if we assume equal mode amplitudes E_0 the output optical power temporal variations can be written as:

$$\left|E(t)\right|^2 = \frac{\sin^2\left[2(M+1)\pi\Delta\nu t + \phi/2\right]}{\sin^2(\pi\Delta\nu t + \phi/2)} E_0^2 \tag{1-4}$$

Figure1-5 plots the equation (1.4) for example values of: M=4, Δν=10GHz, Φ=0, E_0=1.

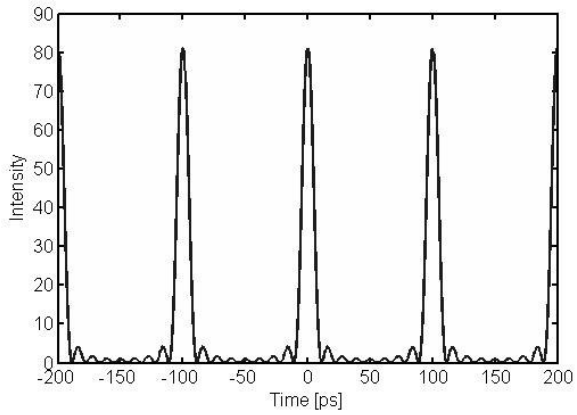

Figure 1-5 Calculated mode-locked pulse train

This simplified model shows the principle of mode-locking pulse generation. In more accurate description the active region gain profile resulting in unequal mode amplitudes need to be considered. In addition an external Fabry-Perot cavity results in optical spectrum of a diode laser (determined by the gain profile) being affected by the external resonator. A typical optical spectrum of a diode laser in an external resonator is shown (after [27]) in Figure 1-6 where l is the diode laser cavity length and L is the external cavity length.

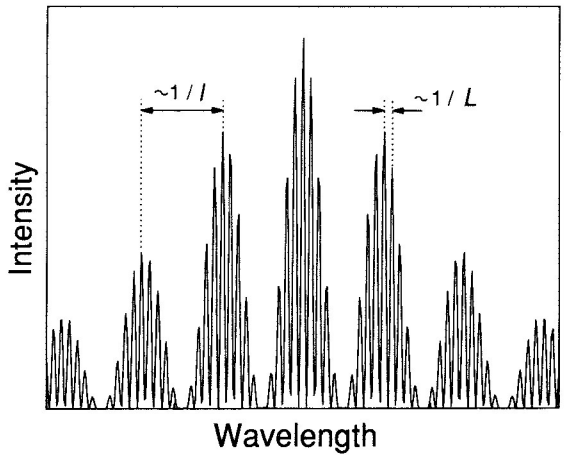

Figure 1-6 A typical optical spectrum of a diode laser in an external resonator, l is the length of the laser diode, L is the external cavity langth

The resonant current modulation of the laser diode results in the locking of external cavity modes within each cluster however phases between clusters are distributed randomly. In practical realization an external selective element, Fabry-Perot etalon (FP) or diffraction grating (DG) can be used to reduce output optical spectrum and the composite Fabry-Perot resonator effect as shown in Figure 1-7 a) and b) respectively.

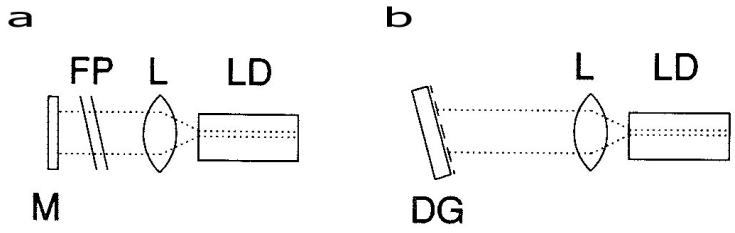

Figure 1-7 External cavity configurations of mode locked diode lasers with wavelength selective element a) Fabry-Perot etalon (FP), b) diffraction grating (DG)

A number of analytical and numerical models for mode locked laser description were developed e.g. by A.E. Siegman [28], D.J Kuizenga [29] and H.A. Haus [30].

The pulse shape achieved is governed by a balance of pulse shortening through the modulator and pulse broadening due to the limited gain bandwidth, wavelength filtering and other effects Commonly optical pulses generated using mode-locking technique are best described using $sech^2$ power envelope. Passive mode locking (with a saturable absorber) allows for the generation of much shorter (femtosecond) pulses, basically because a saturable absorber, driven by already short pulses, can modulate the resonator losses much faster than an electronic modulator: the shorter the pulse becomes, the faster the loss modulation, provided that the absorber has a sufficiently short recovery time. The pulse duration can be even well below the recovery time of the absorber.

1.3.2. Gain-Switching

Gain switching is a method for pulse generation that involves fast modulation of the laser gain via the electric drive current. A direct modulation can be applied for the gain switching of semiconductor laser diodes by directly driving the laser with large amplitude, fast electrical pulses. The first indication that very short pulses could be generated by the gain switching technique came about with the observations of relaxation oscillations when turning on a laser diode from below threshold using electrical pulses with a fast leading edge [31]. The idea is to excite the first spike of the relaxation oscillation and terminate the electrical pulse before the onset of the second spike. Initially the laser is biased with DC current, which is below the lasing threshold. A large amplitude pulsed current is then applied to the laser resulting in rapid carrier concentration increases. When the carrier concentration exceeds the threshold value (population inversion) the lasing starts. The photon density however increases at a slower rate, and as it reaches its maximum level, it rapidly depletes the carrier concentration. This is followed by photon density decreasing, and if the current pulse is cut-off at this time a short optical pulse is generated.

Modulated optical pulses can be propagated through an optical fiber to transmit information. A short pulse transmission and optical fiber impairments will be discussed in the following section.

1.4. High-Speed Propagation in Optical Fiber

In its simplest form, an optical fiber consists of a cylindrical core of silica glass surrounded by a cladding whose refractive index is lower than that of the core. A fiber with an abrupt index change at the core-cladding interface is called a step-index fiber to distinguish it from graded-index fiber in which the refractive index of the core decreases gradually from center to the core boundary. Step index fiber suffers from an impairment called multi-path or inter-modal dispersion. This can be significantly reduced using graded-index fiber or removed entirely when operating in a single mode condition. The number of modes propagating in a fiber can be varied depending on the fiber design, particularly on index difference, between core and cladding, and fiber core diameter. Fibers that propagate only one fundamental mode are called Single Mode Fibers (SMF). Modal description of light propagation in optical fiber can be considered utilizing Maxwell's equations for electromagnetic waves [31]. This results in the commonly used Nonlinear Schrödinger Equation for signal propagation in optical fiber:

$$i\frac{\partial A}{\partial z} = \frac{1}{2}\beta_2 \frac{\partial^2 A}{\partial t^2} - \gamma |A|^2 A \tag{1-5}$$

where A is the slowly varying amplitude of the pulse envelope, t is the time measured in a reference frame moving with the pulse at the group velocity v_g, and z is distance along the fiber. The equation (1-5) describes optical pulse propagation within Single Mode Fiber (SMF) assuming maintained polarization along the fiber length, quasi-monochromatic operation and neglecting fiber losses. It is suitable for the description of pulse propagation as short as 1ps. Shorter pulses require including higher order dispersion effects and delayed nonlinear response [32]. The two terms on the right-hand side of the equation (1-5), containing β_2 and γ, govern respectively the effects of Group Velocity Dispersion (GVD) and Self Phase Modulation (SPM) of pulses propagating inside the fiber. Both effects results in pulse temporal (GVD) and spectral (SPM) broadening, limiting performance of an optical communication system. In addition optical systems suffer from impairments such as Polarisation Mode Dispersion (PMD), inelastic scattering, Optical Signal to Noise Ratio (OSNR) degradation and others. These impairments became more considerable with increased data-rate and can fluctuate in time with varied environmental conditions. High-capacity systems operating at ultra-high bit-rates will require careful design with continuous performance monitoring and adaptive impairments compensation. This section will review the most important fiber propagation impairments.

1.4.1. Group Velocity Dispersion

Group Velocity Dispersion (GVD) also referred to as Chromatic Dispersion (CD), manifests itself through the frequency dependence of the refractive index n(ω) of the optical fiber. This results in different propagation velocities of different frequency components and as a consequence temporal pulse broadening. Mathematically, the effect of GVD is accounted by expanding the mode-propagation constant β in series about the mode central frequency ω_0:

$$\beta(\omega) = n(\omega)\frac{\omega}{c} = \beta(\omega_0) + (\omega - \omega_0)\left|\frac{\partial\beta}{\partial\omega}\right|_{\omega_0} + \frac{1}{2}(\omega - \omega_0)^2\left|\frac{\partial^2\beta}{\partial\omega^2}\right|_{\omega_0} + \ldots \quad (1\text{-}6)$$

The first derivation of β defines the pulse envelope group velocity:

$$v_g = \left(\left|\frac{\partial\beta}{\partial\omega}\right|_{\omega_0}\right)^{-1} \quad (1\text{-}7)$$

The second and following derivations of β, are called consecutive GVD parameters and are responsible for temporal pulse broadening. The cubic and higher-order terms in this expansion are generally negligible for quasi-monochromatic operation, and only second-order derivation usually referred to as β_2 is considered. Higher-order terms however needs to be considered when propagating around fiber zero-dispersion (β_2=0) wavelength or when ultra-short (<1ps) pulses are considered. Fiber dispersion is commonly described as dispersion parameter D defined when neglected higher order GVD parameters by:

$$D = -\frac{2\pi c}{\lambda^2}\beta_2 \quad (1\text{-}8)$$

usually presented in ps/km/nm. Standard SMF has zero-dispersion wavelength around 1310nm, and around 17 ps/km/nm dispersion at 1550nm. Special type Dispersion Shifted Fiber (DSF) was fabricated to have zero dispersion around 1550nm and Dispersion Flattened Fiber (DFF) that has flat dispersion characteristic around 1550nm wavelength window. Initially DFF was fabricated for WDM transmission however its applicability is limited due to channel cross-talk effect. The number of wavelength channels propagating along the fiber with the same group velocities results in improved phase matching between propagating wavelengths and leads to a significant increase in Four Wave Mixing (FWM) between the channels. This causes channel cross-talk over long distances. Consequently for WDM applications a special kind of DSF is used with a small amount of dispersion around 1550nm, called Non-Zero Dispersion Shifted Fiber NZ-DSF. The small amount of dispersion reduces FWM cross-talk between channels and can be then compensated using dispersion management scheme. This involves including in the transmission path a fixed-value, negative-dispersion elements that compensate for the positive dispersion encountered by the signal. A vast number of deployed systems use Dispersion Compensating Fibers (DCF) although

chirped Fiber Bragg Gratings (FBG) can also be used [33]. This technique however does not compensate for additional CD fluctuations that arise due to β_2 temperature variations [34][35] or mechanical stress. Such variations will become a serious problem when individual channel data rates start to exceed 10Gb/s. This will be discussed in greater detail in Chapter 4.

1.4.2. Nonlinear Effects

The response of an optical material to light becomes nonlinear for intense electro-magnetic fields. On a fundamental level, the origin of the nonlinear response is related to anharmonic motion of bound electrons under the influence of an applied field. The lowest-order nonlinear effects in optical fibers originate from the third-order susceptibility, responsible for four-wave mixing (FWM), nonlinear refraction and stimulated inelastic scattering.

FWM results in wavelength-channel interference in WDM systems and become a serious problem when high optical power is transmitted over a long distance. The nonlinear refraction – intensity dependence of the refractive index – leads to Self-Phase Modulation (SPM) and Cross-Phase Modulation (XPM) effects. SPM is responsible for spectral broadening of ultra-short pulses [36] and XPM results in nonlinear phase shift of an optical field induced by another field having a different wavelength. XPM in WDM systems can result in a fluctuation of accumulated dispersion experienced by different wavelength-channels, reducing effectiveness of dispersion management techniques. A second class of nonlinear effects results from stimulated inelastic scattering in which the optical field transfers part of its energy to the nonlinear medium. These include Stimulated Raman Scattering (SRS) and Stimulated Brillouin Scattering (SBS). In both effects photons of the incident field are annihilated to create a photon of different frequency and a phonon with the right momentum and energy to fulfill the conservation of energy.

Nonlinear effects need to be carefully considered when designing high-capacity systems since they can significantly reduce its performance. On the other side, they have a potential to be used for ultra-fast all-optical signal processing in high-speed communication systems. FWM can be utilized for optical wavelength-channel conversion [37], SPM for optical soliton propagation in the anomalous-dispersion regime of fibers [38], and XPM for ultra-fast OTDM channel switching. Applications of nonlinear effects for all-optical signal processing will be discussed in detail in Chapter 2.

1.4.3. Fiber Attenuation

Attenuation is a fundamental limiting factor of any fiber communication system. The maximum transmission distance is a function of transmitted power, fiber attenuation and receiver sensitivity.

Receiver sensitivity is defined as the minimum input signal power, required to produce output signal, having a specified Signal-to-Noise Ratio (SNR). SNR is the signal power in the receiver divided by the mean noise power of the receiver.

Early optical transmission required inline signal regenerators, converting optical signal into electrical domain, amplifying it and retransmitting back as optical signal. With the introduction of Erbium Doped Fiber Amplifiers (EDFA) and later Raman and Semiconductor Optical Amplifiers (SOA), transmission distances without optical to electrical conversion, were significantly increased. The important parameters of optical amplifiers are gain and bandwidth allowing for multi-wavelength transmission in WDM system. A limiting factor is a spontaneous emission in the amplifier that successively degrades transmitted Optical Signal to Noise Ratio (OSNR) of the signal. OSNR is defined as a ratio between optical signal power and the mean optical noise power. The optical noise originates from the optical transmitter during signal generation process, and EDFA Amplified Spontaneous Emission (ASE) noise that is added to the signal during amplification. The transmitted signal needs to be regenerated before OSNR degrades to the level preventing correct signal detection. This might be achieved traditionally involving optical to electrical conversion, electrical regeneration and retransmission, or using novel all-optical regeneration techniques. Another problem associated with EDFA's is unequal gain along the amplification bandwidth that results in varied power between WDM channels. High power channels can saturate in-line EDFAs and prevent low power channel amplification. Consequently additional power leveling methods are required to ensure proper system performance.

1.4.4. Polarization Mode Dispersion

Polarisation Mode Dispersion (PMD) is a phenomenon of temporal pulse broadening due to stochastic fiber birefringence fluctuation along the fiber. The optical birefringence (or double refraction) is a property of an anisotropic material. In general three anisotropy axes can be distinguished. In optical fiber, however, one axis lies along the fiber length and does not influence light propagation. Birefringence can be introduced in optical fiber by applying transverse tension along the fiber. This result in different refractive indexes for light polarised perpendicularly and in parallel to the applied strain. Consequently fast (ordinary) and slow (extraordinary) birefringence axes are distinguished. Any polarisation state of light coupled into birefringent fiber can be decomposed into two basic linear polarization-modes along the ordinary and extraordinary axes. Both modes propagate along the fiber with different group-velocities resulting in summary polarization periodical change (beating). If an optical pulse is coupled into highly-birefringent fiber the difference in propagation group-velocities results in pulse broadening and consequently pulse separation into two perpendicularly polarized pulses. This phenomenon is known as Polarisation

Mode Dispersion (PMD) and its magnitude is measured with the Differential Group Delay (DGD) parameter. Ideally telecommunication fiber should not exhibit any birefringence. In fact, due to small fiber rotational asymmetry, fiber bending or other kinds of mechanical stress, random birefringence occurs along the fiber. Fiber birefringence is also affected by environmental conditions such as temperature or pressure fluctuations. Birefringent axes and DGD value change randomly along the fiber causing the propagated pulse broadening to be proportional (due to statistical character) to the square root of the propagation distance. A DGD parameter for telecommunication fiber is a measure of the strength and frequency of the fiber imperfections.

Polarization mode dispersion can have adverse effects on optical data transmission in fiber-optic links over long distances at very high data rates. PMD pulse broadening causes temporal bit interference and degrades link performance. Modern telecom fibers have fairly stringent PMD specifications, but fibers laid in the early 1990s often exhibit much stronger PMD, which is often not even specified. Due to statistical, time-dependant character, compensation of PMD is difficult and it is often necessary to apply an automatic feedback system with a tuneable-birefringence element. If the system has multiple wavelength channels, the compensation has to be done separately for each channel, because the effect is wavelength dependent.

1.5. Optical Modulation Formats

A digitalized optical bit-stream can be transmitted in fiber utilizing two basic codes known as Return to Zero (RZ) and Non-Return to Zero (NRZ). Commonly an electrical bit stream is used to modulate the intensity of the optical carrier and the optical signal is detected directly at a photodiode to convert it to the original digital signal in the electrical domain. Such schemes are referred to as intensity modulation with direct detection. In the RZ code, each optical pulse representing bit 1 is shorter than the bit slot, and its amplitude returns to zero before the bit duration is over. In the NRZ code, the optical pulse remains on throughout the bit slot and its amplitude does not drop to zero between two or more successive 1 bits. The advantage of NRZ format is that the transmitted signal is spectrally narrower or in other worlds the bandwidth associated with the bit stream is narrower. Narrower-bandwidth signals offer higher spectral efficiency (occupied bandwidth per wavelength channel) and suffer less from Chromatic Dispersion (CD) impairments. However, its use requires tighter control of the pulse width and may lead to bit-pattern-dependent effects.

As an alternative for intensity modulation with direct detection the coherent lightwave systems were proposed. A basic concept is to mix the received signal coherently with another optical wave before

it is incident on the photo-detector. The optical wave is generated locally at the receiver by using a narrow-linewidth laser, called a Local Oscillator (LO). Consequently the photocurrent measured is given by:

$$I(t) = R(P_S + P_{LO}) + 2R\sqrt{P_S P_{LO}}\cos(\omega_{IF} t + \phi_S - \phi_{LO}) \quad (1\text{-}9)$$

where R is the receiver responsivity, P_S, P_{LO} are signal and LO optical powers, intermediate frequency $\omega_{IF}=\omega_S-\omega_{LO}$ is the difference between incident signal frequency ω_S and LO frequency ω_{LO}, Φ_S, Φ_{LO} are signal and LO phases. Depending on whether or not ω_{IF} equals zero, coherent systems divide into homodyne and heterodyne systems. Both techniques improve detection sensitivity. Additionally information can be transmitted through amplitude, phase, or frequency modulation of the optical carrier. Amplitude modulation is referred to as on-off keying (OOK) and is identical with the intensity modulation scheme in noncoherent digital lightwave systems. The frequency modulation called Frequency Shift Keying (FSK) makes use of direct-modulation capability of semiconductor lasers where small changes in the operating current results in feasible frequency changes. The most commonly employed coherent technique is Phase Shift Keying (PSK) where transmitted data is encoded using phase variation between transmitted bits.

The main difficulty associated with coherent detection is the requirement for phase stability between signal and LO. This problem is minimised in Differential Phase Shift Keying (DPSK) scheme where data is encoded using the phase difference between consecutive bits. Successive decoding is feasible as long as the carrier phase remains stable over duration of two bits. Direct detection can be employed with the implementation of a one-bit-delay interferometer (balanced receiver), resulting in cost-effective enhanced receiver sensitivity [39],[40]. DPSK transmission of 160 Gb/s signal over 1000 km [41], and 2.56 Tb/s signal over 160 km [42] have been demonstrated. The RZ-DPSK format offers a 3 dB improvement in OSNR sensitivity in comparison to OOK, which in turn offers 1-2 dB improvement in sensitivity compared to the simple NRZ format. An attractive DPSK feature is long term stable receiver operation because it has a constant decision threshold regardless of the signal power [43].

To maximize spectral efficiency, modulation formats with narrow spectra are desired, such as nonreturn-to-zero (NRZ). However, such modulation formats tend to have higher nonlinear impairments and greater intersymbol interference, resulting in shorter system reach. In other words NRZ channel will experience more signal distortion than a RZ channel, even assuming that the receiver is separately optimized for each modulation format [44][45]. Consequently RZ modulation formats are most likely to be used in future ultra-high-speed communication systems. Some advanced modulation formats carrying the information through OOK, but also modulating the

optical phase in a non-information-bearing way, have attracted increased attention [46][47]. These include duobinary, Alternate Mark Inversion (AMI), Chirped Return-to-Zero (CRZ) and Alternating-Phase (AP) OOK formats such as Carrier-Suppressed Return-to-Zero (CSRZ). The optical phase modulation enhances signal's robustness to chromatic dispersion, optical filtering, and nonlinearities. Also multi-level modulation formats are highly desirable as the resulting transmission bandwidth is reduced proportionally to $\log_2(N)$, where N represents the number of levels. This resulted in modulation formats such as Differential Quadrature Phase-Shift Keying (DQPSK) [48].

1.6. Summary

Due to continued increase in commercial demand for higher bandwidth, novel high-speed data transmission systems are investigated. Successive generations of transmission networks increased line-rates resulting in 2.5 Gb/s, 10 Gb/s and currently introduced 40Gb/s technologies. Channel bit rates in excess of 100 Gb/s are currently being explored and maybe implemented commercially in coming years. The main advantages of high-speed operation compare to multi-wavelength low bit-rate systems are smaller foot-print, higher cost-per-bit efficiency and easier system management. Novel ultra-fast signal processing techniques are required to overcome electronic processing limits and compensate for higher optical fiber transmission impairments. Optical nonlinearities that occur on time scales in the order of few femtoseconds, are potential candidates for the future high-speed processing schemes. The principles of optical nonlinearity and possible applications will be discussed in the following Chapter.

References

[1] G. Bell, U.S. Patent No. 174,465 (1876)

[2] J.Hegarty, S.D.Poulsen, K.A.Jackson, I.P.Kaminow, "Low-loss single-mode wavelength-division multiplexing with etched fibre arrays," *IEEE Electronics Letters*, vol.20, no.17, pp. 685-686, 1984

[3] N.A.Olsson, R.Logan, L.F.Johnson, „Transmission experiment at 3 Gbit/s with close-spaced wavelength-division-multiplexed single-frequency lasers at 1.5μm," *IEEE Electronics Letters*, vol.20, no.17, pp.673-674, 1984

[4] "Samsung introduces low water-peak fiber," *Fiber Optics Weekly Update*, 21 May, 2004, http://findarticles.com/p/articles/mi_m0NVN/is_21_24/ai_n6063670

[5] O.E.DeLange, "Some Optical Communications Experiments," *Journal of Applied Optics*, vol.9, no.5 pp.1167-1175,1970

[6] R. J. Mears, L. Reekie, M. Jauncey, and D. N. Payne, "Low-noise erbium-doped fiber amplifier operating at 1.54 μm", *IEEE Electronics Letters,* vol. 26, pp.1026, 1987

[7] E. Desurvire, J. R. Simpson, and P. C. Becker, "High-gain erbium doped traveling wave fiber amplifier", *Optics Letters*, vol. 12, no.11, pp. 888, 1987

[8] M.K. Smit, "Progress in AWG design and technology," *IEEE/LEOS workshop on fibres and optical passive components*, pp. 26-31, Jun. 2005.

[9] B. Mikkelsen, C. Rasmussen, P. Mamyshev, F. Liu, S. Dey F. Rosca, "Deployment of 40 Gb/s systems: technical and cost issues," *in conference on Optical Fibre Communication (OFC'04)*, vol. 2, no. ThE6, p. 3, 2004

[10] R.Ludwig, "Ultrafast Transmission Technology," *in European Conference on Optical Communications (ECOC'2005)*, vol.5, pp. 159-168, 2005

[11] R.S. Tucker S. K. Korotky, G. Eisenstein, L. L. Buhl, J. J. Veselka, G. Raybon, Bryon L. Kasper, A. H. Gnauck, and Rodney C. Alferness., *in Conference on Optiical Fiber Communication* (OFC'88), Paper ThB2 (1988).

[12] V. Marembert et. al., „Single channel 640Gbit/sDPSK transmission over a 160km fibrelink," *in European Conference on Optical Communications* (ECOC'04), Stockholm, Postdeadline paper Th4.4.6

[13] S. Bhandare et al., "5.94 Tbit/s 1.49 b/s/Hz (40 x 2 x 2 x 40 Gb/s) RZDQPSK polarization-division multiplex C-band transmission over 324 km", *IEEE Photonics Technology Letters*, vol. 17, no. 4, April 2005

[14] Jeff Hecht, "OTDM promises higher communications speeds using optical processors," *Laser Focus World*, vol.39, no.11, Nov. 2003

[15] M. Nakazawa, T. Yamamoto and K.R. Tamura, "1.28TbWs-70 km OTDM transmission using third- and fourth-order simultaneous dispersion compensation with a phase modulator," *IEEE Electronics Letters*, vol.36, no.24, pp.2027-2029, 2000

[16] A. Suzuki, X. Wang, Y. Ogawa and S. Nakamura, “10 x 320 Gbit/s DWDM/OTDM transmission in C-band by semiconductor-based devices”, *in European Conference on Optical Communications (ECOC’04)*, Postdeadline paper Th4.1.7

[17] P.J.Maguire, L.P.Barry, T.Krug, M.Lynch, A.L.Bradley, J.F.Donegan, H.Folliot, "All-Optical Sampling based on Two-Photon Absorption in a Semiconductor Microcavity for High-Speed OTDM," Proc. SPIE, Vol. 5825, p.316 (2005)

[18] Huawei Technologies Co Ltd., “Huawei to build China's first 40G transmission network for China Telecom,” html document, 2008 *http://www.huawei.com/news/view.do?id=5540&cid=42*

[19] Richard Penty, “Optical TDM makes faster networks possible,” *Laser Focus World*, vol.36, no.1, Jan. 2000

[20] D. Grischkowsky, A. C . Balant, “Optical pulse compression based on enhanced frequency chirping,” *Applied Physics Letters*, vol.41, pp. 1-3, July 1982.

[21] W.J. Tomlinson, R.H. Stolen, C.V. Shank, “Compression of optical pulses chirped by self-phase modulation in fibers,” *Journal of the Optical Society of America, B1*, pp. 139-149, Apr. 1984.

[22] B. Nikolaus, D. Grischkowsky, “90 fs tunable optical pulses obtained by two-stage pulse compression,” *Applied Physics Letters*, vol.43, pp. 228-230, Aug. 1983.

[23] A.S. Gouvera-Neto, A.S. L. Gomes, J.R. Taylor, “Generation of 33-fsec pulses at 1.32 μm through a high-order soliton effect in a single-mode optical fiber,” *Optics Letters,* vol. 12, no.6, 395, (1987)

[24] K. Y. Lau, “Short Pulse and High-Frequency Signal Generation in Semiconductor Lasers,” IEEE J. of Lightwave Technology, vol.7, pp.400-419, 1989

[25] W. E. Lamb Jr., “Theory of an optical laser”, *Physical Review* 134 (6A), A1429 (1964)

[26] Govind P. Agrawal, ”Nonlinear Fiber Optics,” Academic Press, San Diego, 1995

[27] Peter Vasil’ev, “Ultrafast diode lasers, fundamental and applications”, Artech House, Boston, London

[28] A.E. Siegman, D.J Kuizenga, “Simple Analityc Expressions for AM and FM Mode-Locked Pulses in Homogeneous Lasers,” Applied Physics Letters, vol.14, pp. 181-183

[29] D.J Kuizenga, A.E. Siegman, “FM and AM Mode Locking of the Homogeneous Laser,” IEEE J. of Quantum Electronics, vol.6, pp.694-708, 1970

[30] Haus, H.A., “A Theory of Forced Mode Locking,” IEEE J. of Quantum Electronics, vol. 11, pp. 323-330, 1975

[31] P. Vasil’ev, “Ultrafast Diode Lasers: Fundamental and Applications (1st Ed.),” Artech house, 1995

[32] Y. Kodama, A. Hasegawa, “Nonlinear pulse propagation in a monomode dielectric guide**,”** *IEEE Journal of Quantum Electron*ics vol.23, no.5 pp.510 (1987).

[33] M.J.Cole, K.Geiger, R.I.Laming, S.Y.Set, M.N.Zervas, W.H.Loh, V.Gusmeroli "Broadband dispersion-compensating chirped fibre Bragg gratings in a 10 Gbit/s NRZ 110 km non-dispersion-shifted fibre link operating at 1.55 μm," *IEEE Electronics Letters*, vol.33, no.1, pp.70-71, 1997

[34] W.H.Hatton and M. Nishimura, "Temperature dependence of chromatic dispersion in single mode fibers," *IEEE Journal of Lightwave Technology*, vol.4, no.10, pp.1552-1555, 1986.

[35] T.Kato, Y.Koyano and M.Nishimura, "Temperature Dependence of Chromatic Dispersion in Various Types of Optical Fibers," *in conference on Optical Fiber Communication (OFC'00)*, vol.1, pp 104-106, paper TuG7, 2000

[36] R. H. Stolen and C. Lin, "Self-phase-modulation in silica optical fibers," *Physical Review A*, vol.17, pp. 1448 (1978).

[37] S. Diez, C. Schmidt, R. Ludwig, H. G. Weber, K. Obermann,S. Kindt, I. Koltchanov, K. Petermann, "Four-Wave Mixing in Semiconductor Optical Amplifiers for Frequency Conversion and Fast Optical Switching*," IEEE Journal of Selected Topics in Quantum Electronics*, vol.3, no.5, 1997

[38] A. Hasegawa and F. Tappert, "Transmission of stationary nonlinear optical pulses in dispersive dielectric fibers. I. Anomalous dispersion," *Applied Physics Letters*, vol.23, no.3, pp. 142 (1973)

[39] P. A. Humblet and M. Azizoglu, "On the bit error rate of lightwave systems with optical amplifiers," *Journal of Lightwave Technology*, vol. 9, no. 11, pp. 1576–1582, 1991.

[40] S. R. Chinn, D. M. Boroson, and J. C. Livas, "Sensitivity of optically preamplified DPSK receivers with Fabry-Perot filters," *Journal of Lightwave Technology*, vol. 14, no. 3, pp. 370–376, Mar. 1996.

[41] Toshihiko Hirooka, Masatada Okazaki, Masataka Nakazawa, "A Straight-Line 160-Gb/s DPSK Transmission Over 1000 km With Time-Domain Optical Fourier Transformation," *IEEE Photonics Technology Letters*, vol.20, no.13, 2008

[42] H.G. Weber, S. Ferber, M. Kroh, C. Schmidt-Langhorst, R. Ludwig, V. Marembert, C. Boerner, F. Futami, S. Watanabe, C. Schubert, "Single channel 1.28 Tbit/s and 2.56 Tbit/s DQPSK transmission," IEEE Electronics Letters, vol. 42, no. 3, pp. 178-179, 2006

[43] S. Ferber, R. Ludwig, C. Boerner, A.Wietfeld, B. Schmauss, J. Berger, C. Schubert, G. Unterboersch, and H. G.Weber, "Comparison of DPSK and OOK modulation format in 160 Gbit/s transmission system," *IEEE Electronics Letters*, vol. 39, pp. 1458–1459, 2003.

[44] A.H. Gnauck, G. Raybon, S. Chandrasekhar, J. Leuthold, C. Doerr, L. Stulz, A. Agarwal, S. Banerjee, D. Grosz, S. Hunsche, A. Kung, A. Marhelyuk, D. Maywar, M. Movassaghi, X. Liu, C. Xu, X. Wei, D.M. Gill, "2.5 Tb/s (64/spl times/42.7 Gb/s) transmission over 40/spl times/100 km NZDSF using RZ-DPSK format and all-Raman-amplified spans", *in Conference on Optical Fiber Communication* (OFC'02), pp. FC2-1 - FC2-3

[45] A. Belahlou, S. Bickham, D. Chowdhury, P. Diep, A. Evans, J.M. Grochocinski, P. Han, A. Kobyakov, S. Kumar, G. Luther, J. C. Mauro, Y. Mauro, M. Mlejnek, M. S. K. Muktoyuk, M. T. Murtagh, S. Raghavan, V. Ricci, A. Sevian, N. Taylor, S. Tsuda, M.

Vasilyev, L. Wang, “Fiber Design Considerations for 40 Gb/s Systems,” *IEEE Journal of Lightwave Technology*, vol. 20, no. 12, pp. 2290–2305, 2002

[46] P. J. Winzer and R.-J. Essiambre, “Advanced optical modulation formats,” *in European Conference on Optical Communications* (ECOC’03), Invited paper Th2.6.1, pp. 1002–1003, 2003

[47] A. H. Gnauck, X. Liu, X.Wei, D. M. Gill, and E. C. Burrows, “Comparison of modulation formats for 42.7-Gb/s single-channel transmission through 1980 km of SSMF,” *IEEE Photonics Technology Letters*, vol. 16, pp. 909–911, 2004.

[48] S. Bhandare; D. Sandel; B. Milivojevic; A. Hidayat; A.A. Fauzi; Hongbin Zhang; S.K. Ibrahim; F. Wust; R. Noe, “5.94 Tbit/s 1.49 b/s/Hz (40 x 2 x 2 x 40 Gb/s) RZDQPSK polarization-division multiplex C-band transmission over 324 km”, *IEEE Photonics Technology Letters*, vol. 17, no. 4, April 2005

CHAPTER 2. High-Speed Nonlinear Signal Processing

2.1. Introduction

In the previous chapter the advantages of high-data-rate transmission for future communications systems were discussed. The transmission line-rates in excess of 100 Gb/s are expected to be implemented in the nearest future. Since some of the networking functions are difficult or impossible to carry out electrically, novel processing schemes are required. All-optical processing techniques remove the need for optical-to-electrical conversion, and electronic processing, resulting in optically transparent networks. Optical nonlinearities are potential candidates for a number of optical networking processing elements.

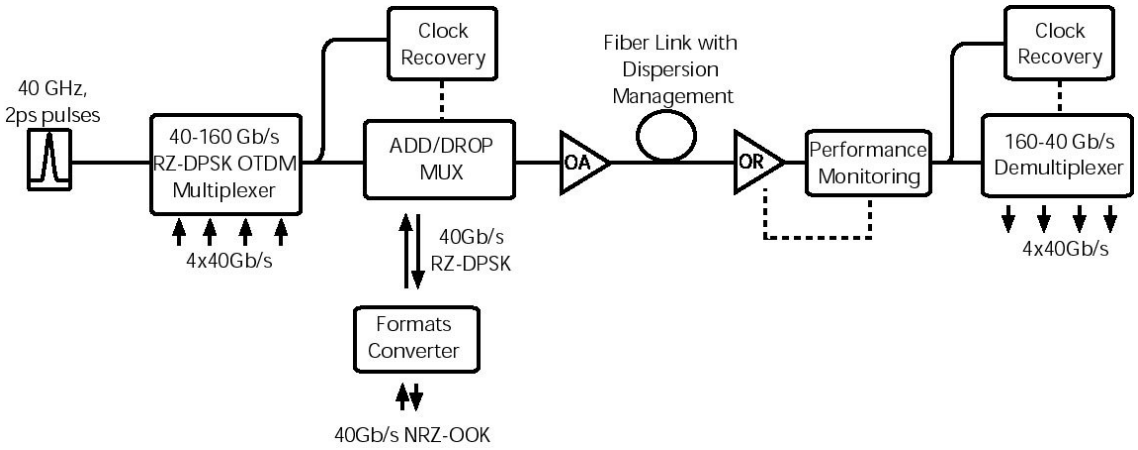

Figure 2-1 Schematic of 160 Gb/s RZ-DPSK transmission line

An example of high speed transmission line can be viewed in Figure 2-1. The coding format of choice is RZ-DPSK due to a better transmission performance then the conventional OOK for the long-haul transmission [1][2], however more advanced coding schemes such as multi-level PSK or CSPSK are also considered. The 160 Gb/s transmission can be realized involving OTDM multiplexing scheme with 40 GHz, 2ps pulse source and $LiNb0_3$ phase modulator [3] for DPSK data format. If the optical transmission link is going to span a number of metropolitan networks, different kinds of popular modulation formats should be transparently connected. Thus ADD/DROP multiplexer is required with format converter. All-optical format conversions, such as RZ-OOK to NRZ-OOK [4], Frequency Shift-Keying (FSK)-to-PSK [5] and NRZ-OOK to RZ-PSK [6] are studied. The data signal is transmitted through an optical fiber interlaced with in-line Optical-Amplifiers (OA) to compensate for fiber and connector losses. The OA realizes the most basic regeneration: re-amplification function, of the transmitted signal involving EDFA, Raman or SOA amplifiers, depending on the transmission bandwidth. However OA's inherently reduce the signal

OSNR and introduces unequal power levels in different WDM channels due to unequal gain profile. Thus OSNR regeneration and channel equalisation schemes are required.

The transmitted signal suffers a temporal broadening due to Chromatic Dispersion (CD) in an optical fiber link. Dispersion management is usually employed to compensate for a fixed amount of CD however additional fluctuations may appear due to environmental change. In addition PMD, SPM, non-elastic scattering (Raman, Brillouin) and channel cross-talk due to FWM and XPM in a multi wavelength operation reduces the overall transmission performance. The system tolerance for the above impairments decreases rapidly with increased transmission-rates. Consequently full Re-amplification, Re-shape and Re-time (3R) Optical Regenerators (OR) are required with gain equalizing filters for long-distance transmission. Optical regeneration describes an extremely wide range of techniques intended to be implemented to improve the systems performance. One possible approach utilizes a continuous signal performance monitoring module with a feedback to an adaptive compensation element. Nonlinear detection may be utilized for the all-optical signal performance monitoring, providing comprehensive signal quality information. Other important signal processing components that can be realized with optical nonlinearities include timing extraction (clock recovery) and high-speed optical switching required for ADD/DROP operation and signal demultiplexing. In this Chapter the principles of the optical nonlinearities and selected all-optical nonlinear signal processing techniques will be discussed. The nonlinear signal performance monitoring for the adaptive impairments compensation will be discussed in a great detail.

2.2. Optical Nonlinearities

When an electromagnetic optical wave interacts with any material it induces oscillations of bound electrons of the material lattice. This results in the creation of electric dipoles or in other words material polarisation. Since light frequencies differ significantly from the material resonance frequency the material polarisation P can be decomposed into a series given by:

$$P = \varepsilon_0 \left(\chi^{(1)} : E + \chi^{(2)} : EE + \chi^{(3)} : EEE + ... \right) \tag{2-1}$$

where ε_0 is the vacuum permittivity and tensors χ are successive orders of material susceptibilities, describing the material linear and nonlinear properties. The real and imaginary parts of the first-order susceptibility $\chi^{(1)}$ define material linear propagation (refractive) index and absorption (attenuation). Higher order susceptibilities describe an anharmonic motion of bound electrons oscillations and are responsible for the generation of new frequency components, nonlinear refraction and multi-photon absorption effects.

Second-order susceptibility is responsible for a group of nonlinear effects occurring only in materials that lack inversion symmetry at the molecular level. Example materials are optical crystals: $LiNb0_3$, KTP, KDP, $LiIO_3$, $AgGaS_2$, LiB_3O_5 and compound semiconductors such as GaAs and InP. $\chi^{(2)}$ nonlinearities are commonly used for electro-optic modulators and nonlinear frequency conversion. Electro-optic modulation utilizes a Pockels effect (nonlinear refraction) for the control of the transmitted signal power, phase or polarization through the modulator. Second-order frequency conversion also called Sum-Frequency Generation (SFG) is a process where two pump beams generate another beam with the sum or difference of the optical frequencies of the pump beams. A special case of SFG is a Second-Harmonic Generation (SHG) where a single pump wave interacts with a nonlinear medium resulting in the creation of its doubled frequency component. SHG in crystalline quartz was the first experimentally observed optical nonlinearity [7]. In telecommunications the SHG found its application for ultra-short pulses characterization in a number of configurations such as intensity or fringe resolved autocorrelation [8][9], cross-correlation [10] or Frequency Resolved Optical Gating (FROG) [11] techniques and other nonlinear processing applications.

In materials with inversion symmetry such as silica fiber, the majority of nonlinear effects originate from the third-order susceptibility $\chi^{(3)}$. An example is a third-order nonlinear attenuation commonly referred to as a Two-Photon Absorption (TPA). The TPA process offers an excellent alternative [12] for SHG based high-speed signal processing since the material attenuation due to TPA process is proportional to the optical intensity squared:

$$\alpha_{NL} = \beta I^2 \qquad \text{where} \qquad \beta = 24\pi^2 \frac{\varpi}{n^2 c^2} \cdot \mathrm{Im}(\chi^{(3)}) \tag{2-2}$$

Other important $\chi^{(3)}$ nonlinearities are Kerr nonlinear refraction, Four Wave Mixing (FWM) and Raman scattering. Kerr nonlinear refraction is an intensity dependent refractive index change leading to Self-Phase Modulation (SPM), Cross-Phase Modulation (XPM) and self-focusing (Kerr lensing). The FWM is a special case of the frequency generation, where two frequency components ν1 and ν2 propagates in the material resulting in a creation of two new frequencies: ν3=ν1−(ν2−ν1)= 2ν1−ν2 and ν4=ν2+(ν2−ν1)= 2ν2−ν1. The importance of this process results from the fact that the new components lies around the spectral range of the original components. This can result in FWM cross-talk between different wavelength channels in WDM system and optical power fluctuations between channels. The Raman scattering originates from an interaction of the propagated beam with the crystal or glass lattice. It results in transforming of some part of the energy into a longer wavelength accompanied with emission of an optical phonon. This effect can be employed for Raman amplification and Raman lasers.

2.3. Optical Timing Extraction

Timing extraction, or clock recovery, which retrieves the timed clock from the received optical signal, is one of the key functions for constructing high-speed optical transmission systems. A number of optical transmission elements such as optical regenerators, add/drop multiplexers and demultiplexers require accurate clock signals. Requirements for optical timing extraction include fast operation, low-phase noise, high sensitivity and polarisation independence. To increase the operating speed, many approaches based on photonic technology have been studied.

The first approach was to use an optical tank circuit that features a high speed operation and a simple configuration originating from its passive structure. This technique was employed for clock recovery from 2 Gb/s optical data [13]. Another approach, called injection locking, utilizes a self-pulsating LD, whose output repetition frequency is locked to that of an injected optical pulse train. A wavelength and polarisation insensitive clock recovery, based on self-pulsating DFB-LD was developed and tested in 10 Gb/s, 105 km transmission experiment [14]. Recently self-pulsating quantum dot Fabry-Perot laser was employed to retrieve 40 GHz clock signal from injected 40 Gb/s, 80 Gb/s and 160 Gb/s signals [15]. Probably the most mature method utilizes a Phase-Locked Loop (PLL) circuit with electrical Voltage-Controled Oscilators (VCO). This technique benefits from several advantages in that it has no phase-error, and complete retiming is possible, in principle. The conventional PLL circuit speed is limited due to the microwave mixer used as a phase comparator to approximately 40 Gb/s. New cross-correlation techniques based on photonics are investigated to overcome this problem. The first experiment has been conducted using a Travelling Wave Semiconductor Optical Amplifier (TW-SOA) as an optical phase correlator [16]. Because the SOA gain is instantaneously modulated by the intense optical clock, the cross-correlation between the signal and the clock (driven by a VCO) can be obtained all-optically. The cross-correlated signal can be measured with a conventional low speed detector, the output of which is returned to the VCO to close the PLL.

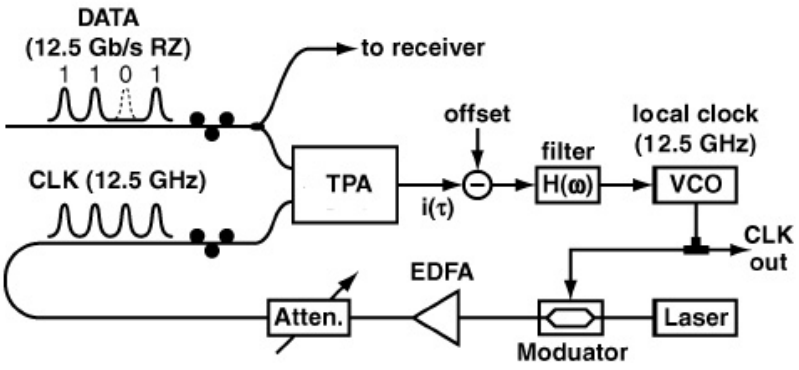

Figure 2-2 Optical clock recovery system based on TPA in Si-APD

A similar approach was proposed using Two-Photon Absorption [17] in a configuration shown in Figure 2-2. The reference clock and data are combined in a 50/50 coupler and focused on a Silicon Avalanche-Photodiode (SI-APD). The averaged nonlinear TPA photocurrent is a measure of both signals cross-correlation. The photocurrent contains a nonzero background level since both data and clock signal can each separately produce TPA even when they are non-overlapped. This constant offset is subtracted from the output of the TPA detector and the resulting cross-correlation signal passes through a feedback filter and is used to control the frequency of the VCO. The feedback filter was designed so that the closed-loop transfer function would have a third-order low-pass response with a bandwidth of around 10 kHz. This approach can be extended to ultra-high rates and wide wavelength ranges. This makes it an attractive candidate for future high-speed communications systems.

2.4. Optical Switching

Optical switches are key devices for ultra-fast transmission systems realizing principle networking functions such as channel add/drop processing and signal full-demultiplexing. All-optical, stable bit-error-free, polarisation independent techniques are desired for future communications systems. The first high-speed optical switching operation was demonstrated with an optical Kerr switch [18]. An optical signal was launched into a birefringent fiber at 45° with respect to the birefringent axes. A control pulse, co-propagating with the optical signal, was coupled into the fiber along one of the birefringent axes causing a nonlinear refractive index change (Kerr nonlinear refraction) along the axis. The fiber length and the control signal power were chosen to achieve 90° polarisation flip between the signal propagated alone and the signal co-propagating with the control pulse. A polarization analyzer was used to separate both polarisations resulting in an ultra-fast all-optical switch. To compensate for PMD the fiber was cut in the middle and spliced at 90°. However it is difficult for the Kerr switch to operate without polarization dependence.

Another method is the use of the FWM process that occurs in silica fibers or SOAs. The first error-free, polarization independent 100 to 6.3 Gb/s demultiplexing was demonstrated utilizing FWM in a 3km polarization maintaining fiber loop [19]. Moreover a FWM-based multiple-output 100 Gb/s demultiplexing was achieved employing a linearly chirped square-pump pulse [20]. Four OTDM channels were simultaneously converted through FWM into four different wavelength channels. Other promising approaches to create a simple optical switch involve XPM-induced frequency shift [21], and Nonlinear Optical Loop Mirror based on a Sagnac interferometer [22]. The NOLM is based on the nonlinear refraction in optical fiber. It consists of a 50/50 fiber coupler with its two outputs joined by a certain length of nonlinear optical fiber. When an OTDM signal is injected into an input port of the coupler, it splits into two counter-propagating components in the fiber loop.

Since both components experience the same phase shift propagating in the loop, when recombined in the coupler, the overall signal is output through its initial input port. If now a high power control signal is directly coupled into the loop, such that it co-propagates with one of the split signals, synchronized with one of the OTDM data channels, then the phase shift induced by the control results in that particular channel being output to the second input port of the coupler. If the nonlinear fiber is replaced by an SOA such a configuration is called a Terahertz Optical Asymetric Demultiplexer (TOAD) [23]. Recently, interferometric devices (Mach-Zehnder and Sagnac interferometers) with integrated SOAs where realized as switching elements for OTDM experiments [24].

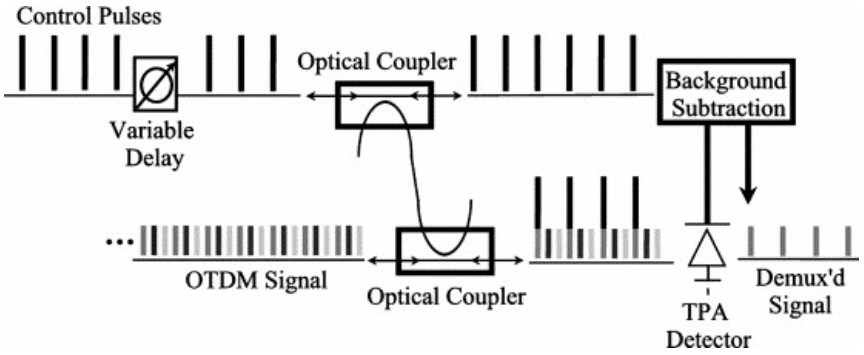

Figure 2-3 Schematic of TPA Demultiplexing

Although NOLM and TOAD-based demultiplexers have demonstrated all-optical demultiplexing in systems operating at up to 640 Gbit/s, a number of factors limit the performance of these devices. For example, high speed switching in the NOLM requires specialty fiber and precise wavelength control of signal and control pulses about the fiber zero-dispersion wavelength, while with TOAD, gain depletion in the SOA has been shown to limit the minimum control pulse width and thus the maximum switching speed. Because of these limitations of presently available all-optical switches, it is important to consider alternative optical nonlinearities for ultra-fast switching. An all-optical demultiplexing might be carried out using optical pulses to switch out data from a single channel in a high-speed OTDM system using a TPA effect in a semiconductor device [25]. The example configuration that was used in [26] is shown in Figure 2-3.

2.5. High-Speed Signal Characterization

Generation and accurate characterization of ultra-short optical pulses is essential to obtain high-speed optical transmission. Optical signals can be successfully characterized at rates up to 40 Gb/s involving fast photodetection. Measured intensity can be displayed on an oscilloscope in real time, providing an excellent method for optical pulse analysis. Figure 2-4 a) plots example oscilloscope trace of 500 MHz pulses generated using external-injection, Fabry-Perot (FP) laser gain-switching

(GS) technique with linear chirp compression. Important signal properties such as peak intensity rise/falling times, period, temporal and amplitude jitter can be read directly from the oscilloscope trace. Optical pulse duration in an experimental arrangement is commonly measured as a Full Width at Half Maximum (FWHM). Pulse FWHM is commonly desired to be less the 1/3 signal period in RZ transmission systems. Pedestal Suppression Ratio (PDSR) measures the suppression of any undesirable features just before or after the pulse. PDSR is important when pulses are placed close together such as in OTDM Systems. If the PDSR is not high enough it can lead to Inter Symbol Interference (ISI). Extinction ratio is the relative intensity of the `ON' state to the `OFF' state. In communication systems a high extinction ratio reduces the Bit Error Rate (BER) by making 1's and 0's more distinct. Consequently a high extinction ratio is usually desirable.

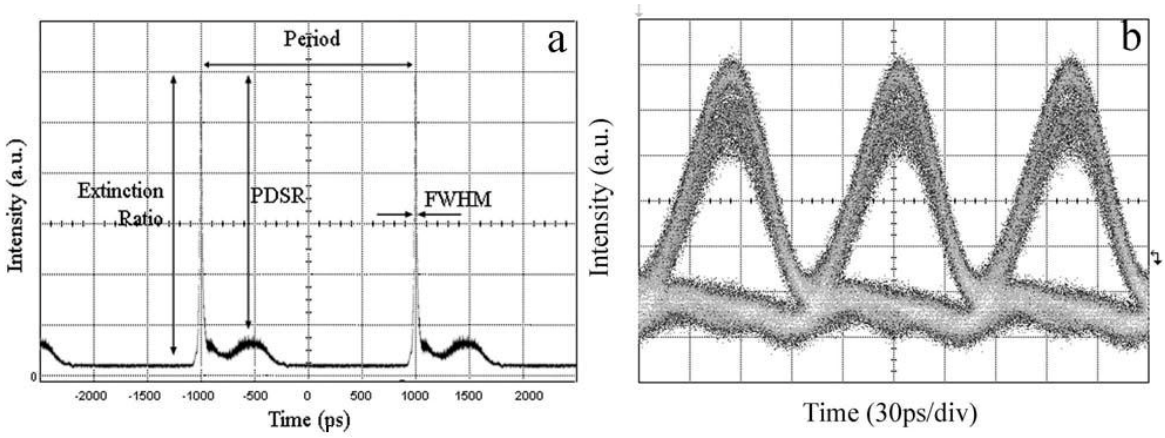

Figure 2-4 a) Oscilloscope trace of 500MHz pulses from externally injected GS FP laser with linear chirp compression, b) Eye diagram of 10 Gb/s RZ signal from TMLL followed by MZ modulator

A data signal is commonly displayed on the oscilloscope as an eye diagram. Figure 2-4 b) plots an example eye diagram of 10Gb/s RZ signal obtained from Gain-Switched pulse source with external injection. The generated 5ps RZ data pulses were passed through a 40km SMF and than compressed back to 5ps with DCF. The transmitted signal was displayed on the low-bandwidth oscilloscope. Important signal features such as one and zero level noise or temporal jitter can be estimated from the diagram. It can be seen that the speed (bandwidth) of the photodetector-oscilloscope system is not sufficient to measure the incident pulse width correctly. The original 5 ps pulse is displayed on the oscilloscope as approximately 40 ps wide. This is due to a limited optical-to-electrical conversion speed. With current speed of electronics it is difficult to characterize pulses shorter then approximately 10ps. It can be achieved involving all-optical techniques based on optical nonlinearities.

An autocorrelation is a simple all-optical technique for the real time measurement of optical pulses with durations in the femtosecond to picosecond range. In this technique, the short light pulse is

divided by a splitter into two beams, each of which travels a different path length. A variable optical delay line in one of the arms provides the time difference τ between the two beams which are focused onto a nonlinear detector, commonly a SHG crystal, TPA photodetector or FWM SOA. The nonlinear response as a function of the scanning delay provides the temporal characteristic of the optical pulse trains with pulses as short as a few femtoseconds. There are two types of autocorrelation which differ in how the two light beams are recombined. Most deployed SHG devices utilize non-collinear light beams, crossing within the crystal to generate background-free intensity autocorrelation signal. This results in intensity correlation signal:

$$S_1(\tau) \propto \int p(t)\,p(t-\tau)dt \tag{2-3}$$

where p(t) is a temporal power envelope of the incident signal under test. The background-free autocorrelation is defined completely by the pulse's intensity and all phase information is lost. The collinear SHG autocorrelation, by contrast, contains the background of the co-propagating beams which interfere with the SHG product causing fringes. This is also the case in the TPA semiconductor autocorrelation [12]. The measured autocorrelation trace has the form:

$$S_2(\tau) \propto \int \left|\left(E(t) + E(t-\tau)\right)\right|^2 dt \tag{2-4}$$

where E(t) is the incident signal electric field. Several methods of subtracting the pulse phase information from the above trace have been reported including Fringe-resolved Autocorrelation (FRAC) [27][28]. However, since a very precise, sub-wavelength stability with a slow optical delay control is required most of the deployed autocorrelators provides the pulse intensity information only. This technique is easy to integrate in an experimental arrangement offering inexpensive, robust and sensitive, real-time pulse intensity measurement.

A drawback of the autocorrelation technique is that for any autocorrelation trace there exists an infinite number of possible pulse shapes. The accurate pulse measurement is only possible when the pulse shape is known. This problem can be resolved with optical sampling [29] technique where the signal under test is cross-correlated with an optical gate pulse using a nonlinear detector, resulting in cross-correlation trace:

$$S_3(\tau) \propto \int p(t)\,p_G(t-\tau)dt \tag{2-5}$$

Alternatively the optical gate can be formed by an electro-optic modulator followed by a linear detector. Again the gate signal is scanned across the signal under test using electric phase, or optical time delays. If the gate signal is much shorter then the signal under test, the cross-correlation trace

is a unique representation of the pulse intensity profile. This is the principle of the operation of many optical oscilloscopes. The main difficulty is that the optical gate has to be shorter than the measured pulse to achieve adequate resolution, and only the intensity profile can be measured with phase information being lost.

A complete pulse characterisation including both intensity and phase information of the signal can be represented in a chronocyclic space. This is a time-frequency distribution containing information about when and in what frequency, energy exists in the signal. A spectrogram is a common time-frequency distribution representation, where Fourier transforms of short signal sections, in a temporal domain are successively taken. Similarly an inverse Fourier transform can be taken of successive small sections (or bands) of the signal in the frequency domain. This is called a sonogram however both approaches are equivalent. The spectrogram can be represented by a general equation:

$$P(\tau,\varpi) \propto \left| \int E(t)G(t-\tau)\exp(-i\omega t)dt \right|^2 \tag{2-6}$$

where E(t) is the tested signal temporal field and G(t) is the gate signal used to cut the temporal section of E(t). A large number of approaches were proposed to measure spectrograms of ultra-fast signals. One way is to use a nonlinear interaction between two or more optical signals referred to as an optical gating technique. In Frequency Resolved Optical Gating (FROG) [30] the tested signal autocorrelation is obtained using a SHG crystal. Next the Fourier transform of the SHG signal is measured for each autocorrelation step using a spectrometer. This is one of the most powerful pulse measurement techniques, which is still one of the best methods for ultra short pulse measurement. From the measured spectrogram the pulse phase and intensity can be retrieved.

2.6. Performance Monitoring

A transmitted optical signal suffers from various impairments during propagation in an optical system. These impairments will need to be monitored in order to allow for adaptive compensation. The Optical Performance Monitoring (OPM) element must possess some ability to make time domain measurements. The most straightforward way to achieve this functionality is to perform a high-speed optical-to-electrical (O/E) conversion and to then make measurements on the resulting electrical signal. Although very powerful, the high-speed O/E conversion introduces much of the complexity and high cost of an optical receiver, especially problematic at data rates exceeding 40 Gb/s. An attractive alternative offers a nonlinear optical detection capable to provide comprehensive ultra-fast signal quality information in a cost effective manner. In the field of ultra-fast optics, nonlinear effects such as SHG, TPA and FWM are commonly used as a tool to make

time-domain measurements. In the previous section the value of nonlinear detection for a temporal-characterisation of optical pulse trains was presented. A number of powerful techniques allowing for ultra short signal intensity and phase characterisation were discussed. Although these measurements are invaluable laboratory tools, nonlinear detection can be used to provide powerful characterization of optical signals without the use of any temporal scanning elements. In this section the applications of nonlinear detection for ultra-short pulse time domain characterisation are introduced.

2.6.1. Time Domain Measurements

Optical signals are commonly defined by an incident optical signal electric field temporal fluctuation given by:

$$E(t) = A(t)\cos(\omega_0 t + \varphi) = \mathrm{Re}\{A(t)\exp(i\varphi)\exp(i\varpi_0 t)\} \tag{2-7}$$

where A(t) is a slowly varying amplitude, ω_0 is the optical signal carrier angular frequency and φ is the signal phase. The right side of the equation (2-7) is commonly referred to as a complex notation and is used due to its mathematical simplicity. The rapidly varying sinusoidal part in many cases may be omitted resulting in the optical signals described by a slowly varying complex amplitude, and optical power envelope, given by respectively:

$$\overline{A(t)} = A(t)\exp(i\varphi) \quad ; \quad p(t) = \frac{1}{2}A(t)^2 = \frac{1}{2}\left|\overline{A(t)}\right|^2 \tag{2-8}$$

where brackets |…| refers to a modulus of a complex number. The most general nonlinear detector is defined as any device that produces a nonlinear signal proportional to:

$$S_{NL} \propto \int p(t)^2 dt \tag{2-9}$$

where p(t) is the time-varying power envelope of the optical signal. The efficiency of the process is determined by quantities such as volume of the active region and nonlinearity of the medium. In many cases it depends also on the polarization state of the signal resulting in the device polarisation sensitivity.

Let us now consider an optical signal defined as a periodic sequence of optical pulses with a Gaussian power envelope given by:

$$p(t) = \frac{TP_{Av}}{\tau\sqrt{\pi}}\exp\left(-\frac{t^2}{\tau^2}\right) \tag{2-10}$$

where T is the period, P_{Av} is the average power within the pulse and τ is the pulse width parameter related to the power envelope FWHM by: $\tau_{FWHM}=1.665\tau$. If the signal period T is greater than pulse width $T>\tau$, the response of the nonlinear detector can be written as:

$$S_{NL} \propto \frac{1}{T}\int_{-T/2}^{T/2} p(t)^2 dt = \frac{T}{\sqrt{2\pi\tau}} P_{Av}{}^2 \qquad (2\text{-}11)$$

The ratio τ/T is commonly defined as a duty cycle d of the signal and the square root of 2π is the proportionality constant associated with the Gaussian pulse shape. The problem with different proportionality constants for different pulse temporal envelopes can be removed by introducing a generalized duty cycle definition given by:

$$d_{gen} = \frac{\langle p(t) \rangle^2}{\langle p(t)^2 \rangle} = \text{ (for Gaussian pulses)} = \frac{\sqrt{2\pi\tau}}{T} \qquad (2\text{-}12)$$

Consequently a nonlinear response for any sequence of optical pulses with power envelope given by p(t) and average power P_{Av}, is inversely proportional to the generalized duty cycle as long as the pulse width is shorter then the signal period T:

$$S_{NL} \propto \frac{P_{Av}^2}{d_{gen}} \qquad (2\text{-}13)$$

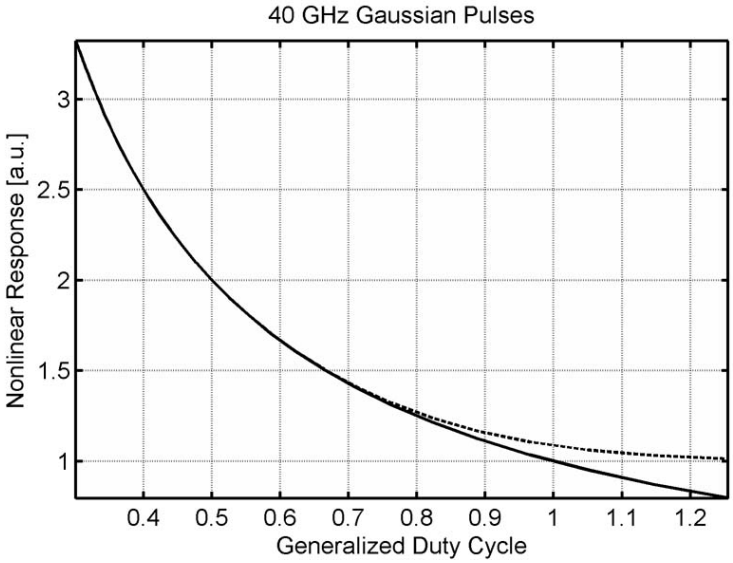

Figure 2-5 Nonlinear response vs. generalized duty cycle of 40 GHz Gaussian pulse signal: solid line - plotted equation (2-13), dashed line - simulated numerically including neighboring pulses overlapping.

A nonlinear response vs. generalized duty cycle for the incident Gaussian pulse sequence is shown in Figure 2-5 where the solid line plots the equation (2-13) in a range from 0.3 to 1.2 generalized duty cycle. This is compared with a dashed curve simulated numerically including the pulse overlapping with the neighbouring pulses. It can be seen that the equation (2-13) calculated analytically accurately describes the nonlinear response as long as the incident pulses are shorter than the signal period: d_{gen}<0.8. Above this threshold level the pulses start to overlap resulting in coherent or incoherent (intensity) interference.

Temporal pulse broadening and consequent pulse overlapping results from various optical transmission impairments. One of the main high-speed systems-limiting impairments is Chromatic Dispersion (CD) resulting in a temporal broadening of initially Fourier Transform-Limited (FTL) pulses. Since the period of the pulse sequence does not change once the pulses are launched, this leads to an increase in the generalized duty cycle d_{gen} of the signal. The signal measured by a nonlinear detector will therefore change according to equation (2-13) as a function of the net accumulated dispersion through which the pulses have propagated. This method is inherently scalable to high bit-rates and is fundamentally asynchronous, requiring no clock recovery. The applicability of this technique for ultra-high speed measurements arises from the extremely short nonlinear response time, rather than from the electrical bandwidth of the nonlinear detection scheme. The only constraint on the electrical bandwidth of the detection scheme is that it be sufficient to track changes in the duty cycle that occur on the time scale of interest.

For a sequence of optical pulses that contains digital data encoded into RZ or NRZ format, the quantity of interest is not the duty cycle for a single bit, but rather it is this quantity averaged over many ones and zeros in a binary sequence. For common data sequences where there is an approximately equal distribution of ones and zeros, the generalized duty cycle averaged over the data stream will therefore be half that envisioned when considering only a single bit.

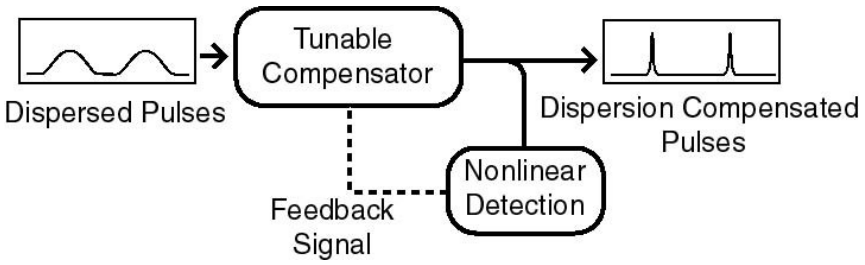

Figure 2-6 Adaptive dispersion compensation scheme involving nonlinear detection in a feedback loop

CD is commonly compensated in optical systems involving dispersion management, however additional temporal fluctuations resulting from varied environmental conditions may still limit the system performance. A real-time CD monitoring and dynamic compensation is required to ensure the maximum transmission link performance. Dynamic pulse dispersion compensation may be achieved involving nonlinear detection with a feedback loop to a tunable dispersion compensation element. An example of a monitoring and compensation configuration is shown in Figure 2-6.

The ability to provide meaningful accumulated dispersion measurements is less efficient for the case of NRZ optical signals. This is due to the so-called “ears” that form on the edges of NRZ signals during the propagation through a dispersive medium. Although dispersion causes optical

power to spread and increase the duty cycle, the ear formation leads to localized high peak powers and high nonlinear response. The net result of these two competing effects is that the nonlinear signal is only weakly sensitive to dispersion for the NRZ case. The overall transmission tolerance for CD, however for NRZ signals is larger then RZ signals due to its reduced bandwidth.

2.6.2. OSNR Measurements

The use of in-line optical amplifiers has enabled long-haul optical communication systems, but the cascading of a large number of amplifiers introduces Amplified Spontaneous Emission (ASE) noise into the optical signal and degrades OSNR of the signal. The OSNR is commonly estimated using spectral measurements made by an Optical Spectrum Analyser (OSA). Since the OSA can not measure the in-band ASE noise level it is estimated by interpolation of an ASE level measured on either side of a channel slightly outside of its bandwidth. This technique has limited accuracy since optical signals are commonly passed through a number of optical band-pass filters during the propagation, reducing only the out-of-band ASE noise. Consequently the in-band noise commonly exceeds the out-of-band ASE level. This motivates the investigation into alternative schemes to measure the in-band OSNR level such as polarization measurements [31],[32] and pilot tones [33]. In this section an approach based on nonlinear detection will be discussed.

The average optical power transmitted in the RZ format is shared between the optical coherent signal carrying the information and noncoherent noise added to the signal during the amplification process. A ratio between the energy in the signal and in the noise is referred to as Optical Signal to Noise Ratio (OSNR). This can be measured using a nonlinear detection since the nonlinear response varies between the incident sinusoidal waveform and random noise of the same average power. Let us first consider an optical sinusoidal Continuous Waveform (CW) described by an electric field temporal dependence:

$$E_{CW}(t) = \sqrt{2P_{Av}}\cos(\varpi_0 t) \tag{2-14}$$

where ω_0 is the angular frequency and P_{Av} is the CW signal average power defined as:

$$P_{Av} \propto \left\langle E_{CW}(t)^2 \right\rangle = \frac{1}{T}\int_T E(t)^2 dt \tag{2-15}$$

where the brackets <> correspond to the temporal averaging and $T=2\pi/\omega_0$ is the CW signal period. An average nonlinear response for such a signal is then:

$$S_{CW} \propto \left\langle E_{CW}(t)^4 \right\rangle = \frac{3}{2}P_{Av}^2 \tag{2-16}$$

Let us now consider the noise that has a Gaussian probability density function with zero mean. The probability P(E) that the electric field at any arbitrary time falls in the range E to E+dE is given by:

$$P(E)dE = \frac{1}{\sqrt{2\pi}\sigma}\exp\left(-\frac{E^2}{2\sigma^2}\right)dE \tag{2-17}$$

where σ^2 is the noise standard variance. The average noise power can be then represented as:

$$N_{Av} = \int_{-\infty}^{\infty} E^2 P(E)dE = \sigma^2 \tag{2-18}$$

The nonlinear response for the noise signal is given by:

$$S_{Noise} \propto \left\langle E(t)^4 \right\rangle = \int_{-\infty}^{\infty} E^4 P(E)dE = 3N_{Av}^2 \tag{2-19}$$

Comparing equations (2-16) and (2-19), it can be seen that the noise signal generates twice the nonlinear response of that generated by the sinusoidal signal. The same conclusion, confirmed experimentally, was obtained in similar analysis carried out in [34]. The same calculations can be carried out for combined noise and CW signals to obtain relations for combined average power:

$$P_{CW+Noise} = \left\langle \left(E_{CW}(t) + E_{noise}(t)\right)^2 \right\rangle = P_{Av} + N_{Av} \tag{2-20}$$

and the combined nonlinear response:

$$S_{CW+Noise} = \left\langle \left(E_{CW}(t) + E_{noise}(t)\right)^4 \right\rangle = \frac{3}{2}P_{Av}^2 + 3N_{Av}^2 + 6P_{Av}N_{Av} \tag{2-21}$$

where $E_{Noise}(t)$ is the (random) noise electric field temporal variation, described by the probability density function given by equation (2-17). If we define the OSNR as a ratio between the CW and noise average optical powers, the equation (2-21) can be rewritten as:

$$S_{CW+Noise} = \left(3 - \frac{3}{2}\left(\frac{OSNR}{OSNR+1}\right)^2\right)P_{CW+Noise}^2 \tag{2-22}$$

This shows the nonlinear detection potential for OSNR measurements. In telecommunication systems where optical signal is modulated for example in the form of optical pulses, the signal can be decomposed into number of spectral components. Any spectral component can be filtered out from the signal using a narrow-band optical filter. The nonlinear detection S_{NL} can be then used to measure the OSNR within the narrow-band spectral range around the filtered component. This is shown in a schematic setup in Figure 2-7. This technique can be used to scan the signal spectrally to measure OSNR across the signal frequency components.

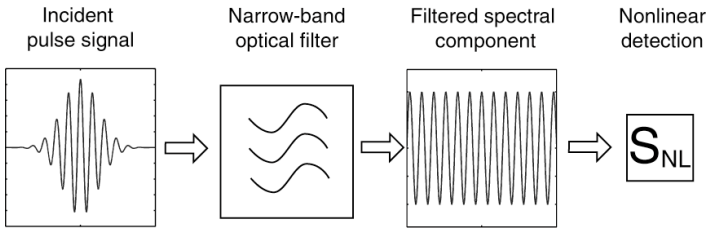

Figure 2-7 Nonlinear OSNR measurements of a narrow-band spectral component of the pulsed signal

The applicability of this technique was tested employing a numerical simulation. The simulation was carried out for a 160 GHz, Gaussian pulse sequence operating at 1550nm wavelength. The simulated pulse-train (power envelope) is plotted in Figure 2-8 a) for a pure signal (infinity OSNR). The corresponding optical spectrum is plotted in Figure 2-8 b). The central frequency component was then cut out from the spectrum through a simulated 160 GHz bandwidth square filter. The nonlinear response was calculated for the resulting sinusoidal signal for different OSNR. Note that OSNR in this case is a ratio between the average power of the filtered spectral component and the noise average power within the filtered narrow-band spectral range. Figure 2-8 c) plots the simulation results (square points) versus OSNR, compared with a plot of the equation (2-22) obtained analytically (solid line). An excellent fit between the numerical simulation and the equation can be seen.

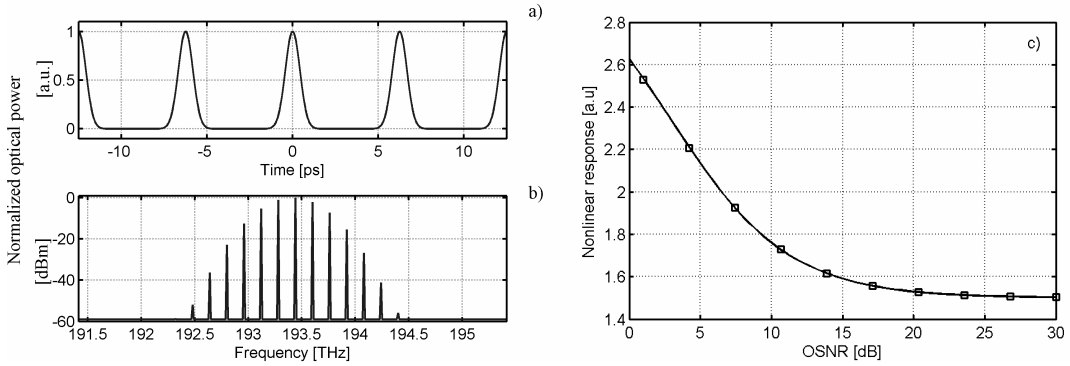

Figure 2-8 In-band OSNR measurement of 160 GHz signal spectral component: a) incident 160 GHz RZ Gaussian pulse sequence power envelope, b) incident signal spectral components, c) nonlinear response vs. OSNR within 160 GHz in-band range around filtered central spectral component calculated analytically (solid line) and simulated numerically (square points)

2.6.3. Extinction Ratio Measurements

In communications systems some part of the signal energy can be transmitted as a constant coherent background. Constant background occurs for example in a transmitter consisting of CW laser followed by external modulator curving the constant waveform in order to encode data. Some applications such as all-optical label switching involving orthogonal label technique requires a certain level of a constant background to encode an optical label for switching purposes. The ratio between the signal peak power and the constant background power is commonly measured with an extinction ratio parameter. This can be measured involving a nonlinear detection. Let us consider an optical signal consisting of Gaussian optical pulses, sitting on a constant coherent background:

$$E(t) = \sqrt{2P(t)}\cos(\varpi_0 t) \tag{2-23}$$

$$P(t) = \frac{TP_{pulse}}{\tau\sqrt{\pi}}\exp\left(-\frac{t^2}{\tau^2}\right) + P_{Bground} \tag{2-24}$$

where P(t) is the signal power envelope, P_{pulse} is the average optical power within the pulses, T is the signal period, τ is the pulse width parameter and $P_{Bground}$ is the constant background optical power. The extinction ratio for such a signal can be written as:

$$ER = \frac{P(t=0)}{P_{Bground}} = \frac{TP_{pulse}}{\tau\sqrt{\pi}P_{Bground}} + 1 \tag{2-25}$$

The average linear P_{Av} and nonlinear S_{NL} responses, in τ<T range, are proportional respectively to:

$$P_{Av} \propto \left\langle E(t)^2 \right\rangle = P_{pulse} + P_{Bground} \tag{2-26}$$

$$S_{NL} \propto \left\langle E(t)^4 \right\rangle = \frac{3}{2}\left(\frac{T}{\tau\sqrt{2\pi}}P_{pulse}^2 + 2P_{pulse}P_{Bground} + P_{Bground}^2\right) \tag{2-27}$$

The nonlinear response S_{NL} from the equation (2-27) can be rewritten by substituting ER, P_{av} and generalized duty cycle d_{gen} resulting in:

$$S_{NL} \propto \left[\left(\frac{1}{d_{gen}} - 1\right)\left(\frac{\sqrt{2}}{d_{gen}(ER-1)} + 1\right)^{-2} + 1\right] \cdot \frac{3}{2}P_{Av}^2 \tag{2-28}$$

The nonlinear detection sensitivity for the incident signal extinction ratio ER is clear from the above equation. It should be noted that the nonlinear response would be different than shown in equation (2-28) if the background light was formed by an ASE noise instead of the constant sinusoidal waveform. According to equations (2-16) and (2-19) ASE noise generates twice as much nonlinear response as continuous sinusoidal waveform of the same average power. If we define ASE extinction ratio as:

$$ER_{ASE} = \frac{P(t=0)}{P_{ASE\_Bground}} \tag{2-29}$$

the nonlinear response can be calculated for an incident average optical power (P_{Av}):

$$S_{NL}^{ASE} = \left[\left(\frac{1}{2d_{gen}} - 1\right)\left(\frac{\sqrt{2}}{d_{gen}ER_{ASE}} + 1\right)^{-2} + 1\right]3P_{Av}^2 \tag{2-30}$$

The above equation shows the applicability of the nonlinear detection for the signal extinction ratio measurements where background light is formed by ASE noise. Figure 2-9 compares nonlinear response calculated for CW background (solid line) according to the equation (2-28) with the case of the ASE background (dashed line) according to the equation (2-30). Calculations were carried for an example of 0.3 generalized duty cycle of Gaussian pulse sequence. The same analysis was

carried out numerically with the results plotted for CW background (square points) and ASE background (diamond points) in Figure 2-9.

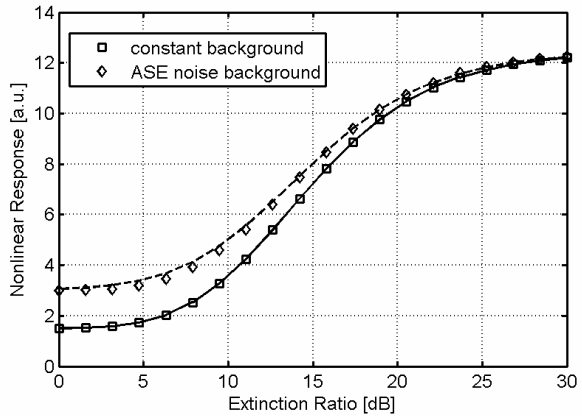

Figure 2-9 Nonlinear response vs. incident signal extinction ratio of Gaussian pulse train for coherent and ASE backgrounds, calculated for dgen=0.3, and PAv=1, solid line - plot of the equation (2-28) for the case of coherent background, dashed line – plot of equation (2-29) for the case of ASE background, dots and diamond points – corresponding numerical simulations

According to the expectations for a zero extinction ratio signal (background only) the nonlinear response due to the ASE background is twice that of CW background. In both cases the agreement between the analytical and numerical results is excellent.

2.7. Summary

Optical nonlinearities offer an attractive alternative for electronic signal processing techniques in ultra-fast communications. Important networking functions including optical clock recovery and optical switching can be realized employing optical nonlinearities. Nonlinear detection offers a powerful tool for ultra-short pulse characterization and real-time performance monitoring. This would be required in future optical systems for adaptive transmitted signal regeneration. Transmission impairments resulting in temporal pulse broadening, in-band OSNR degradation and extinction ratio degradation can be monitored employing optical nonlinearities.

Commonly used optical nonlinearities for ultra-fast signal processing are SHG, TPA and FWM in optical fibers, semiconductors and optical crystals. The TPA process in a semiconductor microcavity structure offers attractive advantages for future ultra-fast signal processing techniques. The principles of the TPA process and microcavity design will be discussed in the following chapter.

References

[1] A. H. Gnauck, G. Raybon, S. Chandrasekhar, J. Leuthold, C. Doerr, L. Stulz, E. Burrows, "25x40-Gb/s copolarized DPSK transmission over 12x 100-km NZDF with 50-GHz channel spacing," *IEEE Photonics Technology Letters*, vol. 15, pp. 467-469, 2003.

[2] T. Mizuochi, K. Ishida, T. Kobayashi, J. Abe, K. Kinjo, K. Motoshima, K. Kasahara, "A comparative study of DPSK and OOK WDM transmission over transoceanic distances and their performance degradations due to nonlinear phase noise," *IEEE Journal of Lightwave Technology*, vol. 21, pp. 1933-1943, 2003.

[3] R. E. Tench, J.-M.P. Delavaux, L. D. Tzeng, R. W. Smith, L. L. Buhl, and R. C. Alferness, "Performance evaluation of waveguide phase modulators for coherent systems at 1.3 and 1.5 pm," *IEEE Journal of Lightwave Technology*, vol. LT-5, pp. 492-501, 1987.

[4] L. Xu, B. C. Wang, V. Baby, I. Glesk, and P. R. Prucnal, "All-optical data format conversion between RZ and NRZ based on a Mach-Zehnder interferometric wavelength converter," IEEE *Photonics Technology Letters*, vol. 15, pp. 308-310, 2003.

[5] T. Kawanishi, T. Sakamoto, and M. Jzutsu, "All-optical modulation format conversion from frequency-shift-keying to phase-shift-keying by using optical double-sideband modulation technique," *in Conference on Lasers and Electro-Optics (CLEO'05)*, Paper CWO1, 2005.

[6] K. Mishina, A. Maruta, S. Mitani, T. Miyahara, K. Ishida, K. Shimizu, T. Hatta, K. Motoshima, K. Kitayama, "All-optical format conversion from NRZ-OOK to RZ-BPSK using SOA-MZI wavelength converter," *in conference on Optical Fiber Communication (OFC'06)*, paper OThB2

[7] P.A. Franken, AE. Hill, C.W. Peters, and G. Weinreich, "Generation of optical harmonics," *Physical Review Letters*, vo1.7, no.4, pp. 118-119, 1961

[8] J.C. Diels, E.W. Van Stryland, D. Gold, "Investigation of the parameters affecting subpicosecond pulse durations in passively mode locked dye lasers," *in Conference on Picosecond Phenomena*, Springer-Verlag, pp.117-120, 1978

[9] Yuzo Ishida, Kazunori Naganuma, Tatsuo Yajima, "Self-phase Modulation in Hybridly Mode-Locked CW Dye Lasers," *IEEE Journal of Quantum Electronics*, vol.21, pp. 69-77, 1985

[10] A. S. Weling and D. H. Auston, "Novel sources and detectors for coherent tunable narrow-band terahertz radiation in free space," *Journal of Optical Society of America B*, vol.13, no.12, 1996

[11] S. Akturk, M. Kimmel, and R. Trebino, "Ultrasimple FROG device for measuring ultrashort pulses at 1.5-micron wavelengths," *IEEE Lasers and Electro-Optics Society 17th Annual Meeting* (LEOS'04) vol.2, pp. 737-138, 2004.

[12] Yoshihiro Takagi, Tohru Kobayashi, Keitaro Yoshihara, "Multiple- and single-shot autocorrelator based on two-photon conductivity in semiconductors," *Optics Letters,* vol.17 no.9, pp.658-660, 1992

[13] M. Jinno and T. Matsumoto, "Optical tank circuits used for all-optical timing recovery," *IEEE Journal of Quantum Electronics*, vol. 28, pp. 895–900, Apr. 1992.

[14] B. Sartorius, C. Bornholdt, O. Brox, H. J. Ehrke, D. Hoffmann, R. Ludwig, and M. Möhrle, "All-optical clock recovery module based on self-pulsating DFB laser," *IEEE Electronics Letters*, vol. 34, pp. 1664–1665, 1998.

[15] V. Roncin, A. O'Hare, S. Lobo, E. Jacquette, L. Bramerie, P. Rochard, Q.-T. Le, M. Gay, J.-C. Simon, A. Shen, J. Renaudier, F. Lelarge, and G.-H. Duan "Multi-Data-Rate System Performance of a 40-GHz All-Optical Clock Recovery Based on a Quantum-Dot Fabry–Pérot Laser," *IEEE Photnics Technology Letters*, v.19, n.19, 2007

[16] S. Kawanishi and M. Saruwatari, "New-type phase-locked loop using travelling-wave laser-diode optical amplifier for very high-speed optical transmission," *IEEE Electronics Letters*, vol. 24, pp. 1452–1453, 1988.

[17] Reza Salem, T. E. Murphy, "Broad-Band Optical Clock Recovery System Using Two-Photon Absorption," *IEEE Photnics Technology Letters*, v.16, n.9, 2004

[18] T. Morioka, M. Saruwatari, and A. Takada, "Ultrafast optical multi/demultiplexer utilizing optical Kerr effect in polarization-maintaining single-mode fibres," *IEEE Electronics Letters*, vol. 23, pp. 453–454, 1987.

[19] T. Morioka, S. Kawanishi, K. Uchiyama, H. Takara, and M. Saruwatari, "Polarisation-independent 100 Gbit/s all-optical demultiplexer using four-wave mixing in a polarisation-maintaining fiber loop," *IEEE Electronics Letters*, vol. 30, pp. 591–592, 1994.

[20] T. Morioka, S. Kawanishi, H. Takara, and M. Saruwatari, "Multiple output, 100 Gbit/s all-optical demultiplexer based on multichannel four-wave mixing pumped by a linearly-chirped square pulse," *IEEE Electronics Letters*, vol. 30, pp. 1959–1960, 1994.

[21] T. Morioka, K. Mori, and M. Saruwatari, "Ultrafast polarisation-independent optical demultiplexer using optical carrier frequency shift through crossphase modulation," *IEEE Electronics Letters,* vol. 28, pp. 1070–1072, 1992.

[22] K.J. Blow, N.J. Doran, and B.P. Nelson, "Demonstration of the nonlinear fibre loop mirror as an ultrafast all-optical demultiplexer," *IEEE Electronics Letters*, vol. 26, pp. 962–964, 1990.

[23] J.P. Sokoloff, P.R. Prucnal, I. Glesk, M.P. Kane, "A terahertz optical asymmetric demultiplexer (TOAD)," *IEEE Photonics Technology Let*ters vol.5, no.7, pp. 787-790, 1993

[24] W. Pieper, E. Jahn, M. Eiselt, R. Ludwig, R. Schnabel, A. Ehrhardt, H. J. Ehrke, and H. G. Weber, "System applications for all-optical semiconductor switching devices," *in Photonic Network Communications, Springer-Verlag*, 1997, p. 473.

[25] B.C Thomsen, J.M. Dudley, J.D. Harvey, L.B. Barry, "Demonstration of demultiplexing in high speed OTDM systems using a two photon absorption based switch," *in conference on Optical Fiber Communication (OFC'01)*, vol.3, pp.WO2-1-WO2-3, OFC 2001

[26] P.J. Maguire, L.P. Barry, T. Krug, M. Lynch, A.L. Bradley, J.F. Donegan, H. Folliot, "Simulation of a high-speed demultiplexer based on two-photon absorption in semiconductor devices," *Optics Communications*, vol. 249, no.4-6, 2005, pp.415-420

[27] J.C. Diels, E.W. Van Stryland, D. Gold, "Investigation of the parameters affecting subpicosecond pulse durations in passively mode locked dye lasers," *in Conference on Picosecond Phenomena*. Berlin, West Germany: Springer-Verlag, 1978, pp.117-120

[28] Peter M. W. Skovgaard, Rory J. Mullane, David N. Nikogosyan and John G. McInerney, "Two-photon photoconductivity in semiconductor waveguide autocorrelators," *Optics Communications* vol.153, pp.78-82, 1998

[29] K. Kikuchi, "Optical sampling system at 1.5um using two photon absorption in SI avalanche photodiode," *IEEE Electronics Letters*, vol.34, no.13, pp. 1354-1355

[30] D. J. Kane and R. Trebino, "Characterization of arbitrary femtosecond pulses using frequency-resolved optical gating," *IEEE Journal of Quantum Electronics*, v.29, no.2, pp. 571-579, 1993.

[31] M. Petersson, H. Sunnerud, B.-E. Olsson, and M. Karlsson, "Multichannel OSNR monitoring for WDMnetworks," *in European Conference on Optical Communication (ECOC'02)*, vol.1, pp. 1-2, paper 1.1.6, 2002

[32] M. Rasztovits-Wiech, M. Danner, W.R. Leeb, "Optical signal-to noise ratio measurement in WDM netwodks using poralisation Extinction," *in European Conference on Optical Communication (ECOC'98)*, vol.1, pp:549 – 550, 1998

[33] G. Bendelli, C. Cavazzoni, R. Girardi, and R. Lano, "Optical performance monitoring techniques," *in European. Conference on Optical Communication* (ECOC'00), vol. 4, pp. 113–116, 2000

[34] W.H. Guo, J. O'Dowd, M. Lynch, A.L. Bradley, J.F. Donegan, L.P. Barry and D.C. Kilper, "Two-photon absorption generated by optically amplified signals," *IEEE Electronic Letters*, vol.44, no. 18, pp. 1087-1088, 2008

CHAPTER 3. Two-Photon Absorption microcavity

3.1. Introduction

Two-Photon Absorption (TPA) is a potential candidate for all-optical signal processing alongside other nonlinearities such as Second Harmonic Generation (SHG) or Four Wave Mixing. A TPA photodetector generates nonlinear photocurrent directly, removing the necessity of using an additional photodetector like in the case of SHG systems. TPA detector sensitivity can be increased significantly by incorporating Resonant Cavity Enhancement (RCE) structures. An additional advantage of the RCE TPA photodetector is a resonance characteristic offering a great potential for use in multi-wavelength systems. In this chapter the principles of the TPA process and basics of the RCE will be given in sections 3.1 and 3.2. In section 3.3 fabricated devices structures will be described and in section 3.4 initial device characterizations will be shown.

3.2. Two-Photon Absorption

Two-Photon Absorption (TPA) is an optical nonlinear process where two photons are absorbed to excite a molecule to a higher energy state. The TPA process was discussed theoretically for the first time by Maria Goeppert-Mayer in 1931 [1] and experimentally demonstrated by Kaiser and Garret [2] in 1961. In their experiment a CaF_2:Eu2+ crystal structure was illuminated with red light (694.3 nm) from ruby maser. The crystal is fully transparent for incident red light, however combined two-photon energy corresponds to strong Eu2+ ions absorption wavelength range. The TPA process excited the crystal to the higher energy level and then the fluorescent decay to a lower state was observed around 420 nm. Due to very high crystal symmetry this experiment differs from the Franken's Second Harmonic Generation (SHG) [3] within quartz waveguide, demonstrated in the same year. Since the second-order susceptibility $\chi^{(2)}$ nonlinear effects (e.g. SHG) occur only in materials that lack inversion symmetry, the third-order $\chi^{(3)}$ TPA process was employed to describe the observed blue radiation correctly.

The TPA imposed loss has been recognized as a limiting factor in many optical applications including all-optical switching in waveguides and spatial soliton break-up in glass waveguides. In contrast nonlinear photoconductivity associated with TPA can be applied for a number of all-optical signal processing techniques. TPA occurs in semiconductor bulk or quantum materials where the TPA process excites electrons from the valence to the conductive band. In such case two photons are absorbed simultaneously to generate a single electron-hole pair. This process is much weaker than linear absorption, but if the semiconductor band gap energy is greater than single photon energy the linear absorption is significantly suppressed. However if the band gap energy is still

lower than combined two-photon energies then the TPA process can occur to generate electron-hole pairs. Single-Photon Absorption (SPA) process efficiency P_{SPA} is proportional to the photon density which in turn is proportional to the optical intensity. The efficiency of TPA process P_{TPA}, where two single photons are absorbed at the same time, is proportional to the square of the optical intensity.

$$P_{TPA} = P_{SPA}^2 \propto I^2 \tag{3-1}$$

The absorption proportionality constants for SPA and TPA processes are commonly referred to as α and β coefficients respectively. When both coefficients are known the intensity propagation I(z) along the z axis of semiconductor waveguide can be found by solving a differential equation:

$$\frac{dI(z)}{dz} = -\alpha I(z) - \beta I(z)^2 \Rightarrow I(z) = I_0 \frac{\exp(-\alpha z)}{1 + \frac{\beta I_0}{\alpha}\left[1 - \exp(-\alpha z)\right]} \tag{3-2}$$

where I_0 is the incident optical intensity. The TPA photo-detector can be realized using a p-i-n structure where an intrinsic semiconductor active region is placed between two p- and n- doped layers. The generated electron-hole pairs are separated by electric field existing across the intrinsic active region resulting in current flow in an external circuit. The total absorption within the active region of length L can be written as:

$$I_{abs} = I_0 - I(L) = I_{SPA} + I_{TPA} \tag{3-3}$$

where I_{SPA} and I_{TPA} refers to absorption resulting from SPA and TPA processes respectively. These can be written after [4] as:

$$I_{SPA} = I_{abs} \frac{\alpha L}{\alpha L + \ln C} \qquad I_{TPA} = I_{abs} \frac{\ln C}{\alpha L + \ln C} \tag{3-4}$$

where C=1+(βI0/α)(1-exp(-αL)). The generated photocurrent after propagation through the length L of the active region can be then calculated as:

$$J = \frac{eSI_0}{h\nu}\left(A_{SPA} I_{SPA} + \tfrac{1}{2} A_{TPA} I_{TPA}\right) \tag{3-5}$$

where S is the illuminated area and the photoconductivity coefficients A_{SPA}, A_{TPA} are the probabilities of an electron-hole pair generation after SPA and TPA process respectively. The equation (3-5) assuming 100% photoconductivity efficiency (A_{SPA}=A_{TPA}=1) within 1μm length waveguide is plotted in Figure 3-1 versus incident optical power, given by a product of incident intensity I_0 and illuminated area S. From the plot a dynamic range, in which generated photocurrent is proportional to the square of the incident optical power can be seen. It is limited by SPA which becames dominant at low incident optical powers, and total absorption at high optical powers. The dynamic range can be improved by decreasing α/β ratio or increasing the length of the waveguide. Although the level of calculated photocurrent is impressive it should be noted that it is overestimated due to assumed 100% photoconductivity efficiency, and other simplification

assumptions. The above calculations, however, show the applicability of the TPA process in a semiconductor waveguide for all-optical signal processing.

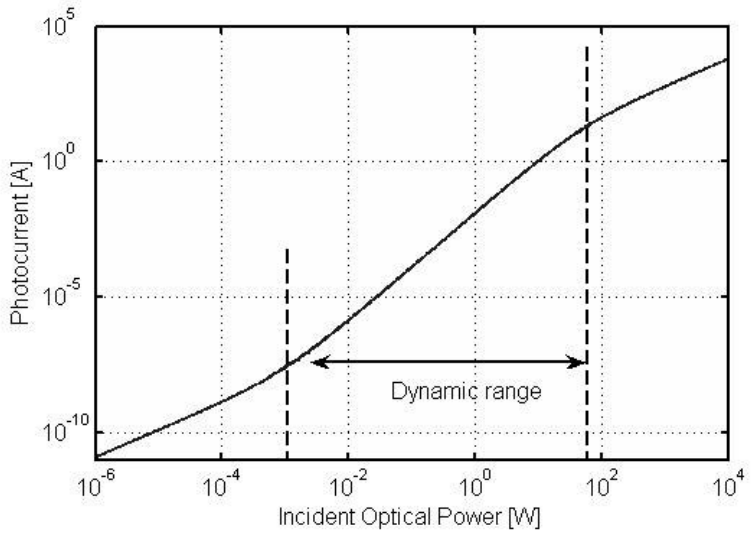

Figure 3-1 Photocurrent versus incident optical power for an L=1μm semiconductor waveguide of S=1μm2 illuminated area, for α=0.1cm-1, β=0.02cm/MW,ASPA/TPA=1 and 1550nm incident wavelength

For high-speed switching applications ultra-short device response time is required, which puts a limit on the device length and cross-section area. The shorter length reduces carrier drift time to the contacts and smaller area reduces the device capacitance. These however decrease the amount of generated photocurrent and sensitivity of the device. A way to enhance the response time while maintaining high TPA photocurrent is to use a microcavity semiconductor structure. This will be discussed in the following section

3.3. Microcavity Structure

High-speed, sensitive photodetectors are crucial for optical communications systems. Various photodetectors such as avalanche photodiodes, p-i-n photodiodes, heterojunction phototransistors, and metal-semiconductor-metal photodiodes have been extensively studied. The efficiency of optical-to-electrical (OE) conversion of conventional photodetector is limited by absorption coefficient, thickness of the active layer, and surface reflection. To achieve high efficiency, a thick high-absorption active layer along with antireflection coating is essential. This however inherently reduces photodetector speed due to longer transit times in depletion region. Therefore, it is desirable to enhance quantum efficiency while keeping the active layer thin. This can be achieved by incorporating a multiple pass detection scheme, in which a single active layer serves many times in generating photocarriers. In this scheme, the detection region is integrated between two mirrors made of quarter-wave stacks. The incoming light is partially reflected by the front mirror but the

transmitted part at resonance condition, interferes constructively within the cavity. Due to successive reflections the optical field within the cavity builds up (and decays) gradually, and can nearly reach the level of the incoming light. The build-up time is measured with the cavity lifetime (or photon lifetime) parameter. This cavity enhancement can be described using an impulse response description. Suppose we launch into the cavity an optical pulse which, as far as the cavity response is concerned, is very narrow. Mathematically the incident, sharp pulse is described using Dirac's delta function δ(x) that has the value zero everywhere except at $x = 0$ where its value is infinitely large in such a way that its total integral is 1. The cavity broadens the incident pulse due to the successive reflections resulting in a pulse of definite shape. The appearing pulse is described by the cavity impulse response h(t), also normalized due to the energy preservation principle

The pulse duration can be characterized using root-mean-square (rms) width of the power envelope A(t) defined as the square root of its time variance [5]:

$$\sigma = \sqrt{\langle t^2 \rangle - \langle t \rangle^2} \tag{3-6}$$

where

$$\langle t^n \rangle = \frac{1}{N} \int_{-\infty}^{\infty} t^n A(t) dt \quad \text{where} \quad N = \int_{-\infty}^{\infty} A(t) dt \tag{3-7}$$

The rms width is a useful quantity since it gives an integral measure of the temporal distribution of the pulse energy. It can be shown that any pulse having rms pulse width σ_1 that passes through a linear system whose impulse response h(t) has rms width of σ_2 will emerge with an rms width σ_3 given by:

$$\sigma_3 = \sqrt{\sigma_1^2 + \sigma_2^2} \tag{3-8}$$

The cavity lifetime τ_{cavity} is commonly defined as the rms width of the cavity impulse response h(t) or equivalently as the average time required for photons to make one round trip in the optical cavity divided by loss uncounted during this round trip. Sometimes a notation borrowed from conventional resonator description is used where resonant property is described by a resonance quality factor (or Q-factor). Q-factor is given by the optical power stored in a cavity divided by the power dissipated per cycle. For a high Q-factor cavity (high mirror reflectivities and thin absorption region) a high ratio between resonance and off-resonance frequencies enhancement can be obtained. High quality resonance cavity corresponds to the longer cavity lifetime and narrower resonance peak. The cavity frequency enhancement characteristic is referred to as the cavity frequency response H(f) or the cavity field transfer function. The functions h(t) and H(f) are in fact related by a Fourier transform that is:

$$H(f) = \int_{-\infty}^{\infty} h(t)\exp(-i2\pi ft)dt \tag{3-9}$$

The Full Width at Half Maximum (FWHM) of the cavity power transfer function $|H(f)|^2$ is referred to as the cavity Bandwidth.

The cavity performance is commonly evaluated with the quantum efficiency parameter η defined as a ratio between optical power within the cavity and the incident optical power. A theoretical analysis of RCE linear detector was carried out for the first time by Kishino et. al. in [6] using cavity model shown in Figure 3-2 a).

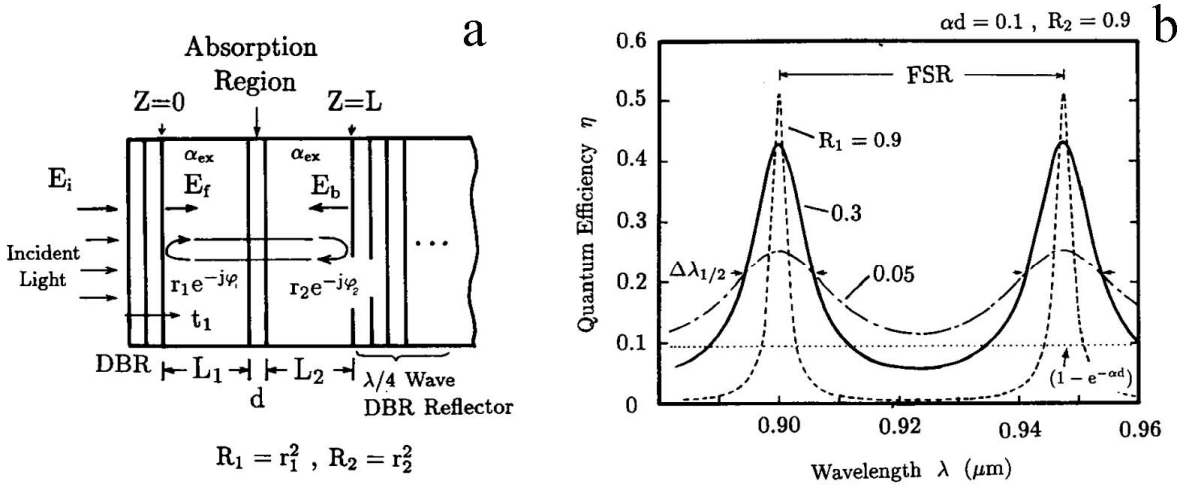

Figure 3-2 a) Model of a resonance cavity detector, b) Resonance cavity quantum efficiency vs. incident wavelength

The cavity shown consists of the active region, with linear absorption (loss) α and thickness d, sandwiched between two external layers of thickness L and quarter wave Bragg reflectors. The Bragg mirrors are described by field reflectivities $r_{1/2}\exp(-i\,\psi_{1/2})$. In practical detector design the material around the active layer absorbs negligibly compared to the active layer thus the external layer absorption α_{ex} can be neglected in most designs. Assuming the propagation constant β is the same along all cavity layers an approximated formula for quantum efficiency can be found:

$$\eta = \left(\frac{1+R_2e^{-\alpha d}}{1-2\sqrt{R_1R_2}e^{-\alpha d}\cos(2\beta L+\Psi_1+\Psi_2)+R_1R_2e^{-\alpha d}}\right)(1-R_1)\left(1-e^{-\alpha d}\right) \tag{3-10}$$

where $R_{1/2}$, are front and back mirrors power reflectivities, $\psi_{1/2}$ are corresponding phase shifts due to light penetrating into multilayer mirrors structure and α is the linear absorption within the active region of thickness d. The equation (3-10) is accurate for analysis of RCE linear detectors except for the case of an extremely thin active layer or extremely thick external layer. A more precise description including different propagation constants in active and external layers, and considering

a standing wave effect was shown in [7]. From the equation (3-10), where the propagation constant β is a function of wavelength $\beta=2\pi n/\lambda$ where n is the material refractive index, η is a periodic function of the inverse wavelength. This is easily seen in Figure 3-2 b) which illustrates, after [6], the calculated wavelength dependency of η for varied front mirror reflectivity, while $R_2=0.9$, $\alpha d=0.l$, and $L=2\mu m$ is fixed. The quantum efficiency reaches its maximum at the resonance wavelengths determined by $2\beta L+\psi_1+\psi_2=2\pi m$ (m=1,2,3…). The wavelength spacing between neighboring resonant peaks is referred to as the Free Spectral Range (FSR). The obtained quantum efficiency wavelength dependence is equivalent to the cavity power transfer function $|H(f)|^2$, where $\lambda=c/f$ (c is the speed of light). The cavity bandwidth may be defined as the FWHM of the quantum efficiency resonance peak, denoted as $\Delta\lambda_{1/2}$ in Figure 3-2 b). A finesse F defined as the ratio of the FSR to the cavity bandwidth measures the cavity wavelength selectivity:

$$F = \frac{FSR}{\Delta\lambda_{1/2}} \tag{3-11}$$

High finesse cavity photodetectors are desired for multi-wavelength applications e.g. in WDM systems, to avoid cross-channel interference.

A microcavity structure was proposed to enhance the TPA process within a nonlinear photodetector [8]. High nonlinear response at resonance wavelength, in conjunction with reduced active region length and thus the photodetector capacitance, allows for high speed signal processing. Accurate description of such a device requires consideration of intensity-dependant nonlinear absorption in the active region and carrier-induced change in the refractive index. A model based on the transfer matrix method (TMM) was developed in [8]. A theoretical simulation was carried for an AlGaAs/GaAs cavity with band-gap around 700nm. A TPA response for 900 nm incident optical pulse was modeled for two microcavity devices and non-cavity device with an equivalent length. The results are shown after [8] in Figure 3-3 where calculated TPA photocurrent is plotted versus incident intensity. The photocurrent values on the left hand side of the plot are normalized by the device cross-section area. The measurable average photocurrent is displayed on the right hand side of the plot. From the results a dramatic improvement in generated photocurrent but lower dynamic range is seen for the microcavity devices. The upper limit of the dynamic range is not due to the total absorption but the generated carrier refractive-index change in the structure. High carrier concentration changes the propagation constant within the cavity and thus shifts the resonance wavelength. Consequently the dynamic range is limited by the carrier-induced refractive index change at high optical intensities.

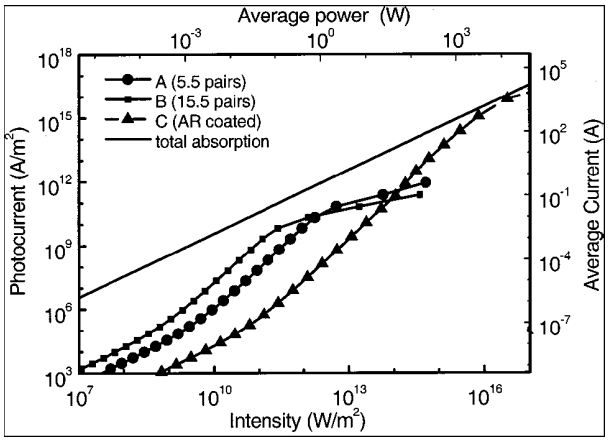

Figure 3-3 Theoretical compare of TPA photocurrents generated from traveling-wave and microcavity photodetectors

From the equation (3-10) it can be seen that the resonance wavelength depends on the cavity length and phase shifts induced by the front and back mirrors. These can be varied by rotating incident angle thus allowing for a resonance wavelength tuning of the microcavity detector. This tunable RCE device wavelength selectivity is an additional advantage that removes the necessity of using external optical filters in multi wavelength applications. This will be discussed in section 3.4.3.

A common problem associated with TPA process is its polarization sensitivity. This problem becomes even more complex when microcavity structure is used. Additional strain introduced during microcavity device growing results in microcavity device birefringence and as a consequence the cavity shows different properties depending on the incident polarisation state. This results in microcavity resonance wavelength shift and optical bandwidth change. If the microcavity device is considered to operate at different than normal incidence angle two additional polarization modes can be distinguished for which the electric field of the light waves lies in the same plane as the incident ray and the surface normal. The two modes interact with lateral periodic structures in a different way resulting in further increase of the device polarisation sensitivity.

3.4. TPA Microcavity Design

In previous sections a potential of Resonant Cavity Enhanced (RCE) devices for fast signal processing was explained. By placing an active region inside a Fabry-Perot microcavity, the photodetector structure benefits from a high resonance enhancement from short device. The increased optical field allows RCE photodetector to be thinner and therefore faster. Molecular Beam Epitaxy (MBE) provides a growth technique capable of producing Fabry-Perot microcavities within exacting specifications enabling the realization of RCE devices. The performance of the RCE photodetection scheme depends critically on the realization of a low loss cavity. This dictates that

both the mirror and cavity material must be non-absorbing at the detection wavelength and that the mirrors have high reflectivity. The materials composing the mirror must be well lattice matched to avoid the introduction of defects into the active layer. Low number of mirror-periods is desired to simplify growing procedure and to reduce the device series resistance. Thus it is desirable to have as large a refractive index difference as possible between the mirror layers. Various materials suitable for realization of RCE photonics devices are overviewed in [9].

In this work a specially designed TPA microcavities using material combination of AlGaAs/GaAs/AlGaAs were fabricated and characterized before experimental implementation for nonlinear signal processing applications. The devices were intended to operate around 1.55μm telecommunication window thus the active material bandgap energy had to be greater then incident photon energy of:

$$E_{photon} = \frac{hc}{\lambda} = 0.8eV \tag{3-12}$$

but less then $2E_{photon}$. This condition holds for GaAs with bandgap energy of Eg=1.42eV. In addition GaAs active region is nearly transparent and have large TPA nonlinear absorption coefficient β=0.02 cm/MW around 1.55 μm [10]. The cavity length and Bragg mirrors period were designed to enhance optical wavelengths around 1.55μm. The material system chosen benefits from simplicity with which heterostructures can be grown using MBE. Additionally GaAs has good electronic properties, reasonably low carrier recombination rates, and excellent lattice matching to AlAs. Because of the fine lattice match, AlGaAs alloys across the entire range are easily incorporated as wide bandgap contact layers and graded heterojunctions. GaAs and AlAs also have a good refractive index contrast which allows a mirror of nearly unity reflectivity to be realized with a twenty period quarter wave superlattice. A number of samples were fabricated on a commercial market based on three RCE designs. Detailed information about the structures is given in Table 3.1 and Table 3.2.

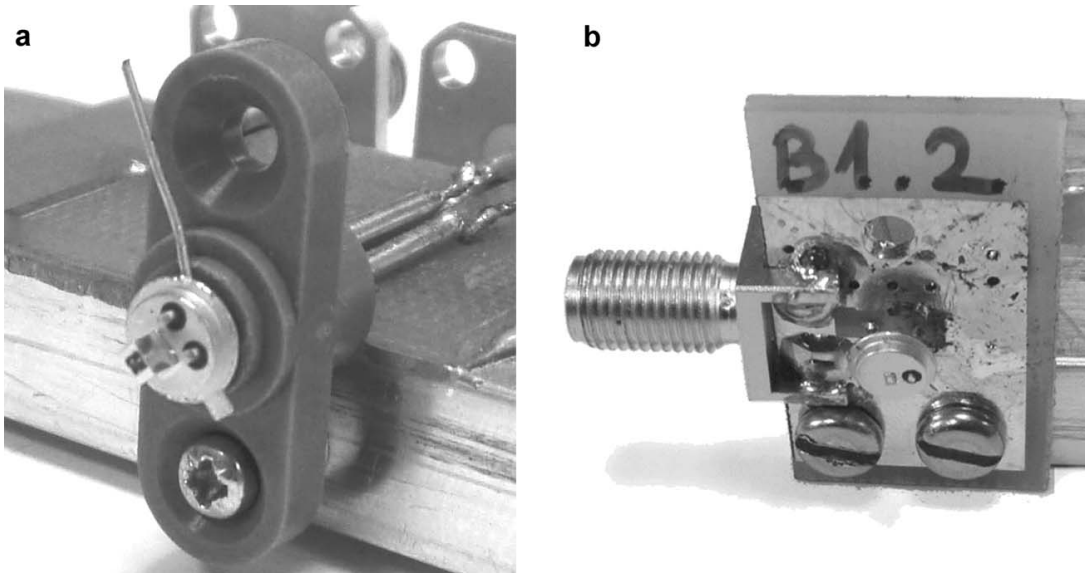

Figure 3-4 TPA microcavity device mounts

Material	Loops	Thicknes (nm)	Doping(cm^{-3})	Dopant
GaAs		115.6	$2.5 \cdot 10^{19}$	Carbon (p)
AlAs		134.8	$3 \cdot 10^{18}$	Carbon (p)
$Al_{(0.12)}GaAs$	x6	117.8	$1 \cdot 10^{18}$	Carbon (p)
AlAs		134.8	$1 \cdot 10^{18}$	Carbon (p)
GaAs	x6	115.6	$3 \cdot 10^{17}$	Carbon (p)
AlAs		134.8	$5 \cdot 10^{17}$	Carbon (p)
$Al_{(0.6)}GaAs$		126.8	$3 \cdot 10^{17}$	Carbon (p)
AlAs		134.8		None
GaAs		**462.5**		**None**
AlAs		134.8	$1 \cdot 10^{18}$	Silicon (n)
$Al_{(0.6)}GaAs$		126.8	$1 \cdot 10^{18}$	Silicon (n)
AlAs	x23	134.8	$1 \cdot 10^{18}$	Silicon (n)
GaAs		115.6	$1 \cdot 10^{18}$	Silicon (n)

Table 3.1 RCE TPA detector designs: no.1 – without 6 layers marked by gray and no.2 – with additional 6 layers.

The first structure top p-doped (Carbon) mirror consists of 7 periods (layers marked in gray were not grown) and the bottom n-doped (Silicon) mirror consists of 23 periods. This cavity was designed to have approximately 1ps cavity lifetime. The second structure has additional 6 highly doped layers marked by a gray color in Table 3.1. Additional layers were meant to increase the top mirror reflectivity, and in consequence the cavity lifetime, to approximately 8ps. The third structure consists of the top p-doped mirror consisting of 21 periods and the bottom n-doped mirror consists

of 25 periods. High doping of the top layers in both designs allows for better bonding of contacts. The third structure design avoids abrupt transitions from GaAs to AlAs and has an order of magnitude greater doping of the top transition layers compared to the first and second structures, in order to reduce resistance and thus increase the device speed.

TPA microcavity devices fabricated from the three designs were mounted on translation stage allowing for accurate device alignment with focusing lens. Most of characterization work was carried out utilizing a photodiode socket shown in Figure 3-4 a, allowing for easy change between different devices. High speed measurements were carried out using especially designed circuits with minimized path lengths (see Figure 3-4 b).

Material	Loops	Thicknes (nm)	Doping(cm^{-3})	Dopant
GaAs		97.9	$1.4 \cdot 10^{19}$	Carbon (p)
$Al_{(0.9 \rightarrow 0.12)}GaAs$		20	$\cdot 10^{18}$	Carbon (p)
$Al_{(0.9)}GaAs$		112.4	$\cdot 10^{18}$	Carbon (p)
$Al_{(0.12 \rightarrow 0.9)}GaAs$		20	$\cdot 10^{18}$	Carbon (p)
$Al_{(0.12)}GaAs$		99.7	$\cdot 10^{18}$	Carbon (p)
$Al_{(0.9 \rightarrow 0.12)}GaAs$		20	$\cdot 10^{18}$	Carbon (p)
$Al_{(0.9)}GaAs$	x16	112.4	$\cdot 10^{18}$	Carbon (p)
$Al_{(0.12 \rightarrow 0.9)}GaAs$		20	$\cdot 10^{18}$	Carbon (p)
$Al_{(0.12)}GaAs$		99.7	$\cdot 10^{18}$	Carbon (p)
$Al_{(0.9 \rightarrow 0.12)}GaAs$		20	$\cdot 10^{18}$	Carbon (p)
$Al_{(0.9)}GaAs$	X2	112.4	$\cdot 10^{18}$	Carbon (p)
$Al_{(0.12 \rightarrow 0.9)}GaAs$		20	$\cdot 10^{18}$	Carbon (p)
$Al_{(0.12)}GaAs$		99.7	$\cdot 10^{18}$	Carbon (p)
$Al_{(0.9 \rightarrow 0.12)}GaAs$		20	$\cdot 10^{18}$	Carbon (p)
$Al_{(0.9)}GaAs$		112.2		None
$Al_{(0.12 \rightarrow 0.9)}GaAs$		20		None
GaAs		447		None
$Al_{(0.9 \rightarrow 0.12)}GaAs$		20		None
$Al_{(0.9)}GaAs$		112.4		None
$Al_{(0.12 \rightarrow 0.9)}GaAs$		20		None
$Al_{(0.12)}GaAs$	x25	99.7	$\cdot 10^{18}$	Silicon (n)
$Al_{(0.9 \rightarrow 0.12)}GaAs$		20	$\cdot 10^{18}$	Silicon (n)
$Al_{(0.9)}GaAs$		112.4	$\cdot 10^{18}$	Silicon (n)
$Al_{(0.12 \rightarrow 0.9)}GaAs$		20	$\cdot 10^{18}$	Silicon (n)
GaAs		500	$\cdot 10^{18}$	Silicon (n)

Table 3.2 RCE TPA detector design no.3

3.5. TPA Microcavities Characterization

The fabricated devices were initially characterized by undertaking basic tests including PI-curve, resonance characteristic and device bandwidth. It should be noted that the same structure devices varied from one to another due to manufacturing imperfections. In addition signal coupling can influence device performance, which was observed in experimental work. Thus even a single device can perform differently depending on the lens used and alignment. This phenomenon may be explained involving Fourier optics analysis since the optical lens basically realizes a Fourier transform of the incident optical signal at the focal plane. The device, placed approximately at the

focal distance from the lens is illuminated by the transformed beam. However if the focused spot size is greater than the device acceptance window, some incoming frequency components will be filtered out. Effectively the device aperture acts as a filter for the incident signal. This can modify the device performance depending on the coupling lens used and the lens alignment. To avoid problems with inconsistent characteristics, devices were always initially characterized before the system measurements. In this section example PI-Curves, resonance characteristics and bandwidth measurements for the three different structures will be discussed. For easier orientation each sample was given a unique name. Experimental results are described including the sample name, structure and an optical source used. For example notation (E, no.2, CW) refers to the sample "E" with design structure no.2 illuminated by a CW source.

3.5.1. PI-Curve

The PI-curve is a basic characterization parameter of nonlinear detectors. The device under test is illuminated with varied optical powers and the generated photocurrent is plotted versus incident optical power. The experimental setup used to characterize devices based on structures no.1 and no.2 is shown in Figure 3-5.

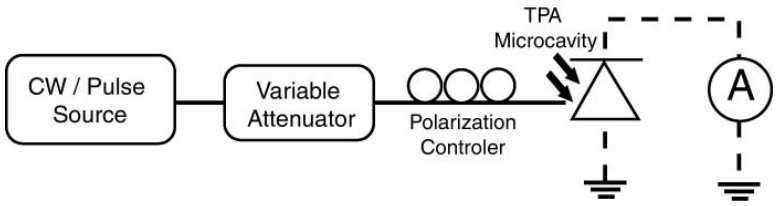

Figure 3-5 Experimental setup to carry a PI-curve characterization of TPA microcavity

The PI-curve is commonly measured utilizing Continuous Waveform (CW) source followed by EDFA. Maximum optical power is limited to approximately 13dBm due to EDFA saturation. Higher optical powers can be obtained utilizing high power laser or EDFA however large CW optical power is destructive for a device under test. Another technique to characterize devices above the EDFA power limit utilizes optical pulses which can easily reach extremely high peak powers while average optical power remains in safe, non destructive ranges. In the experimental setup shown in Figure 3-5, the optical source is followed by variable attenuator and polarisation controller to optimize the incident polarisation state before coupling into the TPA detector, ensuring maximum TPA photocurrent. The light was coupled into the device using an optical lens mounted on xyz transition stage to align it with the device, and the generated photocurrent is measured on a highly sensitive ammeter. Experimental results measured for example samples with structures no.1 and no.2 are plotted in Figure 3-6 a) and b) respectively. No.1 structure sample was characterized with 10 GHz Tunable Mode Locked Laser (TMLL) and 10MHz pulse sources however the sample got damaged before characterizing with CW source. The measurements were limited by a residual

background light in the room, with the lowest detectable photocurrents varying around 1pA depending on the actual conditions.

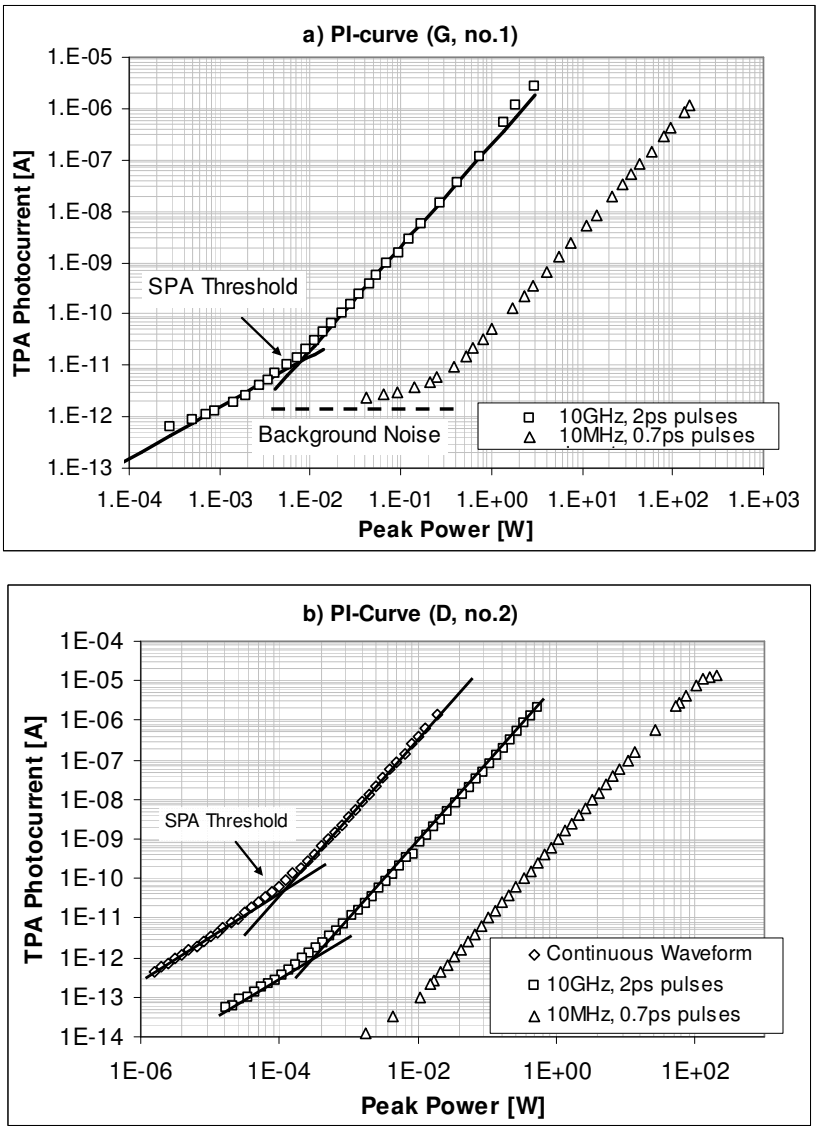

Figure 3-6 PI-curves measured for samples with a) structure no.1 and b) structure no.2

The device with structure no.2 was characterized with CW source and both 10GHz and 10MHz pulse sources. The SPA threshold can be clearly seen for CW and 10GHz results. Supporting solid lines represents slopes of one below the SPA threshold and slopes of two above the threshold respectively. The advantage of using short pulses is that very high optical powers can be obtained however TPA photocurrent is generated only during a short time of the pulse duration. Consequently the measured average photocurrent for a pulse source is scaled by the incident signal duty cycle:

$$J_{pulse} = J_{CW} \cdot d \tag{3-13}$$

where J_{pulse} is the photocurrent generated by incident pulses with peak power P_{pulse} and duty cycle d, and J_{CW} is the photocurrent generated by a CW signal of average power $P_{CW}=P_{pulse}$. Measured TPA photocurrent for incident pulse signal can be though used to evaluate the PI-curve shape above the CW power threshold, simply dividing the results obtained for pulse signal by the operating duty cycle. This method however requires additional correction when RCE detector is used, due to the cavity resonance effect. It was discussed before that the incident optical pulse is modified within the cavity which can be described by the cavity impulse response h(t) or equivalently by the cavity field transfer function H(f). Both approaches gives the same conclusion that optical pulse is broadened within the cavity according to equation (3-8) or simply by considering the cavity as an optical filter where side spectral components of the incident signal are filtered out. Naturally a temporarily-long and spectrally-narrow incident pulse is less affected by the cavity. Consequently the actual average and peak powers within the cavity are decreased by a scaling factor depending on the incident signal bandwidth and the cavity bandwidths ratio. This explains why the SPA thresholds shown in Figure 3-6 b) occur at different peak powers for CW and for the 10GHz pulse sources. In fact the SPE threshold occurs at the same **cavity** peak power which differs from the peak power **in front** of the cavity. The scaling factor between incident and cavity peak powers can be found if the cavity field transfer function H(f) is known. H(f) can be evaluated by carrying out the cavity resonance characteristic which will be discussed in detail in the following section. At the moment we will just say that additional correction factor was used to obtain the actual peak power within the cavity for the two wide-bandwidth pulse sources. Using this correction and dividing the results obtained for pulse signals by its duty cycles aggregated PI curves were evaluated for both structures. The results are plotted in Figure 3-7. Over 5 orders of magnitude dynamic range of the structure no.2 can be seen, limited by the SPA threshold at low incident powers and the carrier-induced refractive index change at high optical powers. Comparing the plots it can be seen that the photocurrent generated by the sample with structure no.2 is an order of magnitude higher than for the structure no.1. This was expected since the structure no.2 has additional layers increasing the quantum efficiency.

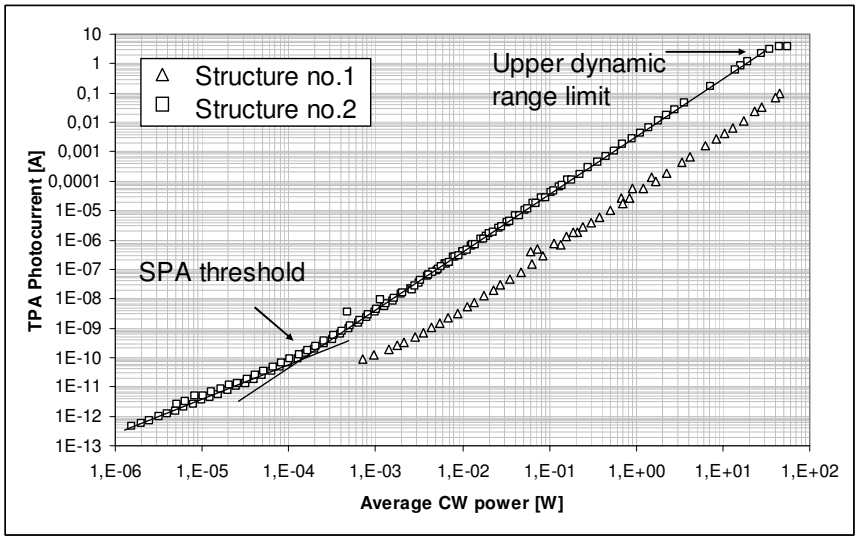

Figure 3-7 TPA photocurrent vs. incident CW optical power evaluated from the results obtained using CW and high power optical pulse sources.

The importance of the evaluated PI-curve arises from the possibility of calculating the TPA response for any incident signal duty cycle. According to the equation (3-13) the TPA photocurrent can be easily found if the device response for incident CW signal of the same average power is known.

The structure no.3 was characterized separately since it differs significantly from the former samples design. The main difference is that the intrinsic region is not fully depleted resulting in a zero potential drop across the active region. The simulated electric potential levels across the sample are viewed in Figure 3-8 a). Samples with this structure design require external reverse bias to separate the generated carriers and move them from the depletion region. The experimental setup used for structure no.3 characterization is shown in Figure 3-8 b).

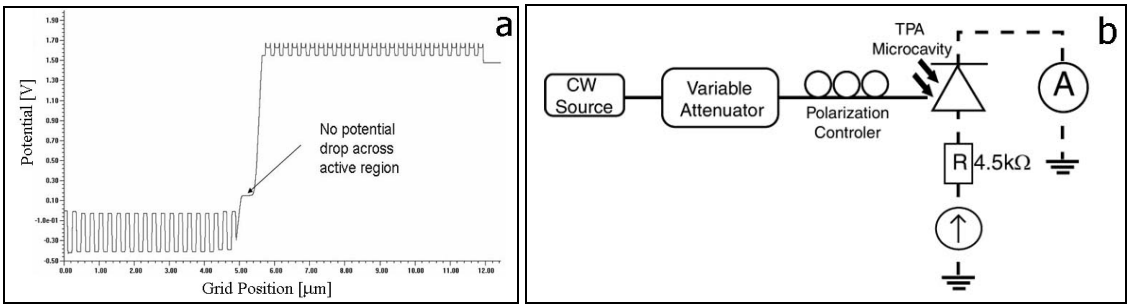

Figure 3-8 (a) Potential levels simulated across structure no.3, (b) PI-Curve characterization experimental setup for sample with structure no.3

A CW source was utilized to measure PI-curves for various bias voltages across the tested sample. An additional resistor was put in series to increase the load of the bias circuit. Pulse characteristics

were not made because of the high risk of samples damage by the high optical peak powers. Results are plotted in Figure 3-8. A dramatic increase in generated photocurrent was observed with increased bias. Excellent nonlinear response was observed for biases up to 0.5 V, however for biases exceeding 0.5 V a background thermal current reduces the device dynamic range at low optical powers. The SPA threshold is not visible since it is hidden below the thermal noise level. From the results the optimal operation bias was found as 0.5V in the tested configuration.

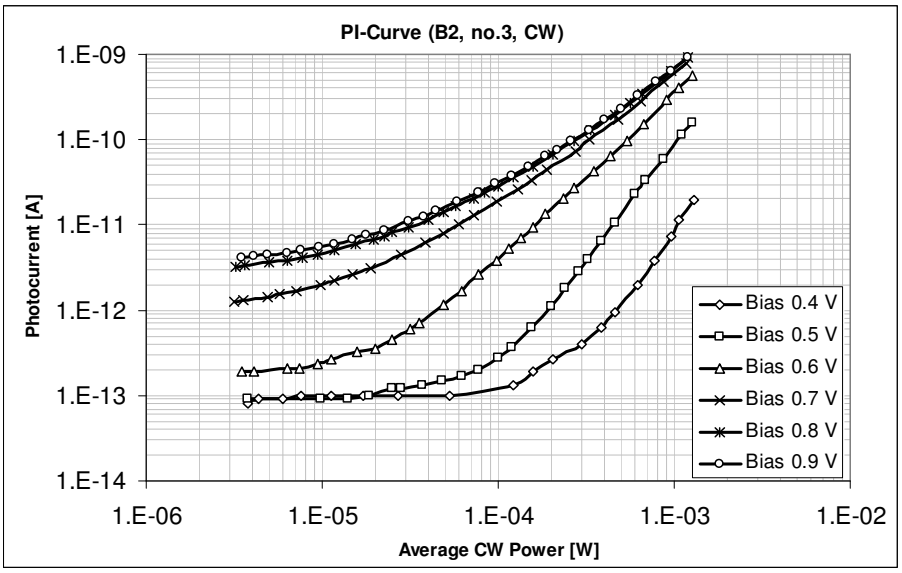

Figure 3-9 PI-curves measured for sample with structure no.3

3.5.2. Resonance Characteristic

Photodetector spectral bandwidth or linewidth is another easy measurable parameter, describing the device wavelength selectivity. To calculate this parameter a quasi-monochromatic CW source can be used to scan the device spectrally around the resonance peak. The cavity modifies the incident signal which is described by the cavity impulse response h(t) in temporal domain or the cavity field frequency response H(f) in spectral domain. H(f) is commonly referred to as the cavity field transfer function and in analogy $|H(f)|^2$ as the cavity power transfer function. Optical power within the cavity plotted versus the incident frequency is called the **cavity resonance characteristic** while the plot of the photocurrent generated versus the incident frequency is referred to as an **RCE device resonance characteristic**. The reason for the difference between these characteristics is due to the nonlinear response of the detector. For linear detectors the photocurrent generated is directly proportional to the optical field within the cavity and consequently the cavity resonance characteristic and the device resonance characteristic have the same shape (proportional to the quantum efficiency shown in Figure 3-2 b). However in the case of nonlinear detectors the photocurrent generated is proportional to the square of the optical power within the cavity and thus the **device** resonance characteristic is proportional to the square of the **cavity** resonance

characteristic. Consequently the device bandwidth is narrower than the RCE cavity bandwidth. In practice the TPA photodetector is nonlinear only above the SPA threshold, and linear at low incident optical powers, below the threshold, due to the SPA process dominating. Thus the **cavity bandwidth** can be measured if the incident optical power is set below the SPA threshold and the **RCE device bandwidth** can be measured by setting optical power above the SPA threshold. This is shown schematically in Figure 3-10

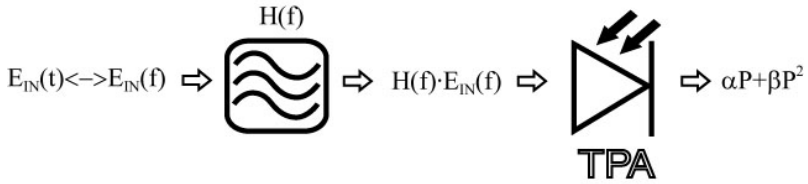

Figure 3-10 schematic equivalent model of TPA RCE device

The incident optical field given by a Fourier-transform pair $E_{IN}(t) \leftrightarrow E_{IN}(\omega)$ is modified by the cavity through the cavity field transfer function H(f). The optical signal within the cavity interacts with a nonlinear medium to generate linear SPA and nonlinear TPA photocurrents, proportional to the optical power and square of the optical power respectively. Here the optical power is given by:

$$P = \frac{n}{2\eta_0}\left|E\right|^2 \tag{3-14}$$

where η_0 and n are the vacuum characteristic impedance of electromagnetic waves and the refractive index of the detector material, respectively. The cavity field transfer function *H(f)* can be approximated by [11]:

$$H(f) = \frac{1}{1+\frac{R}{1-R}\left[1-\exp\left(\frac{i2\pi f}{FSR}\right)\right]} \tag{3-15}$$

where FSR and R are the TPA microcavity Free Spectral Range and the geometric average of the top and bottom mirror reflectivity. The optical field within the cavity in spectral domain $E_C(f)$ can be written as:

$$E_C(f) = E_{IN}(f)\cdot H(f) \leftrightarrow E_C(t) = E_{IN}(t) * h(t) \tag{3-16}$$

The right hand side of equation (3-16) is an equivalent notation in a temporal domain where h(t) is the cavity field impulse response and star denotes the convolution operation. The TPA average photocurrent generated can be written as:

$$I_{TPA}^{Av} \propto \left\langle \alpha\left|E_C(t)\right|^2 + \beta\left|E_C(t)\right|^4 \right\rangle \tag{3-17}$$

where α and β are the SPA and TPA coefficients, brackets |…| denotes modulus operation and <…> denotes time averaging. Assume that monochromatic CW light source operating at frequency f_0 is coupled into the TPA microcavity described by a Fourier pair:

$$E_{IN}(t) = E_0 \cos(2\pi f_0 t) \leftrightarrow E_0 \delta(f - f_0) \tag{3-18}$$

Optical Field within the cavity can be found in frequency and temporal domains respectively:

$$E_C(f) = E_0 H(f) \delta(f - f_0) \leftrightarrow E_C(t) = E_{IN}(t) \cdot H(f_0) \tag{3-19}$$

By substituting (3-19) into (3-17) and neglecting SPA process α=0, the TPA photocurrent can be calculated:

$$I_{TPA}^{Av} \propto \frac{3}{8} \beta P_{Av}^2 \cdot \left| H(f_0) \right|^4 \tag{3-20}$$

where $P_{Av}=|E_0|^2$ is the incident CW light average power and the scaling factor 3/8 results from the time averaging of $<\cos^4()>$.One can include the SPA to obtain:

$$I_{TPA}^{Av} \propto \frac{1}{2} \alpha P_{Av} \left| H(f_0) \right|^2 + \frac{3}{8} \beta P_{Av}^2 \cdot \left| H(f_0) \right|^4 \tag{3-21}$$

From the above equations (3-21) it can be seen that the modulus of the cavity field transfer function can by measured by scanning the device with a wavelength tunable CW source with constant average power. If we normalize the cavity field transfer function so $|H(f_{res})|=1$ where f_{res} denotes the resonance frequency the proportionality constants in equation (3-21) can be evaluated from the previously measured PI curve characteristics.

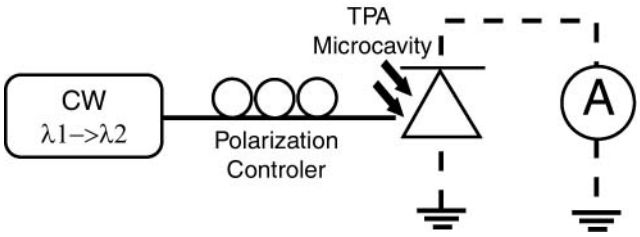

Figure 3-11 Experimental setup to measure devices resonant characteristics

Following the above argumentation the experimental setup to measure the device resonance characteristic is shown in Figure 3-11. A CW laser source used was a tuneable external cavity laser with spectral linewidth of 250 kHz. This was amplified with an EDFA (not shown in figure) and coupled into the device through a polarization controller. Measured characteristics are shown in Figure 3-12. The circle points are experimental results and solid lines are plots of the equation (3-21). For each cavity the field transfer function parameters, R and FSR, were matched to obtain the best fit between the theoretical solid lines and experimental results. The obtained transfer functions are useful to investigate the cavity influence on the devices performance, e.g. to evaluate the actual optical field within the cavity when wide bandwidth pulse source is used. In example this method was used to obtain the aggregated PI-curve characteristics in the previous section. Certain inaccuracy between the theoretical lines and the experimental results can be seen in the resonance characteristics wings. This is due to the EDFA used in the measurements. A small amount of ASE noise generated in the EDFA was coupled into the cavities even when the CW signal was tuned far

away from the resonance wavelength. An EDFA might be also responsible for the small asymmetry of the measured resonance characteristics especially visible for the sample with structure no.2. This is because the CW power before the EDFA was not controlled precisely during the measurements resulting in successive OSNR degradation between CW signal and ASE noise, for tuned wavelengths.

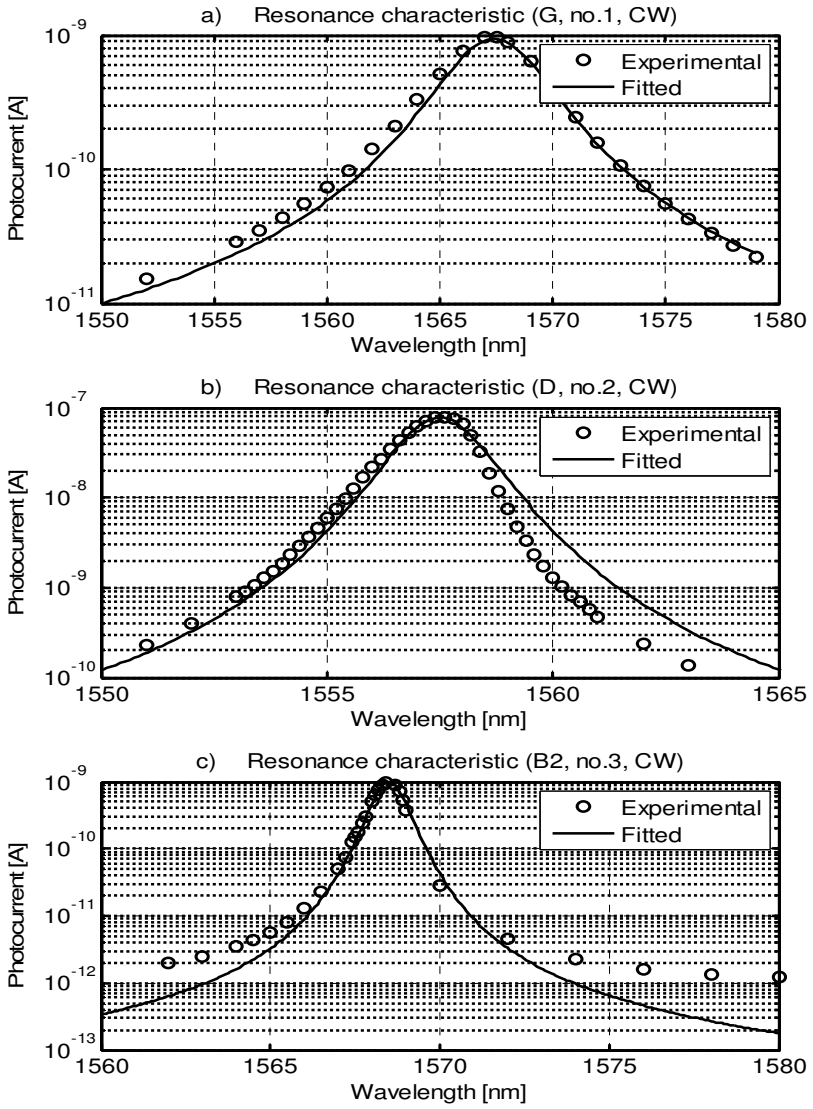

Figure 3-12 Resonance characteristics of the three device structures, points – experimental results, solid lines – plots of equation (3-16) for fitted cavities field transfer functions H(f)

From the experimental results the devices bandwidths were evaluated at normal incident angle as 5 nm for structure no.1, 1.8 nm for structure no.2 and 1 nm for structure no.3. The resonance wavelengths at normal incidence were found as 1567.4 nm, 1557.5 nm and 1568.5 nm respectively.

3.5.3. Resonance Wavelength Tuning

In the previous section a TPA microcavity photodetector resonance characteristic was discussed for normal incident angle. It was mentioned before that the device resonance wavelength can be tuned by varying the incident signal angle. The device resonance characteristic depends on the cavity length, active region absorption and both mirrors reflectivities. All these parameters change when the cavity is tilted (see Figure 3-13). Quantum efficiency of angled RCE photodetector can be analyzed [6] by replacing β with $\beta\cos(\theta)$, and $\psi_{1,2}$ with adequate angle dependant functions $\psi_{1,2}(\theta)$ in equation (3-10). Here θ is, by Snell's law, $n\sin\theta=\sin\theta_I$, where θ_I is the incident angle and n the refractive index of the cavity material.

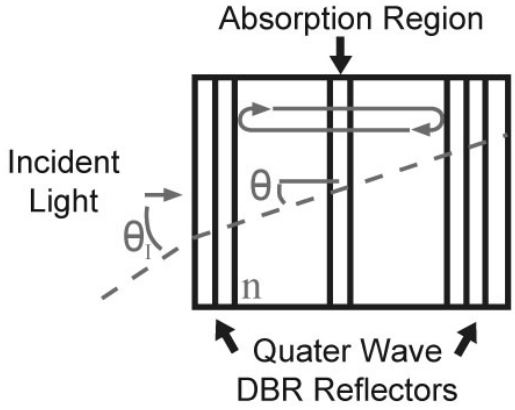

Figure 3-13 Cavity wavelength tuning by varying an incident angle

A theoretical investigation into TPA microcavity angle tuning was carried out in [12] showing that resonance wavelength shift, from the normal incident resonance wavelength, is proportional to the sine square of the incident angle.

$$\lambda_{res} = \lambda_{res}^{norm} - \frac{D^{\theta}\lambda_{res}^{norm}}{2D^{\lambda}}\sin^2(\theta) \tag{3-22}$$

where $D^{\theta/\lambda}$ are constants in units of length determined by the device structure.

To verify this wavelength tuning ability, a sample with structure no.1 was mounted on a rotating stage allowing for accurate angle device positioning. Both the device and the coupling lens were aligned precisely so the coupled light focused exactly in the active region of the device for any rotation angle. This ensured the device was always accurately aligned removing the necessity of the device realignment at each angle step. The resonance characteristic was carried out with incident CW source using the same setup as in Figure 3-11. The experimental results for varied incident angles are shown in Figure 3-14. From the results it can be seen that cavity tilt resulted in the resonance wavelength shift but also cavity bandwidth change. This was expected since the single round-trip loss increases with the incident angle due to the longer interaction length of the light with

the active region. Consequently the cavity finesse decreases for angled device resulting in broadened device bandwidth. The device wavelength tuning range is characterized in Figure 3-15 where resonance wavelength is plotted versus the incident angle. From the results it can be seen that the device resonance wavelength can be tuned over 60 nm by rotating the device by 60°.

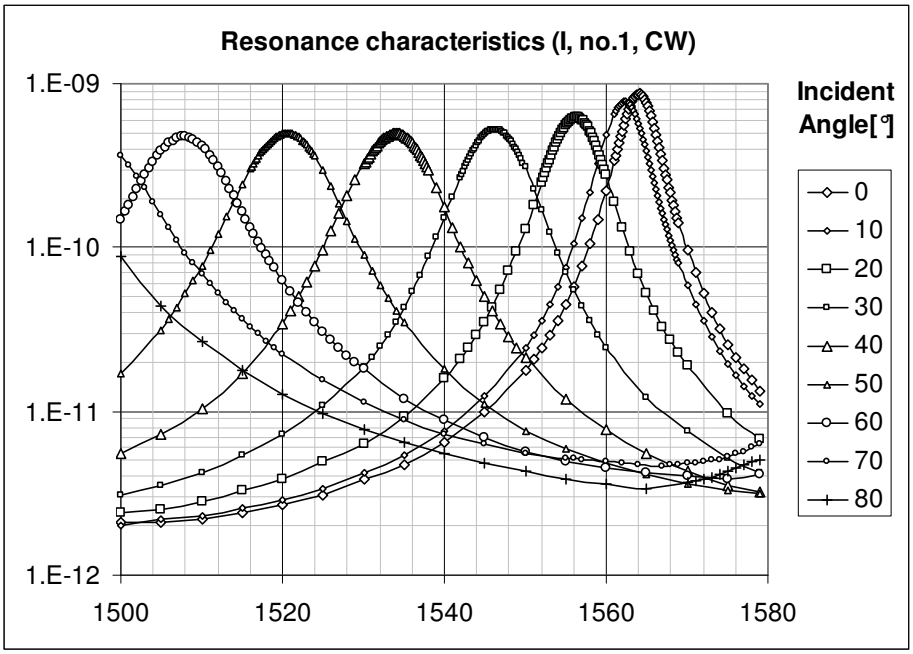

Figure 3-14 Resonance characteristics for varied incident angle

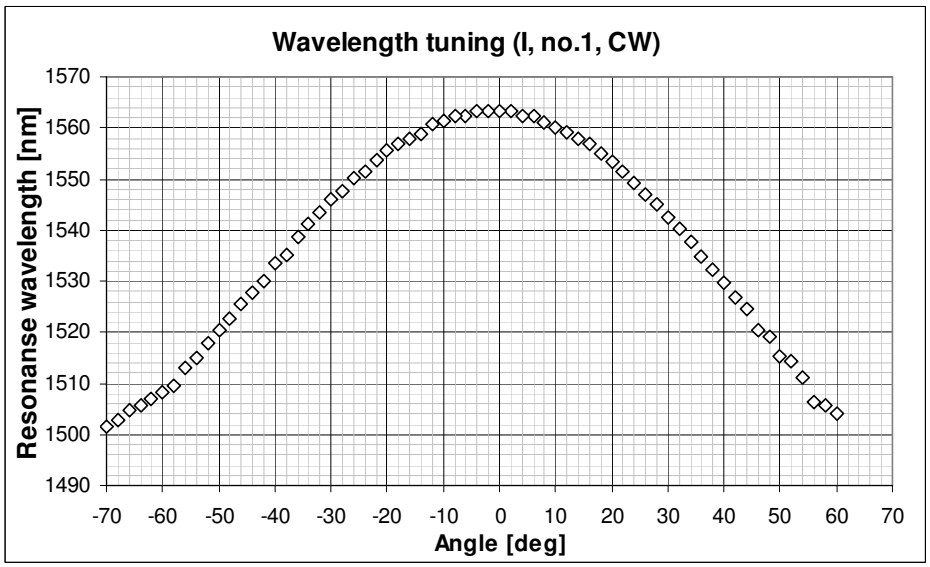

Figure 3-15 TPA microcavity resonance tuning by varying the incident angle

As was expected the measured resonance wavelength shifts is proportionally to the sine squared of the incident angle according to the equation (3.22). Nearly linear resonance wavelength shift of 1.32 nm/1° was measured between 15° and 60° incident angles.

3.5.4. Device Bandwidth

In previous sections the RCE device resonance characteristic was discussed showing its potential for use in multi-wavelength systems. It was described how the optical field within a cavity builds up gradually due to successive reflections of the light coupled into the cavity. Thus the incident optical pulse is modified in the cavity, which may be described with the cavity impulse response h(t). The build up time is measured with the cavity lifetime τ_{cavity} defined as rms width of the cavity impulse response h(t). If an optical pulse with temporal width τ_{pulse} is coupled into the cavity with lifetime τ_{cavity}, the actual pulse width within the cavity can be written as:

$$\tau_{actual} = \sqrt{\tau_{pulse}^2 + \tau_{cavity}^2} \tag{3-23}$$

The Optical field within the cavity interacts with the active region to generate carriers. This results in a delayed device response due to the time required by photo-carriers to travel across the depletion region. The RCE structure allows for significant reduction of the active region thickness and the drift time, however it still remains the main device speed limiting factor. The device response delay due to the electric carriers-drift can be described, similarly to the cavity effect, using an impulse response description. Let us define the impulse response function $h_{electrical}(t)$ associated with the carriers-drift time. The average time required for electric carriers to travel from the depletion region $\tau_{electrical}$ would be then rms width of $h_e(t)$. When electric pulse emerges from the device, it will have broadened into:

$$\tau_{output} = \sqrt{\tau_{pulse}^2 + \tau_{cavity}^2 + \tau_{electrical}^2} \tag{3-24}$$

An aggregated device impulse response is given by:

$$h_{device}(t) = h_{cavity}(t) * h_{electrical}(t) \leftrightarrow H_{device}(f) = H_{cavity}(f) \cdot H_{electrical}(f) \tag{3-25}$$

where h_{device} is the device impulse response given by a convolution of the RCE cavity impulse response h_{cavity} and electrical impulse response $h_{electrical}$, or in equivalently in a frequency domain H_{device} is the device frequency response given by the product of the RCE cavity frequency response H_{cavity} and the electrical frequency response $H_{electrical}$. In practice the device response time is mainly limited by the electric carrier diffusion, thus the RCE cavity effect is often neglected in discussion of the device speed. Thus the device electrical bandwidth is commonly defined as a FWHM of $|H_{device}|^2 \approx |H_{electrical}|^2$.

The impulse response of device with structure no.3 was measured using the experimental setup shown in Figure 3-16. An ultra short-pulse laser source was utilized to generate high peak-power optical pulses of 700 fs duration and 10 MHz repetition rates. Pulses were coupled into the device through a polarization controller (PC). The device was angled by 27° to shift its resonance wavelength and match the 1558nm wavelength of the pulse source. A bias tee was used to cut off a

DC component from the detection arm (SCOPE), and RF component from a DC bias arm. A high-speed electrical amplifier (AMP) was placed before the oscilloscope to boost the RF signal before detection. The RF signal measured on the oscilloscope corresponds to the device impulse response. An additional 2kΩ resistor was placed in series with the tested device to increase the aggregated impedance. Initially the resistance used was 50Ω which corresponds to the input impedance of the electrical amplifier however the signal measured on the oscilloscope was very weak and difficult to analyze. The 2kΩ resistor increased the overall voltage across the sample and the resistor and thus improved the signal amplitude on the scope. This however resulted in imperfect impedance matching between the device and the detection system. To obtain an optimal result a Trans-Impedance Amplifier (TIA) should be used. This prototype design, however, was sufficient to carry out satisfactory measurements.

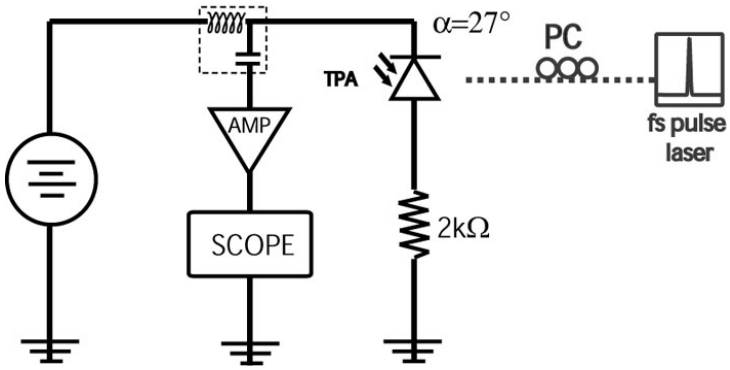

Figure 3-16 experimental setup to measure TPA microcavity device electrical bandwidth

The measured oscilloscope trace obtained using the above setup is shown in Figure 3-17.

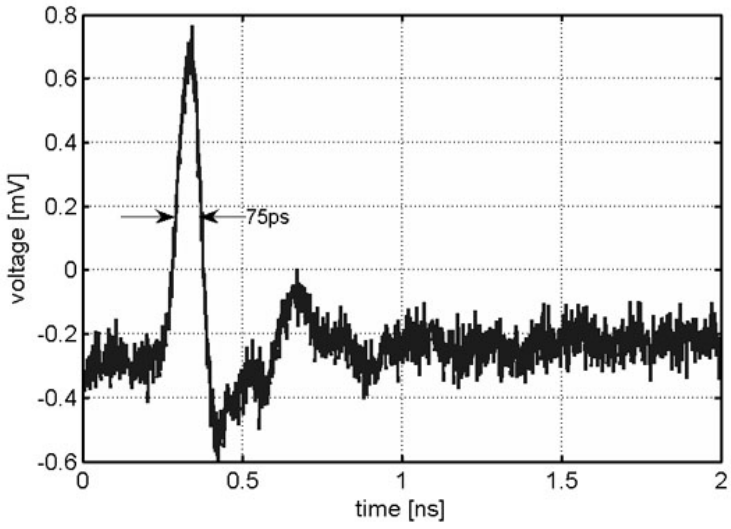

Figure 3-17 Device structure no.3 electrical impulse response

The measured on the scope device impulse response FWHM was τ_{output}=75ps. To evaluate device electrical bandwidth we approximated the impulse response to have a normalized Gaussian shape:

$$A(t) = \frac{1}{\sqrt{2\pi}\sigma} \exp\left(-\frac{t^2}{2\sigma^2} \right) \tag{3-26}$$

where σ is rms width of the Gaussian envelope. The relation between rms and FWHM width can be found σ=0.42·FWHM=32ps and the corresponding device electrical bandwidth:

$$BW = \frac{1}{2\pi\sigma} = 5GHz \tag{3-27}$$

In the above calculations the device electrical bandwidth was evaluated from the impulse response recorded on the scope. In fact the response time is a result of combined effects including limited cavity life time τ_{cavity}=8ps (optical bandwidth), oscilloscope response time τ_{scope}=7ps (oscilloscope bandwidth), signal temporal jitter τ_{jit} and others. These effects were neglected however, since these are an order of magnitude shorter then the dominant, electrical-carriers drift-time.

3.6. Summary

High speed optical signal processing requires novel techniques to overcome electronic speed processing limits. Particularly high speed temporal characterization is a crucial operation for future broadband optical communications. Optical nonlinearities can be used to carry out high speed signal processing entirely in the optical domain. Two-Photon Absorption (TPA) in a semiconductor medium is a potential candidate for all-optical signal processing.

In this Chapter fabricated TPA microcavities based on three different designs were characterized and tested for potential applications. The principles of the TPA process and the RCE technology were summarized. Initial characterization of samples from each design was carried out including PI-curve, resonance characteristic and electrical bandwidth. A simple technique to measure PI-curve above accessible power levels was presented. The device dynamic range was limited by SPA on the low power side and total absorption at the high powers. A simple way to estimate device response for any incident signal duty-cycle from the measured PI-curves was explained. The devices resonance characteristics were measured in agreement with the cavities designed lifetimes. The measured electrical bandwidth of the third structure (no.3) device was around few GHz range. It is expected to achieve further speed improvement by optimizing the device packaging. In addition the elaborated devices are intended to be integrated with Trans-Impedance Amplifier (TIA) to achieve optimal sensitivity and high-speed, impedance matched compact device.

The all-optical, nonlinear, temporal characterization techniques such as autocorrelation or sampling are based on average nonlinear response measurement. The signal characterization which is carried out in the optical domain is not limited by OE conversion as long as the measured parameters (such

as pulse width) are not changing on a timescale comparable with the device electrical bandwidth. For the RCE device the processing speed is however limited by the cavity lifetime, for example the 8 ps (no.2 structure) TPA devices can be used for characterization of signals up to approximately 125 GHz, while the 1 ps devices (no.1) are suitable for up to 1 Tb/s signals characterization. The fabricated devices were implemented for pulse broadening monitoring due to CD of a signal operating up to 160 Gb/s. The experimental results supported by a theoretical discussion are presented in the following chapter.

References

[1] M. Göppert-Mayer, “Über Elementarakte mit zwei Quantensprüngen,” *Annalen der Physik*, vol. 401, no.3, pp.273-294

[2] W.Kaiser, C.G.B. Garrett, “Two-Photon Excitation in $CaF_2:Eu^{2+}$,” *Physical Review Letters*, vol.7, no.6 pp. 229-231, 1961.

[3] P.A. Franken, AE. Hill, C.W. Peters, and G. Weinreich, "Generation of optical harmonics," *Physical Review Letters*, vo1.7, no.4, pp. 118-119, August 1961

[4] P.M.W. Skovgaard, R.J. Mullane, D.N. Nikogosyan, J.G. McInerney, "Two-photon photoconductivity in semiconductor waveguide autocorrelators," Optical Communications vol.153, pp.78-82

[5] Evgeni Sorokin, Gabriel Tempea, and Thomas Brabec, "Measurement of the root-mean-square width and the root-mean-square chirp in ultrafast optics," *Journal of Optical Society of America B*, vol.17, no. 1, 2000

[6] K Kishino, M. S. Unlii, J-I. Chyi, J. Reed, L. Arsenault, H. Morkoq, "Resonant Cavity - Enhanced (RCE) Photodetectors," *IEEE Journal of Quantum Electronics*, vol.27, no.8, 1991

[7] J.A. Jervase, Y. Zebda, "Characteristic analysis of resonant-cavity-enhanced (RCE) photodetectors," *IEEE Journal of Quantum Electronics*, vol. 34, no.7, 1998

[8] H. Folliot, M. Lynch, A. L. Bradley, T. Krug, L. A. Dunbar, J. Hegarty, and J. F. Donegan, L. P. Barry, "Two-photon-induced photoconductivity enhancement in semiconductor microcavities: a theoretical investigation," *Journal of Optical Society of America B*, vol.19, no.10, pp.2396-2402, 2002

[9] M. S. Unlu, “Resonant cavity enhanced photonic devices,” *Journal of Applied Physics* vol.78 no.2 pp.607-639,1995

[10] M. Sheik-Bahae, D. C. Hutchings, D. J. Hagan, E. Van Stryland, "Dispersion of bound electronic nonlinear refraction in solids," IEEE J. Quantum Electron. no.27, pp. 1296–1309, 1991

[11] W.H.Guo, J.O’Dowd, M.Lynch, A.L.Bradley, J.F.Donegan, L.P.Barry, “Influence of Cavity Lifetime on High-Finesse Microcavity Two-Photon Absorption Photodetectors, *IEEE Photonincs Technology Letters*, vol.19, no. 6, March 15, 2007

[12] T. Krug, W. H. Guo, J. O'Dowd, M. Lynch, A. L. Bradley, J. F. Donegan, P. J. Maguire, L. P. Barry, H. Folliot, “Resonance Tuning of Two-Photon Absorption Microcavities for Wavelength-Selective Pulse Monitoring,” *IEEE Photonics Technology Letters,* vol.18, no.2, pp.433-435, Jan. 2006.

CHAPTER 4. Chromatic Dispersion Monitoring using TPA Microcavity

4.1. Introduction

Chromatic Dispersion (CD) or Group Velocity Dispersion (GVD) is a variation in the velocity of light according to wavelength, resulting in temporal pulse broadening in optical fibers. The principles of CD in Single Mode Fiber (SMF) were given in section 1.4.1. The first order GVD β_2 wavelength dependence is related to dispersion D by equation (1-8). In high-speed communication systems, CD becomes a major limiting factor. Although CD results in signals distortion during propagation, certain amount of dispersion in the transmission line is desired in order to minimize nonlinear signal degradation. For example SPM or FWM channel cross-talk in multi-wavelength systems (see section 1.4.1) are significantly suppressed by the phase mismatch between the signal spectral components imposed by GVD. Consequently telecommunication fibers usually are designed to have a small amount of dispersion i.e. D=16ps/km.nm for conventional SMF. The dispersion imposed distance limit can be overcome by implementing a dispersion management scheme [1][2]. This technique includes in a transmission path a fixed-value, negative-dispersion element that compensates for a positive dispersion encountered by the signal. Effective net accumulated dispersion encountered by the signal in the whole link is approximately equal to zero. The dispersion management scheme is widely used in deployed long-haul telecommunication systems however it does not accommodate for additional dispersion fluctuations resulting from varied environmental (temperature and vibration) conditions or additional phase shift imposed by nonlinear effects. CD is a critical issue because system tolerance for additional CD fluctuations rapidly decreases as data rate increases, and it is difficult to mitigate against [3]. The CD characteristics of a fiber may depend on its date of manufacture and type of installation (aerial versus underground). For example underground optical transmission cables are typically buried at a depth of 0.6–1.2 m, therefore daily temperature variations which reach depths up to 0.45 m, can be neglected. Seasonal temperature variations, however, can reach a depth of several meters resulting in degradation of the system performance.

CD temperature dependence was characterized for typical optical fibers in [4]. The dispersion change due to temperature drift coefficient for NZ-DSF was measured to be -0.0025 ps/km.nm.C° or for DCF to be +0.0009 ps/km.nm.C°. Transmission lines, that utilize dispersion management scheme consisting of opposite dispersion sign optical fibers, commonly exhibit low aggregated coefficients typically less than -0.001 ps/km.nm.C° due to a self compensation effect. The time scale of environmental-imposed fluctuation is relatively low however in mesh-topology networks,

where different optical paths are exposed into different environmental conditions, the dispersion mismatch can change very quickly whenever signal is switched into a different path. Variations in dispersion can be reduced either by replacing the optical fiber infrastructure or by utilizing tunable CD compensation within existing systems. According to [5], operators are considering using the second approach near term, rather than phasing over to next-generation fiber. Having spent significant investments installing new fiber (1995-2000), most long-haul service providers are not eager for another major fiber-deployment cycle near term. Consequently tunable CD compensating modules are predicted to dramatically increase in market share in the nearest future. An important parameter of any tunable CD compensator will be CD monitoring element.

In this chapter a CD monitoring technique based on a TPA microcavity device will be discussed theoretically and experimentally. In Sections 4.2 and 4.3 an introduction into the theoretical model will be given including basic equations and notation used. In Section 4.4 a TPA microcavity device response for a modeled dispersed pulse sequence will be calculated to investigate resonance cavity influence on the nonlinear detection. The monitored pulse shape influence will be discussed in Section 4.5. Finally the theoretical model will be applied to discuss experimental results presented in sections 4.6 and 4.7. In section 4.6 CD monitoring of 160 Gb/s signal will be shown and in section 4.7 device performance in a multi-wavelength system will be investigated. In particular additional channel cross-interference and TPA microcavity wavelength tuning will be investigated. In section 4.8 a theoretical discussion into ideally matched device to monitor a realistic system will be given. The last section 4.9 will present experimental results for more advanced system monitoring technique utilizing TPA device for all-optical sampling.

4.2. CD Modeling

Pulse propagation in optical fiber can be modelled using the Nonlinear Schrödinger Equation (1-5). CD effects can be investigated separately by neglecting nonlinear effects (γ=0) resulting in a Linear Schrödinger Equation:

$$i\frac{\partial A}{\partial z} = \frac{1}{2}\beta_2 \frac{\partial^2 A}{\partial t^2} \tag{4-1}$$

where β_2 is the first order GVD parameter and A(z,t) is the incident signal (complex) amplitude envelope:

$$A(z,t) = \left|A(z,t)\right| \exp\left(i\phi(t)\right) \tag{4-2}$$

where z denotes the position along the fiber and Φ(t) is the absolute optical phase. To investigate propagation of a Return to Zero (RZ) pulse sequence, the pulse power envelope is commonly

approximated using Gaussian or sech^2 profiles. Fourier Transform-Limited (FTL) pulse amplitudes can be written for Gaussian and sech^2 shapes respectively:

$$A(z=0,t)_{Gaussian} = \exp\left(-\frac{t^2}{2\tau_0^2}\right) \tag{4-3}$$

$$A(z=0,t)_{\sec h2} = \sec h\left(\frac{t}{\tau_0}\right) = \frac{2}{\exp\left(\frac{t}{\tau_0}\right)+\exp\left(-\frac{t}{\tau_0}\right)} \tag{4-4}$$

were t is the time, τ_0 is the pulse width parameter and the position z along the fiber is set to zero. Note that optical phase is uniform $\Phi(t)=0$ across the amplitude which is characteristic for FTL pulses. Temporal dependence of the amplitude can be decomposed into a series of frequency components through the Fourier transform, to obtain equivalent frequency representation of the signal:

$$\tilde{A}(z,\omega) = \frac{1}{2\pi}\int_{-\infty}^{\infty} A(z,t)\exp(i\omega t)dt \tag{4-5}$$

where ω is the angular frequency. Commonly absolute amplitude squared in the time or frequency domain is plotted (referred to as optical power). Example plots of temporal and frequency power envelopes for Gaussian and sech^2 pulses are depicted in Figure 4-1.

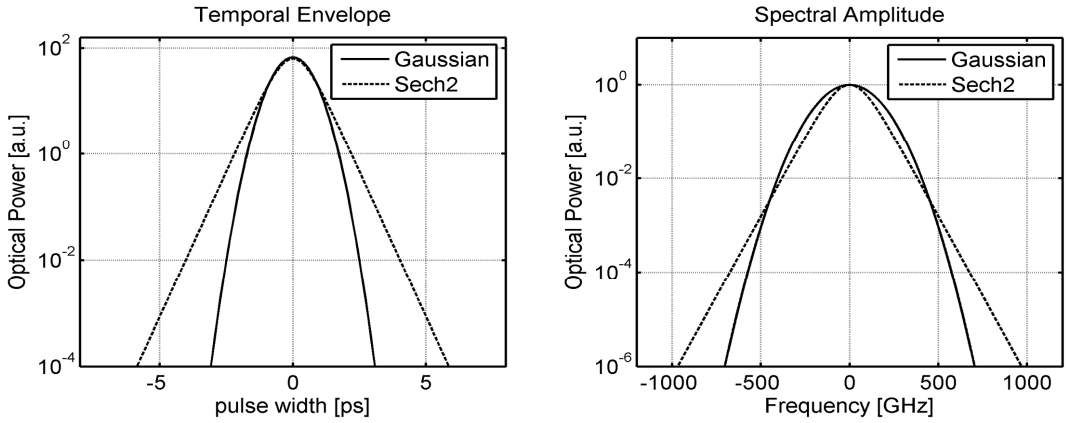

Figure 4-1 temporal a) and frequency b) representations of Gaussian and sech^2 pulses

There are two common conventions used to measure pulse duration and frequency width. This can be explained using the example of a Gaussian pulse given by Fourier-transform pair:

$$A(t) = \exp\left(-\frac{t^2}{2\tau_0^2}\right) \leftrightarrow A(\omega) = \tau_0 \exp\left(-\frac{\omega^2}{2\Delta\omega^2}\right) \tag{4-6}$$

where $\Delta\omega=1/\tau_0$ is the width parameter of the frequency power envelope. It can be seen that for a Gaussian pulse its frequency representation has also Gaussian shape. The pulse duration τ_0 and the frequency width $\Delta\omega$ are commonly used in theoretical calculations. The frequency width is often

referred to as an optical signal bandwidth. It can be seen that the time bandwidth product is constant, and equals to unity ($\tau_0 \cdot \Delta\omega = 1$) for the above notation. Note that for a Gaussian pulse τ_0 and $\Delta\omega$ are rms widths (see equation (3-6)) of the temporal and spectral power envelopes respectively. The above relation for the time-bandwidth product between rms duration and bandwidth can be expanded among any pulse shape. The above notation for pulse duration and bandwidth benefits from a significant calculation simplification in the theoretical discussion. However in experimental work the rms pulse width and bandwidth are difficult to handle therefore pulse duration is commonly defined as a FWHM of the temporal power envelope and the bandwidth as a frequency width at 3dB point (frequency equivalent of FWHM). Furthermore in experimental work frequency defined as $f=\omega/2\pi$ is used rather then angular frequency ω. These parameters are easily measurable using laboratory instrumentation. Example relations between the pulse width parameters τ and the corresponding FWHM of the pulse power envelopes for Gaussian and sech^2 pulses are respectively:

$$FWHM_G = 2\sqrt{\ln 2} \cdot \tau_0 = 1.665 \cdot \tau_0 \quad ; \quad FWHM_S = \ln(3+\sqrt{2}) \cdot \tau_0 = 1.7627 \cdot \tau_0 \qquad (4\text{-}7)$$

Similarly in the frequency domain:

$$\Delta f_G = 1.665 \cdot \frac{\Delta\omega}{2\pi} \quad ; \quad \Delta f_S = 1.7627 \cdot \frac{\Delta\omega}{2\pi} \qquad (4\text{-}8)$$

where G and S refers to Gaussian and sech^2 pulses respectively. Simple calculations show that the time-bandwidth product defined as $FWHM_x \cdot \Delta f_x$ (x=S,G) is 0.44 for Gaussian shape and 0.315 for Sech^2 shape. In this work the second convention will be used for pulse duration and bandwidth unless it is specified otherwise.

Note that time-bandwidth products in both conventions reach a minimum value for FTL pulses having fixed phase among all spectral components. However if the relative phase varies across the pulse, certain frequency components are shifted ahead of the pulse while others lag behind. This results in a temporal pulse broadening and shape change according to the phase distribution. Consequently non-FTL pulses have the time bandwidth product always greater then the FTL minimum value. The phase variation across the pulse can be described by adding $\exp(i\Phi(t))$ component in the equations (4-3) and (4-4).

Phase across an initially transform limited pulse is modulated due to CD while propagating through an optical fiber. Consequently the amplitude across the dispersed pulse becomes a complex value. Since the amplitude can not be measured directly an optical power is commonly plotted, either in a temporal or frequency domain. This however does not contain the phase information, therefore an additional phase distribution plot is required for a complete pulse description. Commonly the phase derivative in respect to time (chirp) or frequency (group delay) is plotted. This can be viewed in

Figure 4-2 where normalized power envelopes of 2 ps incident Gaussian pulse (dotted), and the same pulse after propagation through a 500m of conventional SMF (solid) are plotted. Chirp across the dispersed pulse is plotted on the right-hand side axis. The dispersed pulse power envelope was calculated utilizing the Schrödinger Equation (4-1), for which a general solution can be written as:

$$A(z,t) = \frac{1}{2\pi}\int_{-\infty}^{\infty} \tilde{A}(0,\omega)\exp\left(\frac{i\beta_2\omega^2 z}{2} - i\omega t\right)d\omega \tag{4-9}$$

By carrying out the integration assuming incident Gaussian pulse shape the amplitude at distance L can be written as:

$$A(L,t) = \left(1+\frac{i\beta_2 L}{\tau_0^2}\right)^{-1/2}\exp\left(-\frac{t^2}{2(\tau_0^2 - i\beta_2 L)}\right) \tag{4-10}$$

By substituting L=500 m the dispersed pulse power envelope was calculated for the incident τ_0=2 ps pulse. It can be seen from equation (4-9) that CD varies the phase of the transmitted signal proportionally to the square of the angular frequency ω^2. This results in a linear chirp ($d\Phi(t)/dt$) or linear group delay ($d\Phi(\omega)/d\omega$), and as a consequence temporal pulse broadening. It can be also shown by calculating an absolute amplitude |A(L,t)| from equation (4-10), that a Gaussian pulse has a unique property that it maintains its Gaussian shape during propagation.

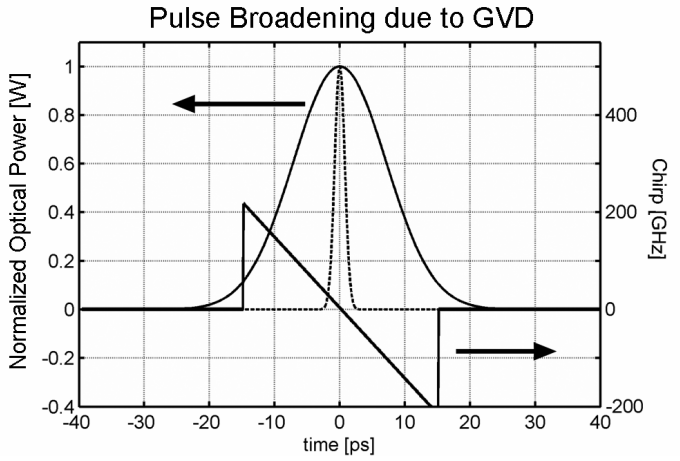

Figure 4-2 Transform-limited 2ps pulse intensity profile (doted), dispersed pulse (solid), chirp profile (solid)

Pulse broadening due to CD can be easily calculated according to the relation:

$$\tau = \sqrt{\tau_0^2 + (D\cdot L\cdot \Delta\lambda)^2} \tag{4-11}$$

where τ_0 and τ are the incident and the broadened pulse rms widths, D is the fiber dispersion, L is propagated distance and $\Delta\lambda$ is the incident signal spectral width given by:

$$\Delta\lambda = \frac{c\Delta f}{f_c^2} = \frac{2\pi c\Delta\omega}{\omega_c^2} \tag{4-12}$$

were Δf and $\Delta\omega$ are the signal frequency and angular frequency envelop rms widths, and f_c and ω_c are the signal central frequency and central angular frequency respectively. From the equation (4-11) it is clear that wider bandwidth signals suffer more from CD, thus narrow-bandwidth modulation formats are desired. Higher bit rates however require shorter pulses which occupy a wider spectral bandwidth. For example RZ modulation commonly requires optical pulses not exceeding 1/3 of the single bit slot duration. Thus approximately τ_0=33 ps pulses are required for 10 Gb/s transmission which corresponds to $\Delta\lambda$=0.038 nm spectral bandwidth (provided Fourier Transform Limited). Such a pulse (at 1550 nm) can propagate through 154 km of conventional SMF (D=16 ps/km.nm) before the pulse broadens to the single bit slot duration. However for 40 Gb/s transmission (τ_0=8.3 ps, $\Delta\lambda$=0.15 nm), pulses will reach a single bit slot duration just after 9.6 km. It can be shown that the maximum transmission distance L_{MAX} decreases proportionally to the square of the transmission bit rate BR:

$$L_{MAX} \propto \frac{c}{D \cdot \lambda^2 \cdot BR^2} \tag{4-13}$$

This illustrates why CD becomes a critical factor limiting system performance when migrating towards higher bit rates. Residual CD fluctuations in high-speed system operating above 100 Gb/s can result in relatively high pulse degradation causing significant pulse overlapping and unacceptable inter-symbol interference. The pulse overlapping effects also limit the nonlinear dispersion monitoring range. This will be discussed in the following section.

4.3. Pulse Overlapping

In telecommunications systems pulses transmitted in an optical fiber broaden due to CD leading to the adjacent pulses overlapping. The overlapped pulses can interfere together resulting in a periodic incidence pulse reconstruction at the multiple of the incident repetition rate. This is known as a temporal Talbot or self-imaging effect [6][7] and can be used to generate pulse trains of ultrahigh repetition rates. The maximum repetition frequency that can be obtained is limited only by the temporal width of incidence pulses. This self-imaging is depicted in Figure 4-3. Temporal pulse evolution during propagation through a standard SMF with D=16ps/km.nm is shown in Figure 4-3 a). In the simulation a 10 ps (FWHM) Gaussian pulse train operating at 10 GHz repetition rate was modeled, with the initial pulse power envelope plotted in Figure 4-3 b). The neighboring pulse interference due to overlapping can be visible at 10 km distance and after approximately 20 km the initial pulse shape has reconstructed at multiplied 40 GHz rate. The temporal power envelope of the reconstructed pulses is plotted in Figure 4-3 c).

The Talbot effect has to be considered when modeling CD monitoring involving nonlinear detection. In communications RZ transmission commonly requires optical pulses with

approximately 33% duty cycle. The evolution of initial 10GHZ, 33 ps (FWHM) RZ pulse sequence due to CD is shown in Figure 4-4 a). Pulses broadened due to CD start to overlap coherently resulting in initial pulse sequence reconstruction after approximately 80km of propagation. This pulse reconstruction however requires high, sub-wavelength, phase stability across the successive pulses. This can occur in systems where optical pulses are carved from a CW source using an external modulator. In practice however, the pulse reconstruction is hardly observed especially when the pulse sequence was generated involving OTDM schemes. The effect is highly sensitive to additional random phase/amplitude change due to the modulation format used, or additional noise resulting from the transmission through the system. Consequently rather intensity pulse overlapping is observed than interference pulse reconstruction. This can be viewed in Figure 4-4 b) where overlapped pulses resemble wide bandwidth CW signal.

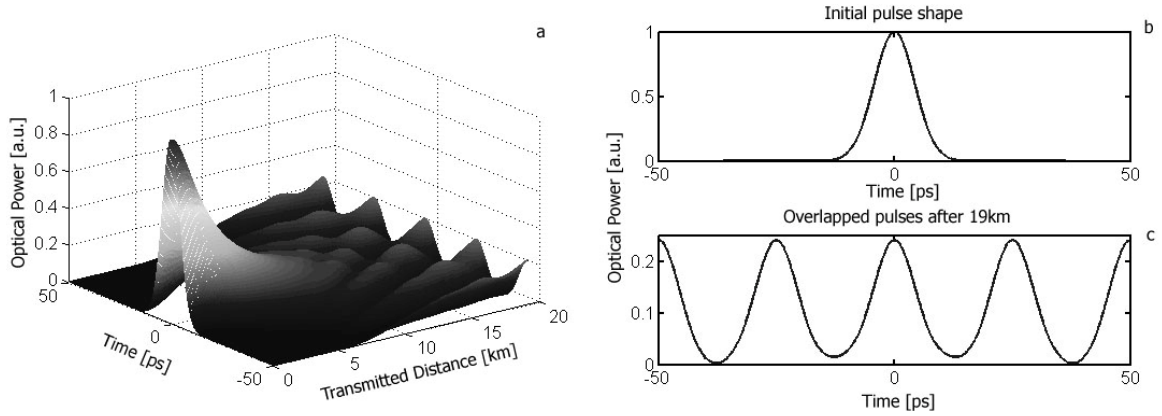

Figure 4-3 Talbot effect a) pulse evolution during propagation in SMF, b) initial pulse temporal profile, c) after propagation through 19km

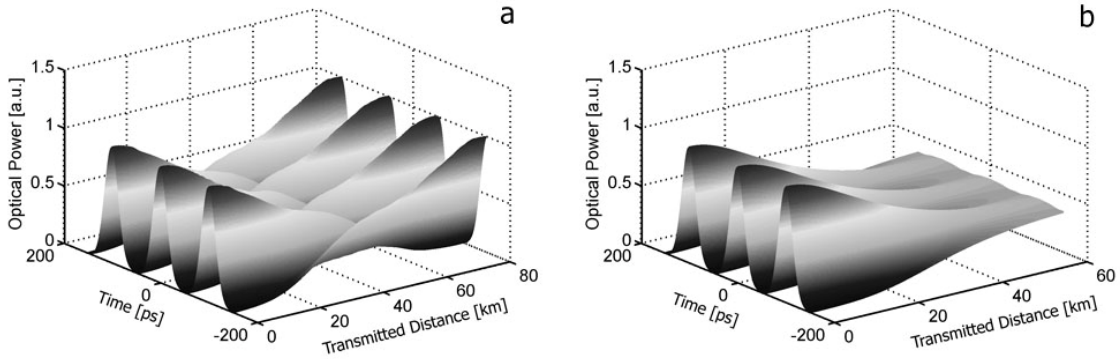

Figure 4-4 a) Self-imaging of 33% Duty cycle 10GHz pulse sequence after propagation through 80 km fiber, b) intensity pulse overlapping.

Both interference and intensity combining of the overlapped pulses limit the applicability of nonlinear techniques for CD monitoring. This overlapping threshold conventionally corresponds to the amount of dispersion where optical pulse width reaches the single bit slot duration. Since pulse reconstruction requires difficult to maintain conditions, in this work simple intensity overlapping will be assumed in the simulation model. For practical realizations, however, it is important to note that in a certain conditions the nonlinear response may start to increase above the overlapping threshold, due to reconstruction of the incidence pulses.

4.4. Cavity Influence on Chromatic Dispersion Monitoring

The applicability of nonlinear techniques for temporal pulse distortion monitoring was discussed in section 2.6.1. An inverse relation between the nonlinear response and the incident signal generalized duty cycle was shown. In chapter 3 the TPA nonlinearity in conjunction with RCE photodetector structure was discussed showing its potential for a high-speed, wavelength selective nonlinear photodetector design. Such a TPA microcavity can be used for high speed-signal processing. In this section TPA microcavity performance will be investigated in order to evaluate the cavity structure influence on the nonlinear detection and CD performance monitoring.

Consider a TPA microcavity photodetector with PI-curve and resonance characteristics as measured for sample with structure no.2 in sections 3.5.1 and 3.5.2. The cavity lifetime of 8ps and corresponding bandwidth of 135 GHz (1nm) is ideally suited for processing of signals from around 100 Gb/s repetition rate. Assume that 33% duty cycle, 100 GHz Gaussian pulse train after propagation through a varied length of optical fiber is coupled into the TPA microcavity. To analyze the cavity influence on the device performance the model shown in Figure 3-10 was used. The cavity influence on the incident dispersed pulse was calculated using the cavity field transfer function given by equation (3-15) with parameters R and FSR matched to mimic the experimental resonance characteristic shown in Figure 3-12 b). Next a nonlinear response was calculated for the obtained optical field within the cavity, and averaged over a single period. The calculation results are plotted versus incident accumulated dispersion and incident pulse width in Figure 4-5 a) and b), for the 135 GHz bandwidth device (dashed line). This is compared with no cavity (solid line) and 85 GHz (dotted line) bandwidth devices. The purpose of this simulation was to show the influence of the cavity structure on the nonlinear CD monitoring dynamic range, thus coupling efficiency effects were not included and the quantum efficiencies were simply normalized to one. For easier results comparison an average optical power within the cavity (after filtering) was normalized to unity for each modeled device.

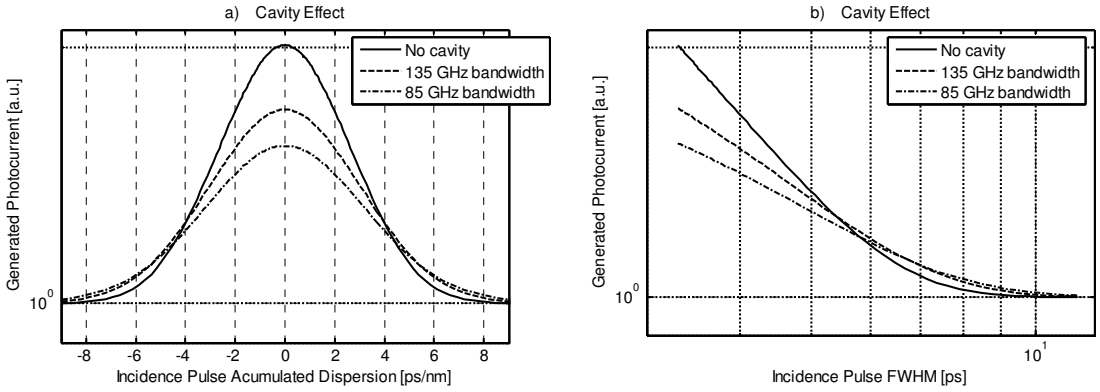

Figure 4-5 Nonlinear CD monitoring for various bandwidth microcavity devices

As was expected the maximum of the nonlinear response occurs for non-dispersed transform limited pulses. Introduced dispersion results in consecutive pulse broadening and leads to nonlinear response decrease. The nonlinear response reaches its minimum value, proportional to the square of the cavity average power, when pulses overlap completely. The non-cavity device represented by the solid lines in both figures was simulated by setting average mirrors reflectivity R to zero. The nonlinear response in this case according to the equation (2-13) is the inverse function of the incident generalized duty cycle and for Gaussian pulses is simply inversely proportional to the incident pulse width as long as pulses do not overlap. However when the cavity influence is included in the calculations it results in the increased dispersion monitoring range and reduced nonlinear response around the low dispersion range. This can be easily explained by considering the TPA microcavity as an optical filter followed by a nonlinear detector. Temporarily short but spectrally wide incident non-dispersed optical pulses are filtered out by the cavity field transfer function. Effectively pulses within the cavity (after filtering) are wider then the incident pulses, thus the nonlinear response is lower comparing to the non-cavity device. On the other side when a significantly dispersed pulse is coupled into the cavity the side spectral components, responsible for the majority of temporal broadening, are filtered out. Consequently the filtering of the incident signal results in partial cancellation of the dispersion effect, and the pulses within the cavity are narrower then the incident dispersed pulses. Thus the nonlinear response for widely dispersed pulses is higher compare to the non-cavity device.

The overall cavity influence results in a decreased contrast of the monitoring characteristic and the increased monitoring range. In practice it is reasonable to use a microcavity device with narrow optical bandwidth however not significantly narrower then the incident signal bandwidth. Narrow bandwidth device is desired due to high quantum efficiency and high wavelength selectivity

property, however extremely narrow bandwidth device will filter out most of the incident signal resulting in a significant reduction of the generated TPA response.

4.5. Pulse Shape Influence on Chromatic Dispersion Monitoring

In section 2.6.1 the principles of time domain measurements using nonlinear detection were given. It was shown that average nonlinear detection is sensitive to the incident signal shape and can be used for the signal monitoring. In particular optical pulse broadening due to Chromatic Dispersion (CD) can be measured involving nonlinear detection. According to equation (2-13) the average nonlinear response is inversely proportional to the incident signal generalized duty cycle. If the incident shape is known the pulse broadening due to CD can be modeled, and the corresponding nonlinear response. In a previous section 4.4, a Gaussian pulse evolution and nonlinear response was discussed. Although Gaussian pulses are commonly used due to mathematical simplicity, the Gaussian approximation may lead to certain inaccuracy between experimental and theoretical results. Usually pulses generated using mode-locking techniques, are best described with $sech^2$ shape. The pulse shape has an influence on the pulse CD broadening, and the way how the signal interacts with the microcavity structure.

To investigate the overall pulse shape influence on the nonlinear CD monitoring using TPA microcavity, numerical calculations were carried out for Gaussian and $sech^2$ pulses. The initial FTL 3.3 ps (FWHM), 100 GHz repetition rate Gaussian and $sech^2$ pulse sequences were modeled. Figure 4-6 a) plots the incident pulses temporal profiles over a single bit slot. Corresponding bandwidths (at 3dB level) are 133GHz for Gaussian and 100GHz for $sech^2$ shapes respectively. A TPA RCE photodetector was modeled to have a cavity field transfer function $|H(f)|$ resulting in the device bandwidth of 124 GHz (the device bandwidth was chosen to match approximately both simulated signals bandwidths). Here according to the previous discussion nonlinear photodetector bandwidth is defined as 3dB frequency width of the cavity field transfer function to the power of four $|H(f)|^4$. Figure 4-6 b) plots the incident pulse spectral profiles and the modeled cavity power-transfer function $|H(f)|^2$.

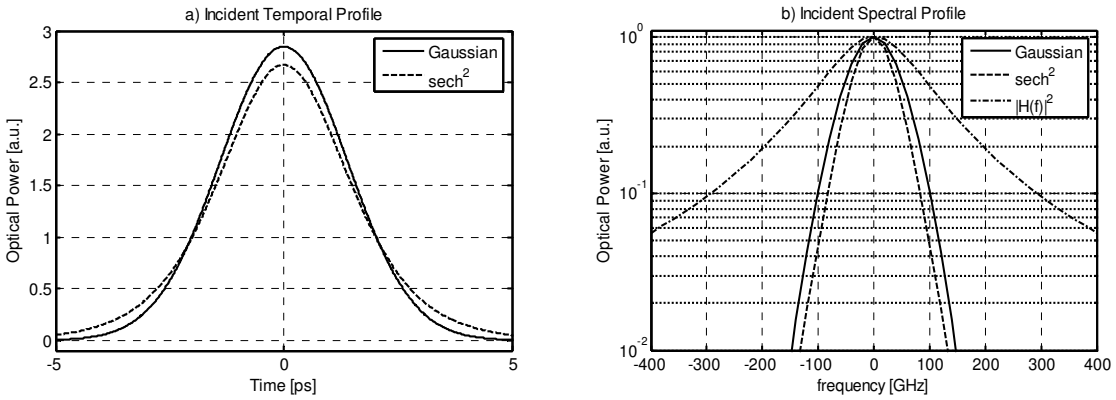

Figure 4-6 Incident Gaussian and sech^2 pulses: a) temporal profiles, b) spectral profiles and cavity power transfer function $|H(f)|^2$

Signal broadening due to CD and the corresponding nonlinear response versus experienced accumulated dispersion was calculated with the results plotted in Figure 4-7. A Gaussian pulse which has higher initial FTL peak power generates slightly higher nonlinear response around zero dispersion range. The nonlinear response decreases gradually due to experienced CD in both positive and negative directions. Both characteristics flatten eventually at levels proportional to the square of the cavity optical powers. Note that the Gaussian pulse which is slightly wider spectrally experiences more filtering due to the cavity. Thus optical power coupled into the cavity is lower for the Gaussian pulse compare to the sech^2, resulting in different flattening levels. The results illustrate how optical pulse shapes influences nonlinear dispersion monitoring characteristic. The nonlinear techniques can be used to measure the experienced accumulated dispersion accurately only if the pulse shape is known. However since the nonlinear response always increases with reduced dispersion and reaches its maximum for the fully compensated FTL pulse the dispersion compensation can be carried out regardless the shape (for RZ modulation format). A dispersion compensation module can be driven by a nonlinear detector to accommodate dynamically for varied amounts of dispersion by maximizing a nonlinear response.

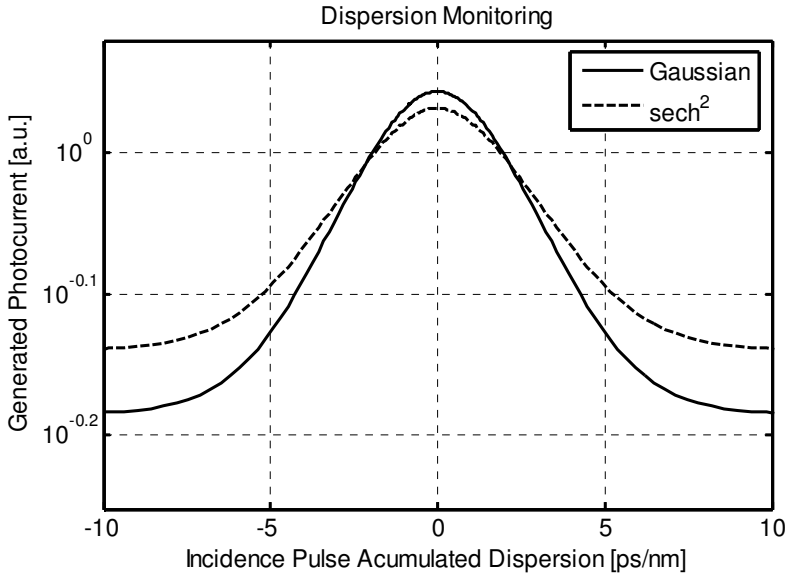

Figure 4-7 Dispersion monitoring for Gaussian and sech^2 pulse shapes

4.6. Chromatic Dispersion Monitoring Using TPA microcavity

Performance of the fabricated TPA microcavity devices was tested experimentally. In this section CD monitoring of a 160 Gb/s signal will be shown using a TPA microcavity A2, with a structure no.2. Since various samples may have slightly different characteristics the device was initially characterized before the actual measurements. The device resonance wavelength and bandwidth, at normal incidence, was 1556.5 nm and 220 GHz (1.8 nm). Such a device suits ideally for processing of signal bit rates in excess of 200 Gb/s, however here the device performance was tested with signals up to 160 Gb/s due to a laboratory equipment available. The experimental setup used is shown in Figure 4-8. Tunable Mode-Locked Laser (TMLL) driven with 10 GHz signal generator was used to obtain an initial sequence of 10 GHz RZ pulses. An optical isolator followed the laser source to remove back reflections from the setup. The pulses have 1.4 ps Fourier Transform-Limited (FTL) width of a sech^2 power envelope. Due to a negative, linear pre-chirp the generated pulses had approximately 2 ps duration at the laser output. The generated signal was first amplified using an EDFA and modulated using 10 Gb/s Mach Zehnder modulator (MOD). The modulator was driven with 2^7-1 Pseudo Random Bit Sequence (PRBS) driven by a Pulse Pattern Generator (PPG). A variable Optical Delay Line (ODL) was used to synchronize the optical pulse sequence with the modulation window and a Polarization Controller (PC) to optimize the incident polarization state before the modulation. Another EDFA and PC were used before an OTDM multiplexing stage (MUX) consisting of four independently switch-able stages with fixed delay lengths within each stage. Another EDFA was used to compensate for multiplexing loss and the signal was passed

through varied lengths of Dispersion Compensating Fiber (DCF) ranging from 0 to 80 m, to introduce varied amounts of CD. The fiber parameters measured at 1550 nm were dispersion D=-99.3 ps/km.nm, Dispersion Slope -0.21 ps/km.nm^2 and polarization mode dispersion PMD=0.18ps/√km. Resulting multiplexed and dispersed optical pulses were once again amplified using EDFA and coupled through a PC into the TPA microcavity (A2, no.2). Since various lengths of DCF resulted in different signal loss a variable attenuator (ATT) was placed before the last EDFA to ensure fixed (-7 dBm) incident optical power. This ensured the same Optical Signal-to-Noise Ratio (OSNR) of the signal after amplification. The optical signal (amplified to 9.2 dBm) was coupled into the device at normal incidence using a gradient index (GRIN) lens. The generated TPA photocurrent was measured using highly-sensitive amperometer (PAmmeter).

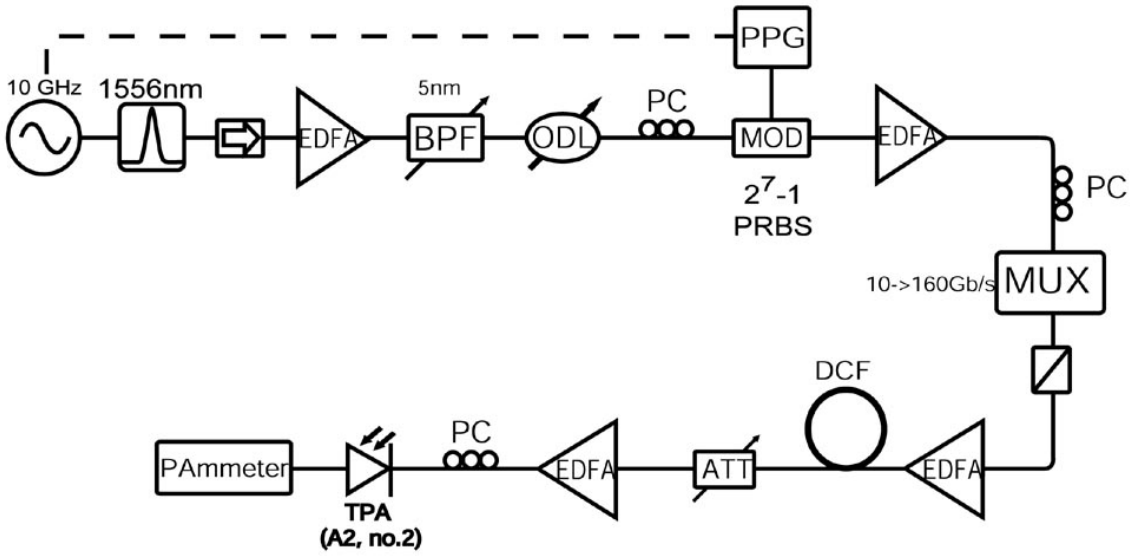

Figure 4-8 Experimental setup to verify TPA microcavity performance for CD monitoring

The DCF lengths were: 7 m, 14 m, 26 m and 40m. Each fiber sample was spliced with SMF connector to allow for easy plug in the setup. Due to different fiber core diameters, splicing between DCF and SMF, using conventional fusion splicer, resulted in significant splice loss (up to 3 dB). Consequently various DCF lengths (with 2 splices on each side) connected in different configurations resulted in significant variation of the optical loss between different configurations, in the worst case even -15 dB. This problem could be avoided by using a fiber splicer allowing for different fiber types splicing. At this stage however, simply an optical attenuator was placed in the setup to attenuate the signal to the same optical power level after each fiber configuration. This avoided additional signal OSNR variation resulting from amplification of significantly different power level signals.

Pulse widths corresponding to each fiber configuration were verified using SHG autocorrelation technique. The measured pulse widths were evaluated assuming $sech^2$ pulse profile. Table 4.1 summarizes the estimated pulse widths and the corresponding levels of accumulated dispersion experienced by the signal.

DCF length [m]	Autocorrelation trace width [ms]	Pulse width [ps]	Accumulated Dispersion [ps/nm]
0	0,4	2,0	-0,4
7	0,5	2,3	-0,7
14	0,7	3,3	-1,4
21	0,8	4,1	-2,1
26	1,0	4,7	-2,6
33	1,2	5,9	-3,3
40	1,3	6,6	-4,0
47	1,6	7,9	-4,7
54	1,8	8,7	-5,4
66	2,3	11,2	-6,6
80	2,9	14,3	-8,1

Table 4.1 Pulse widths and corresponding accumulated dispersion measured for various lengths of DSF using autocorrelation technique

Pulse width $\Delta\tau$ (FWHM) was evaluated according to the relation:

$$\Delta\tau = 0.648 \cdot v * ACT \tag{4-14}$$

where 0.648 is a factor associated with the $sech^2$ pulses, v=7.57 ps/ms is the autocorrelation conversion ratio depending on the scanning speed of the variable delay arm, and autocorrelation trace width is the measured on the scope trace width (FWHM) expressed in milliseconds.

Initially no DCF length was placed in the setup and all MUX stages were switched off to obtain 10 Gb/s, 2 ps pulse train incident onto the TPA microcavity. Successive MUX stages were next switched on to obtain 40 Gb/s, 80 Gb/s and 160 Gb/s signals. The polarization in each stage was set carefully to minimize power variations between different OTDM channels. This was very important since the nonlinear detection is highly sensitive to power variations. Next TPA photocurrents versus incident signal bit rate for fixed incidence optical power were recorded. This procedure was repeated for each DCF length configuration. The measured TPA photocurrent versus magnitude of the accumulated dispersion for each incident bit-rate is plotted in Figure 4-9 a).

Since the average power coupled into the device was fixed (9.2dBm), the incident peak powers are inversely proportional to the bit rate. The nonlinear photocurrent divides by two when the bit rate is doubled (twice more pulses x four times less nonlinear response). According to the expectations the nonlinear response decreases gradually due to the dispersion introduced. A flattening resulting from pulse overlapping can be seen for 160 Gb/s signal at the photo-current level proportional to the square of the incident average optical power (9.2dBm). The flattening occurs at different

accumulated dispersion levels for each data-rate, corresponding to the threshold level when pulses (within cavity) reach single bit slot duration. Above this level the nonlinear photocurrent remains constant.

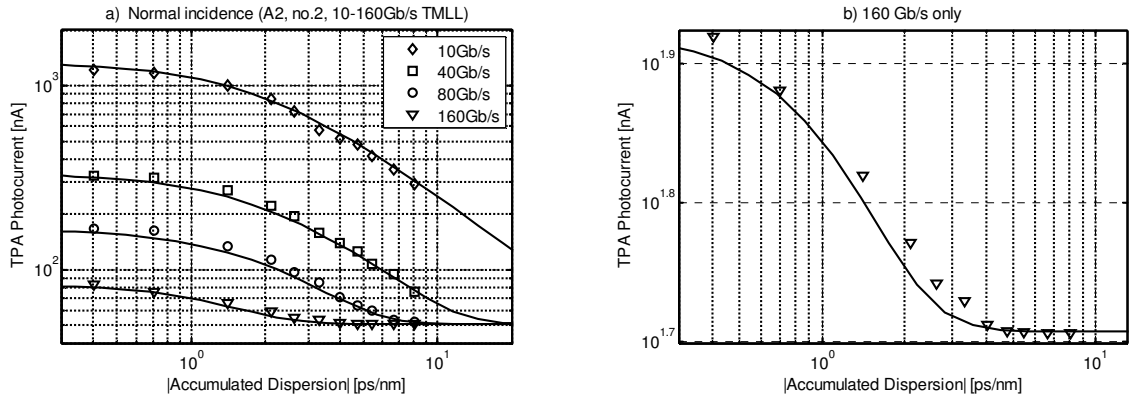

Figure 4-9 Experimental CD monitoring results for sample A2 operating at normal incidence angle for 10-160 Gb/s 2ps RZ PRBS (a), and for 160 Gb/s RZ PRBS only (b)

The experimental results are compared with a numerical simulation carried out utilizing the theoretical model described before assuming initial 1.4 sech^2 pulses and 220 GHz (1.8 nm) device bandwidth. An excellent agreement between the experimental results and the numerical simulation can be seen. The most important results for 160 Gb/s are enlarged in separate Figure 4-9 b). This reflects the most realistic scenario of 33% duty-cycle signal.

As was discussed in section 2.6.1 CD monitoring using nonlinear detection is inherently limited by pulse overlapping effect occurring when the pulse broadens to the single bit slot duration. The amount of temporal pulse broadening resulting from CD is proportional to the signal bandwidth (or transmission bit-rate). At the same time with the increased transmission rate the single bit slot duration reduces linearly. These two effects results in overall CD monitoring range to be inversely proportional to the square of the transmitted bit-rate. According to the equations (4-7), (4-8) and (4-11), for the case of sech2 pulse train operating at 160 Gb/s rate the amount of accumulated dispersion AD required to broaden the initial FTL 1.4 ps (FWHM) pulse to the single bit slot duration (in average 12.5ps due to modulation) is AD=D·L=±4,65 ps/nm. This limit is expected to increase to ±5 ps/nm due to the cavity filtering effect, resulting in partial cancellation of the CD pulse broadening (see section 4.4). This agrees with the experimentally measured accumulated dispersion monitoring range limit for 160 Gb/s data signal. It can also be seen that the limit increases linearly with reduced bit-rate (note that the signal bandwidth was the same for each bit rate). The results shown for 10-80 Gb/s signals, although operated at lower duty-cycles than commonly used in communications, are useful for understanding the device performance.

Certain inaccuracy between simulation and experimental results can be seen in the enlarged Figure 4-9 b. The measured nonlinear response at certain points exceeds the theoretical line due to power

fluctuations in the OTDM channels. The accurate equalization of the OTDM channels was difficult to perform for 160 Gb/s since all MUX stages had to be optimized separately. The nonlinear detection however always reaches its maximum response for fully compensated incident signal regardless of the power uniformity between OTDM channels.

4.7. TPA-Microcavity Wavelength Selectivity

In section 3.3 the advantage of Resonance Cavity Enhancement (RCE) for high speed detection was discussed. The RCE device benefits from the resonance characteristics producing high nonlinear response for the incident signal operating at the resonance wavelength, while significantly lower response for off-resonance signals. Furthermore the RCE microcavity resonance wavelength can be easily tuned by rotating the incidence angle. In this section wavelength-selective TPA microcavity performance will be investigated.

4.7.1. Off-Resonance Chromatic Dispersion Monitoring

In this section CD monitoring using TPA microcavity is performed for various incident signal wavelengths. The measurements were taken for a device E with structure no. 2, operating at normal incidence angle. The device initial characteristics are shown in Figure 4-10. The measured device resonance wavelength and bandwidth are 1561.8 nm and 275GHz (2.2 nm). PI-curve was characterized using 10 GHz, 2ps pulse source used later in the CD monitoring experiment. This allows for an easy comparison between experimentally measured TPA photocurrents and the PI-curve.

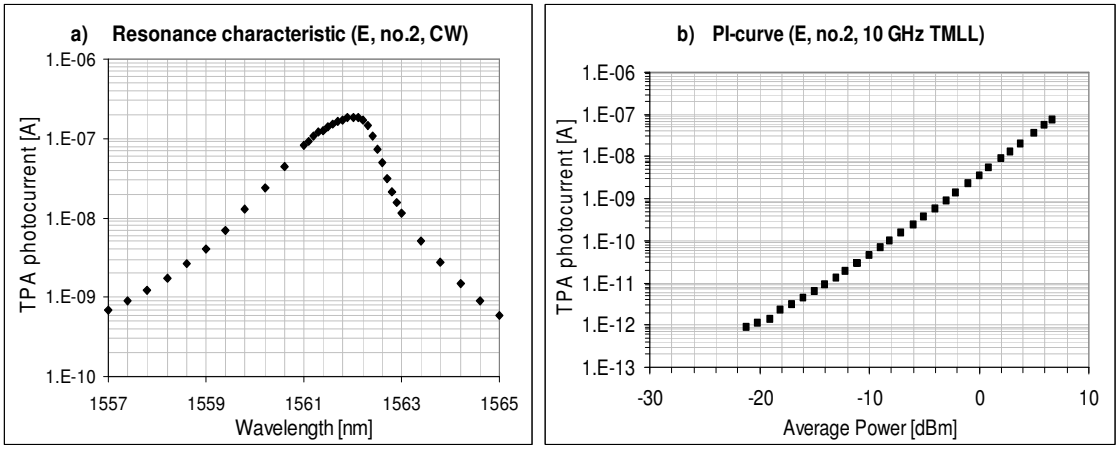

Figure 4-10 Initial characterizations of the TPA microcavity: a) resonance characteristic, b) PI-Curve obtained for 10 GHz, 2ps pulse source.

CD monitoring was carried out for an incident 40 Gb/s RZ Pseudo Random Beat Sequence (PRBS) using a setup shown in Figure 4-11. A similar configuration of 10 GHz TMLL source, modulator (MOD) and OTDM multiplexer (MUX) as in the previous section was used to generate the 40 Gb/s

signal here. Dispersion was introduced into the signal by passing it through various lengths and combinations of SMF, DSF and DCF. Since the exact lengths and parameters of the fibers were unknown, resulting pulse widths were monitored continuously using SHG autocorrelation technique assuming $sech^2$ pulse power envelope. Due to the high optical power required for the autocorrelation measurement 90% of the signal was split off using a passive optical coupler with the remaining 10% coupled into the TPA microcavity at normal incidence angle. The power level in the 10% arm was controlled using inline attenuator/power meter to ensure constant optical power incident onto the device. A polarization Controller (PC) was used to optimize the incident polarization state to achieve maximum TPA photocurrent. Since different lengths and kinds of fibers in various configurations resulted in a variation of the signal output power, the signal OSNR varied from one configuration to another, after the second EDFA. This caused an additional TPA photocurrent change due to response sensitivity to OSNR discussed in section 2.5.2. The generated TPA photocurrent versus incident pulse width was measured for the signal initially operating at 1561.9 nm corresponding to the cavity resonance wavelength. Next the signal was tuned off-resonance to 1560.1 nm and 1559.6 nm and the corresponding TPA versus pulse width characteristics were measured.

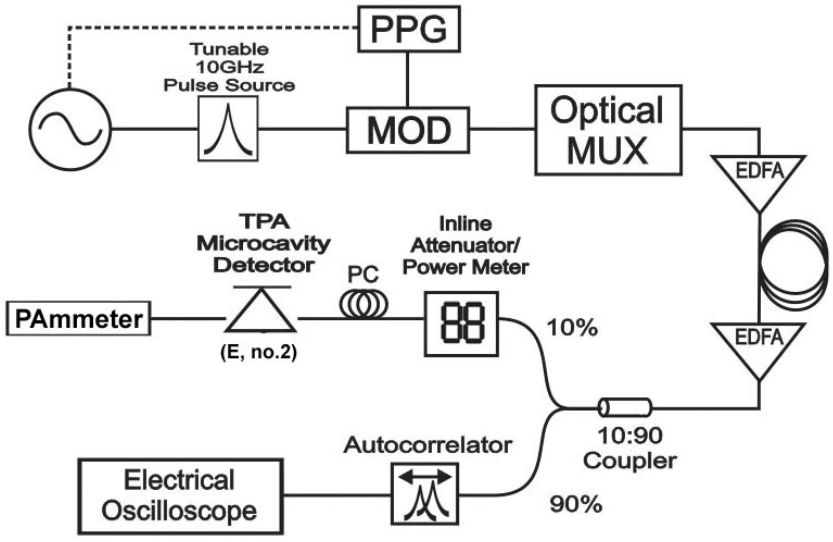

Figure 4-11 Experimental setup to investigate TPA microcavity wavelength selectivity

The experimental results are shown in Figure 4-12. As was expected the measured TPA photocurrents are maximal for the incident resonance wavelength and consecutively decrease when the wavelength is tuned off cavity resonance. Due to OSNR change between various fiber length combinations the measured TPA photocurrents are not consistent, however the expected trends can be observed. The experimental results are compared with theoretical calculations. Since the relation between experienced accumulated dispersion and resulting pulse width is difficult to calculate for

sech^2 pulse a Gaussian approximation was used. For a Gaussian pulse the accumulated dispersion required to broaden initially transform limited pulse to a given width τ can be written as:

$$|AD| = \frac{2\pi c \tau_0 \sqrt{\tau^2 - \tau_0^2}}{\lambda^2} \tag{4-15}$$

Where τ_0 is the initial Fourier Transform Limited (FTL) pulse width, λ is the signal wavelength and β_2 is GVD parameter. The cavity field transfer function was estimated from the resonance characteristic shown in Figure 4-10 a).

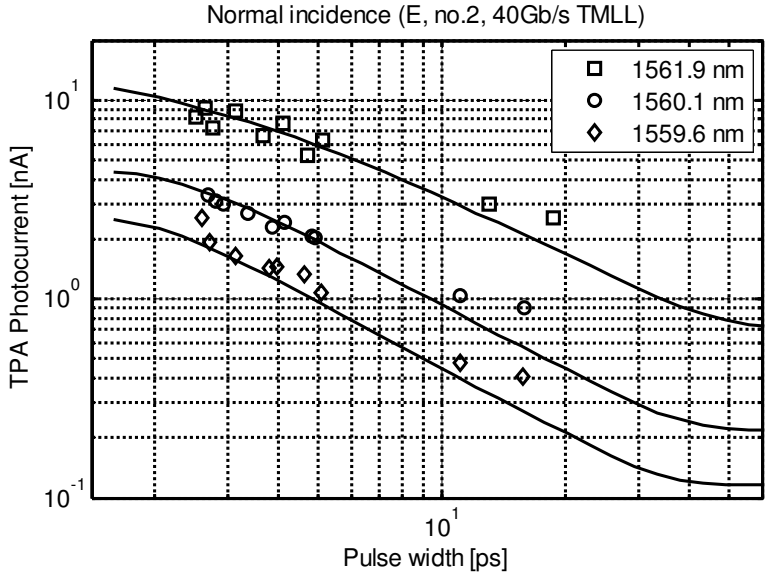

Figure 4-12 Experimental results obtained for resonance (square points) and detuned (circle and diamond points) incident signal wavelength, and calculated responses assuming Gaussian pulse shape (solid lines)

The theoretical model accurately described experimental results with certain inaccuracy resulting from OSNR fluctuations. It can be seen that measured characteristics significantly decreases when the operating wavelength is detuned off resonance. The TPA microcavity can thus be applied for wavelength selective CD monitoring. In the following section a single device will be used for sequential monitoring of two wavelength channels.

4.7.2. Resonance Wavelength Tuning

In this section the performance of a TPA microcavity for CD monitoring was tested in a two-wavelength, 160 Gb/s channel bit-rate, OTDM system. The device under test was initially set at normal position to monitor CD of the first channel and then was rotated to shift the resonance wavelength allowing for monitoring of the second channel. The experimental setup is shown in Figure 4-13. The wavelength channels were generated using two separate TMLL sources driven with a common 10 GHz signal generator. The initial 10 GHz RZ 2ps pulse sequences were

amplified by EDFA's and combined together using a passive optical coupler. The rest of the setup is very similar to the one discussed in the previous sections. A 2^7-1 Pseudo Random bit sequence was simultaneously encoded onto both wavelength channels using the Mach-Zehnder (MZ) modulator. Tunable Optical Delay Lines (ODL) were used to align both channels in the middle of the modulation window and Polarization Controllers (PC) to optimize polarization states before the modulation process. The modulated two-channel signal was next amplified and multiplexed sequentially up to 160 Gb/s using previously described OTDM multiplexer (MUX). Another EDFA was used to compensate for multiplexing loss and various lengths of DCF were used to introduce CD into both channels simultaneously. DCF parameters and lengths were the same as in section 4.5. Optical power after different lengths of DCF was set to a fixed value (-9dBm) using a tunable optical attenuator (ATT) and was amplified using an EDFA to 10 dBm before coupling into the TPA microcavity. A Polarization Controller (PC) was used to optimize incident signal polarization state to obtain maximum nonlinear response measured on highly-sensitive amperometer (PAmmeter).

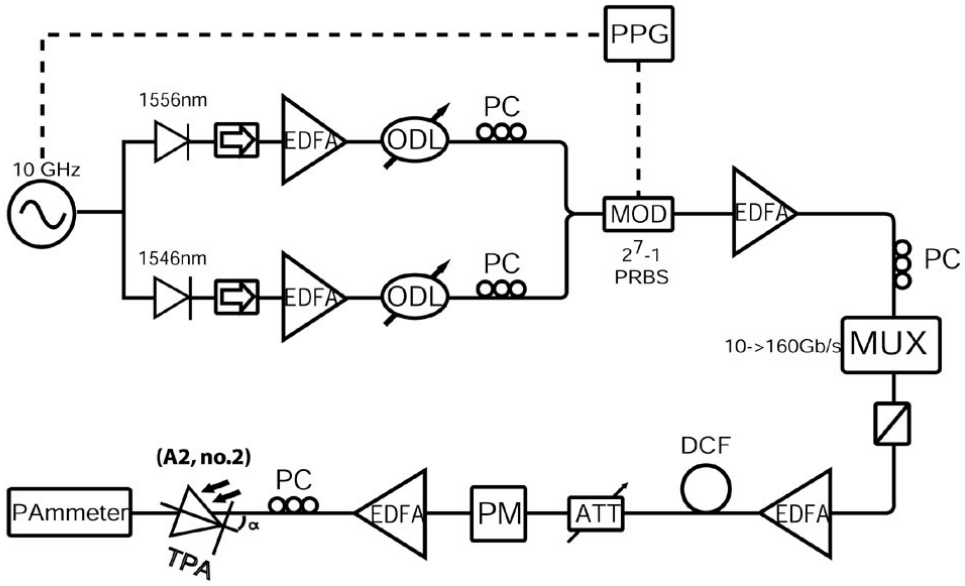

Figure 4-13 experimental setup for sequential CD monitoring of two wavelength channels

The two wavelength channels were separated by 1.25 THz (10nm) operating at 1556 nm (first channel) and 1546 nm (second channel). The large channel separation was set in order to avoid channel cross-interference at this stage. Neighboring channel influence will be discussed in the following section. The device under test was TPA microcavity A2, with the structure no.2. Initial characterization has shown the device resonance wavelength of 1556 nm and bandwidth of 220 GHz (1.8 nm) at normal incidence angle. To shift the resonance wavelength by 1.25 THz the device has to be rotated by 22° which results in device bandwidth broadening to approximately 500 GHz (4 nm). Initially the device was set at normal incidence angle and was illuminated by two channels

operating at 10 Gb/s (MUX stages switched off). Generated TPA photocurrents were measured for successive MUX stages switched on, for varied DCF length configurations. The results are plotted in Figure 4-11 a) for 10 Gb/s, 40 Gb/s and 160 Gb/s bit rates. The device was next rotated by 22° and the measurements were repeated for the second channel with the results plotted in Figure 4-11 b). Solid lines in both figures are simulated nonlinear responses for varied amounts of accumulated dispersion for each bit-rate scenario. The agreement between experimental and theoretical curves is excellent. As was expected the nonlinear response is maximum for fully compensated pulses and decreases gradually with introduced dispersion. The nonlinear response flattening due to pulse overlapping can be clearly seen in Figure 4-11 a) for the first channel operating at 160 Gb/s bit-rate. Apparent flattening of the second channel operating at 160 Gb/s, visible in Figure 4-11 b), results from detection noise-floor rather then the pulse overlapping effect. This resulted from reduced TPA efficiency for rotated device. The high noise floor probably could be reduced by more careful device isolation from the background light during the measurements.

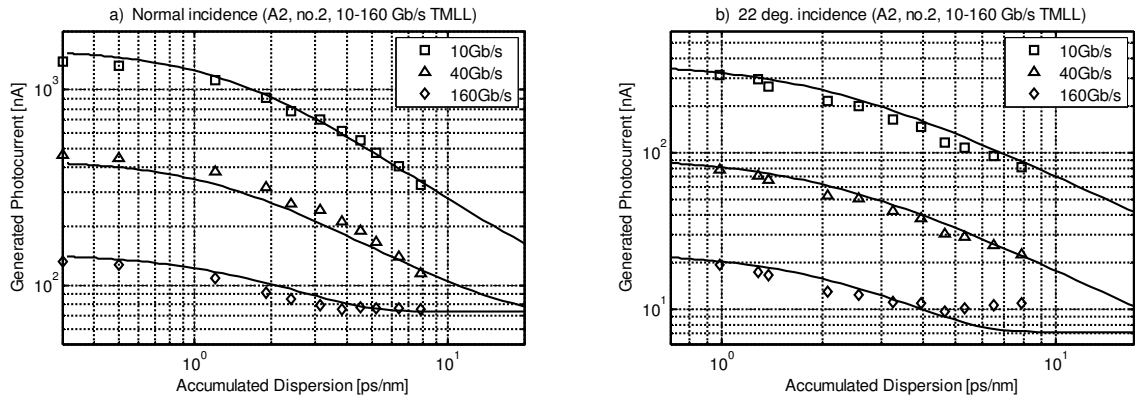

Figure 4-14 Two wavelengths channels sequential monitoring a) Normal incidence angle, b) 22° incidence angle

According to the results CD monitoring can be carried out for 160 Gb/s RZ signal using a current device. The monitoring range is inherently limited by the pulse overlapping effect to ±5ps/nm of accumulated dispersion. The results showed wavelength selective CD monitoring in multi-wavelength system using a single TPA microcavity device. The neighboring channels interference, which put a limit on the minimum wavelength channel spacing, will be investigated in the following section.

4.7.3. Neighboring Channel Interference

The TPA microcavity benefits from resonance characteristics offering the potential for wavelength selective signal processing. In this section the performance of TPA microcavity devices is tested in a two-wavelength system, where an additional wavelength channel is co-propagated with the signal under test. Measurements were taken for three different devices (H, A1, I). First sample H was

characterized with the results shown in Figure 4-15. The device resonance wavelength and bandwidth at normal angle are 1557 nm and 275 GHz (2.2nm). Resonance characteristic was measured using CW laser and PI-curve using 10GHz TMLL pulse source used later in the experiment.

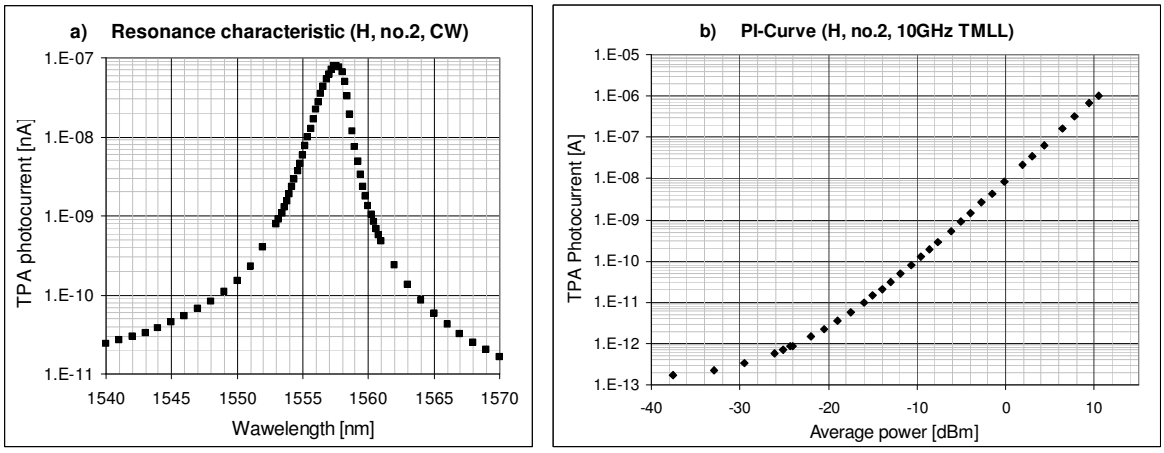

Figure 4-15 Initial characterizations of the TPA microcavity (H, no.2): a) resonance characteristic (CW), b) PI-Curve (10 GHz TMLL)

The experimental setup is shown in Figure 4-16. The cavity was set at normal position which corresponds to 1557 nm resonance wavelength. Two separate TMLL sources were used to generate two wavelength channels with first one operating at a fixed resonance wavelength 1557 nm and the second tuned between 1550 nm and 1557 nm. Optical isolators were used to remove back reflections from the setup. Variable Optical Delay Line (ODL) was placed in the first channel arm allowing for relative, temporal pulse alignment between two wavelength channels. The first channel was passed through varied lengths of SMF, using different combination of 100m, 200m and 1km lengths to introduce varied amounts of dispersion. Both channels were amplified using EDFA's to 5 dBm optical power controlled using in-line power meters. Optical Spectrum Analyzer (OSA) in the second arm allowed for precise control of the second channel wavelength. Both channels were combined using passive optical coupler with one arm connected to oscilloscope (SCOPE) and second arm used for CD monitoring. Similarly as in section 4.6.1 accurate parameters and lengths of different fibers used were unknown, therefore the dispersed pulse widths were measured using SHG autocorrelation technique (Acorr). Polarization controllers in front of the autocorrelator and TPA microcavity were used to optimize polarization of the first channel and additional polarization controller in the second arm to optimize the polarization of the second channel. Generated TPA photocurrent was measured using highly sensitive amperometer (Picoammeter). To investigate the worst case scenario optical pulses in the second channel were kept nearly transform limited during the experiment and were overlapped temporarily with pulses from the first channel when incident onto TPA microcavity. To overlap pulses the ODL was used, with both channels viewed on the

SCOPE allowing for rough pulse alignment. Next the pulses in both channels were precisely overlapped by watching the TPA photocurrent until a maximum value was reached.

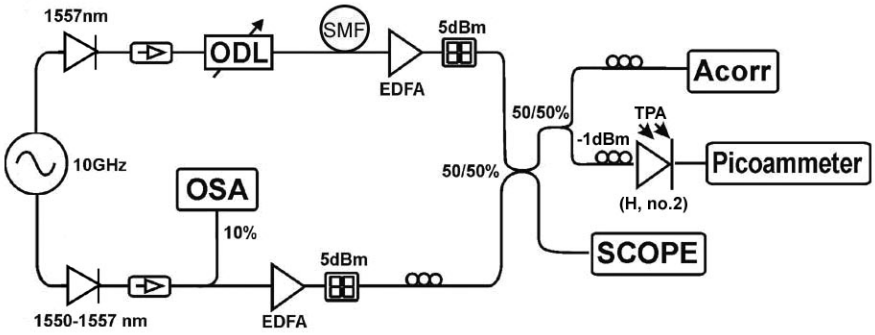

Figure 4-16 Experimental setup to investigate neighboring channel interface on chromatic dispersion monitoring

The experiment was carried in the following order. Initially only the first channel was switched on to measure its pulse width on the autocorrelator. Next the second channel was switched on and set to the required wavelength on the OSA. Pulses in both channels were overlapped temporarily and the corresponding TPA photocurrent was recorded. Next the amount of dispersion in the first channel was changed using different fiber lengths and the corresponding pulse width was measured (with the second channel switched off). At each step TPA photocurrent versus the first channel pulse width was recorded. Next the whole procedure was repeated for different detuning. The experimental results are plotted in Figure 4-17 where accumulated dispersion is evaluated from the measured pulse widths, using Gaussian approximation according to the equation (4-3).

Average optical power from the first channel coupled into the device was -1dBm. According to the PI-curve plotted in Figure 4-15 b) this corresponds to a TPA photocurrent of 6 nA. It can be seen that the measured value for the first channel only, for not dispersed pulse is 8 nA which is in a good agreement with the initial characterization. The slightly higher measured TPA photocurrent may result from the fact that pulses from TMLL source, which are initially pre-chirped with small amount of negative linear dispersion, were possibly compressed by fiber lengths in the setup resulting in the higher photocurrent. Furthermore the signal in the first arm is expected to have slightly degraded OSNR due to EDFA used. The additional channel influence was investigated for detuning up to 860GHz (6.9 nm). For higher channels separation the fractional influence of the additional channel was too small to optimize the second channel polarization state.

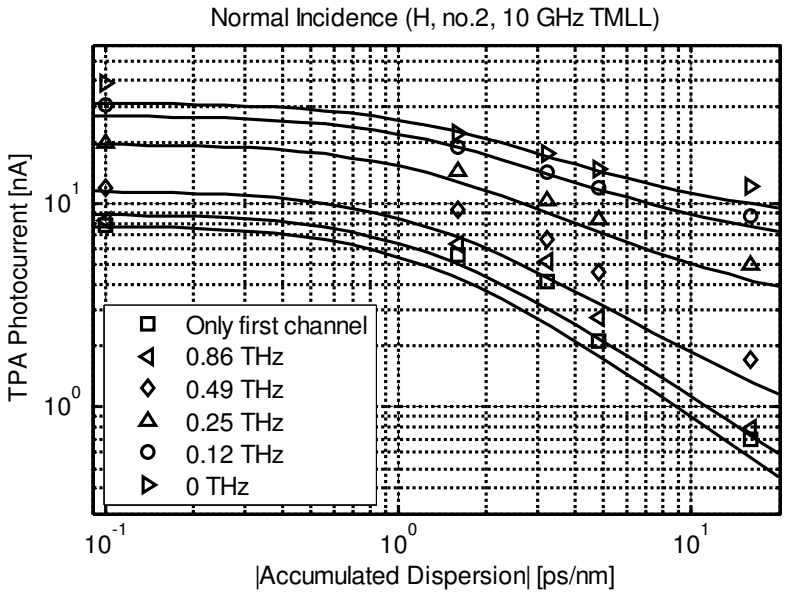

Figure 4-17 TPA photocurrent versus accumulated dispersion for two wavelengths-channel system. Experimental results (points) and simulated curves (solid lines)

Experimental results are compared with theoretical lines calculated for the initial 1.4 ps $sech^2$ pulses, broadened by varied amounts of accumulated dispersion. The TPA microcavity was modeled to match the initially measured resonance characteristic. Visible TPA photocurrents deviations from the theoretical lines, like in section 4.6.1, resulted from varied OSNR. Additional deviation may be caused by assumptions taken to measure pulse width using autocorrelation technique. The accuracy of the measurement decreases significantly for strongly dispersed pulses, due to lower peak power of the signal. Furthermore the initially $sech^2$ pulse changes the shape due to CD. Thus pulse width evaluation based on $sech^2$ shape assumption became less accurate for strongly dispersed pulses. Finally the Gaussian approximation used to evaluate the experienced accumulated dispersion may introduce additional inaccuracy. The experimental results however follow the expected trends for various detuning. The influence of the additional channel is clear, resulting in an increase in the TPA current. According to the expectations, around zero dispersion the TPA photocurrent generated by two overlapped signals operating at the same wavelength (zero detuning) is four times greater compared to the first channel only scenario. To quantify the influence of the additional channel the following dB measure was used:

$$Influence = 10\log\left(\frac{I_1}{I_2}\right) \tag{4-16}$$

where I_1 is the TPA photocurrent measured for the first channel only and I_2 is the TPA photocurrent measured with the additional channel. The influence of the second channel decreases gradually with increased detuning and reaches approximately 0.5 dB for 0.86 THz detuning (around zero dispersion). Since the second channel pulse width was fixed (analysis of the worst case scenario) its

influence becomes relatively more significant at the high accumulated dispersion range. When the TPA photocurrent decreases due to dispersion introduced in the first channel, the second channel remains nearly transform limited thus causing high cross-channel interference. The influence of the second channel detuned by 0.86 THz from the first channel dispersed by 10 ps/nm was measured as 1 dB.

A similar experiment was carried out for a sample A1, having the same no.2 structure. The initial device characteristic is shown in Figure 4-18. The device resonance wavelength and bandwidth at normal incidence are 1558.7 nm and 248 GHz (2nm) respectively.

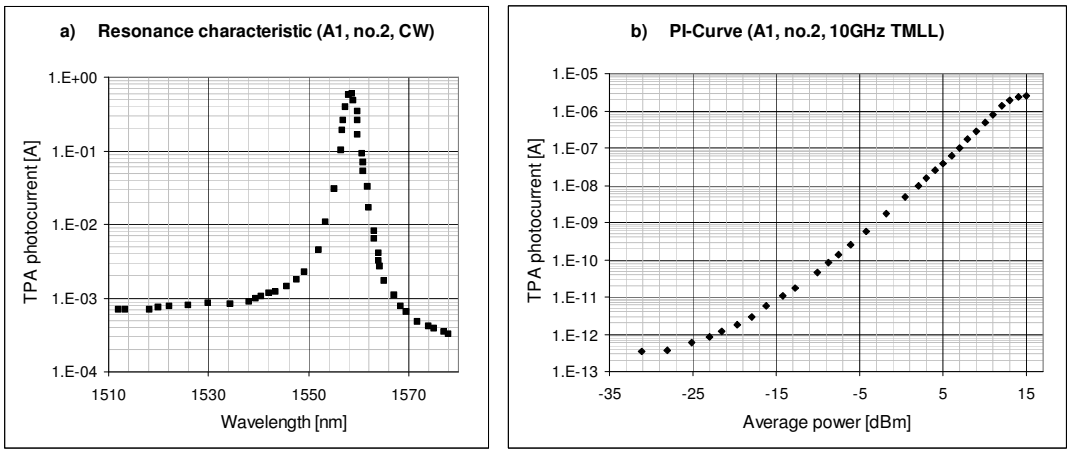

Figure 4-18 Initial characterizations of the TPA microcavity (A1, no.2): a) resonance characteristic (CW), b) PI-Curve (10 GHz TMLL)

This time however, as in section 4.6.2, the known lengths of DCF were used here, thus pulse width measurement during the experiment was not necessary. Accumulated dispersion was simply calculated by multiplying the dispersion parameter by the adequate fiber length. Since the autocorrelation arm was removed from the setup, as shown in Figure 4-19, much higher optical powers could be coupled into the TPA microcavity. To simulate more common telecommunications scenarios both channels were passed through the same lengths of DCF. To avoid problems with OSNR fluctuations optical power after each DCF configuration was attenuated to the fixed value of -7dBm. The device mounting stage allowed for the incidence angle change however at this stage optical light was coupled at normal incidence.

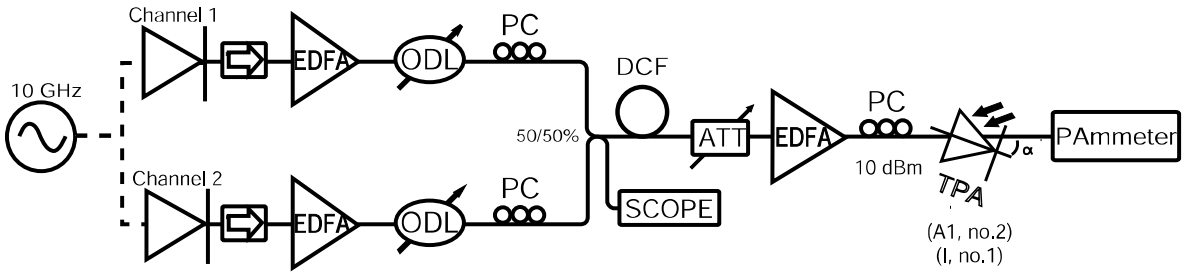

Figure 4-19 Experimental setup to investigate neighboring channel interface on chromatic dispersion monitoring

The first channel wavelength was fixed at resonance 1556 nm and the second channel was initially set at 1546 nm. Both channels were combined together using an optical coupler. Channels temporal overlapping and wavelength alignment was controlled using oscilloscope (SCOPE) and Optical Spectrum Analyzer (OSA) was connected to the remaining coupler arm. Optical power before the TPA microcavity was amplified to 10 dBm. The measurement procedure was the same as in previous setup. Recorded TPA photocurrents versus accumulated dispersion experienced by the first channel are plotted in Figure 4-20 for various channel separation. Again theoretical calculations were carried out to compare with the experimental setup, represented by solid lines in Figure 4-20. Excellent agreement between the theoretical lines and the measured experimental points can be seen. Since both channels were dispersed the second channel influence is not as significant at high accumulated dispersion as in the previous scenario. The device performance around zero dispersion is very similar to the previous sample (see Figure 4-17) since both devices have similar bandwidths.

In communications channels separation is commonly set as four times of the transmitted bit rate. The 2 ps pulses used in this experiment are in general suitable for 160 Gb/s RZ transmission. The second channel influence for 0.68 THz separation (around 4 x 160Gb/s) was measured as 0.37 dB around zero dispersion and 0.59 dB when the first channel was dispersed by 10 ps/nm. Note that the second channel in this case operating at 1546 nm, experienced much less (in magnitude) accumulated dispersion. Therefore its relative influence on CD monitoring of the first channel increases with higher accumulated dispersion.

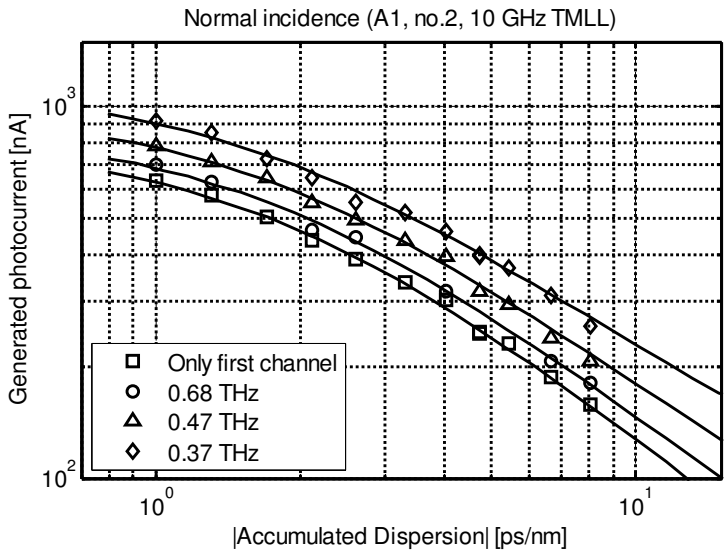

Figure 4-20 TPA photocurrent versus accumulated dispersion for two wavelengths-channel system. Experimental results (points) and simulated curves (solid lines)

The same experimental setup was used to characterize a wide bandwidth TPA microcavity (I, no.1). The new sample was mounted on the rotation stage and initially characterized for normal and 34° incidence angles. These angles are later used in the experiment. Initial characterizations are shown in Figure 4-21. The device resonance wavelength and bandwidth at normal incidence are 1562.5 nm and 625 GHz (5nm). The resonance wavelength shifts by 2.25 THz (18.5nm) towards 1544 nm, and the cavity bandwidth increases to 1.75 THz (14 nm) at 34° angle. Also the nonlinear response reduces by a factor of 5 for the rotated device according to the PI curve measured. The device was initially set at normal incidence angle and the first channel wavelength was set to the resonance 1562.5 nm. Next CD monitoring was carried out for the first channel only and with the second channel on, for various channels spacing. Next the first channel was tuned to 1544 nm and the experiment was repeated for the device rotated by 34°. The results are plotted in Figure 4-22 for the normal incidence (a) and for the rotated device (b).

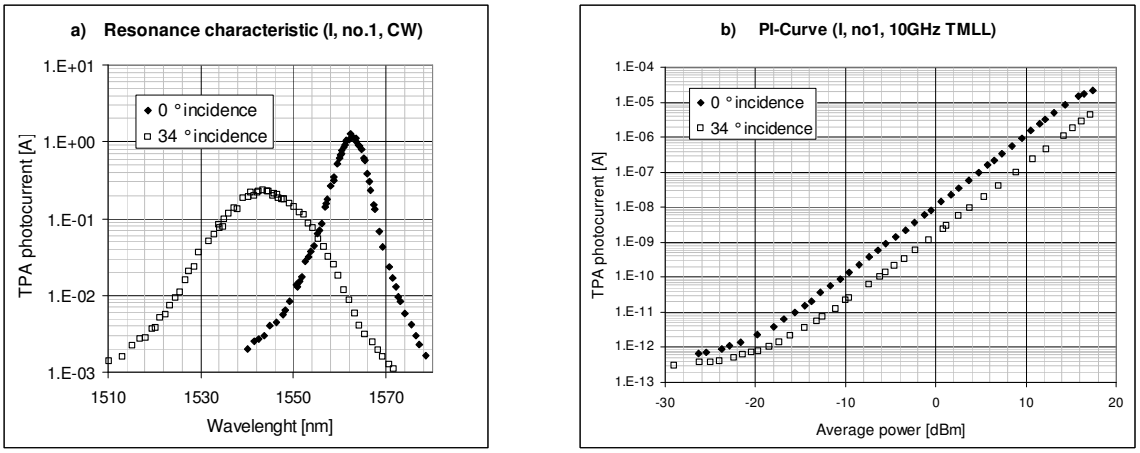

Figure 4-21 Initial characterizations of the TPA microcavity (I, no.2): a) resonance characteristic (CW), b) PI-Curve (10 GHz TMLL)

Since the device bandwidth for this sample is much wider then for previously used samples with structure no.2, the influence of the additional channel is significantly greater compare to the previous results shown in Figures 4-17 and 4-20. This influence is even higher for the rotated device due to the wider bandwidth. For example the influence for 1 THz spacing was measured to be 1.9 dB for normal incidence and 2.6 dB for 34° incidence. For dispersed signals (10 ps/km.nm) these increase to 3.6 dB for the normal incidence and 5 dB for 34° incidence. The reason that the influence increases is because the second channel was less dispersed when propagated through the fiber due to the shorter wavelength.

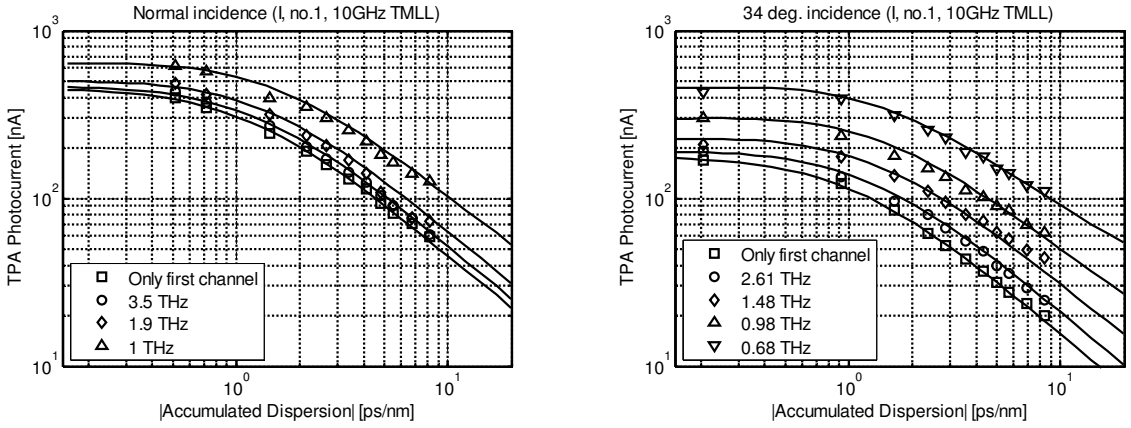

Figure 4-22 Additional channel influence on chromatic dispersion monitoring using TPA microcavity operating at normal (a) and 34° (b) incidence angles.

Large channel spacing would be required for accurate CD monitoring using this device. However such a wide bandwidth device would be accurate for processing of extremely high speed signals (above 600 GHz) which would require high channels separation anyway. In communication systems commonly channel spacing of approximately four times the channel bandwidth is required.

4.8. Optimal Device Performance

A narrow bandwidth device reduces neighboring channel influence on the nonlinear detection, but at the same time if the device bandwidth is narrower than the incident signal bandwidth most of the monitoring channel power is filtered out by the cavity. The optimal device performance would be achieved for a device bandwidth corresponding to the incident signal bandwidth. In such a scenario the cavity filtering results in a small monitored signal change while significantly suppressing neighboring channels. WDM systems utilizing RZ modulation format commonly operate with 33% duty cycle with channel frequency spacing approximately four times of the channel bandwidth. In this section a theoretical investigation is carried out using the same model as previously to investigate an optimal performance of the TPA microcavity device. Three scenarios were modeled for 40 Gb/s, 80 Gb/s and 160 Gb/s incident signals. Each signal was operating with the same 33% duty cycle and was incident onto 40 GHz, 80GHz and 160 GHz bandwidth device appropriately. Influence of the additional channel was modeled for each scenario assuming channel spacing four times of the channel bit rate. The calculated TPA photocurrents versus magnitude of the incident accumulated dispersion are plotted in Figure 4-23 for a single channel (solid) and with an additional channel (dashed) cases. Since the simulated duty cycles and optical average powers were the same the maximum TPA photocurrents for incident FTL pulses are the same for each scenario. Similarly the flattening levels, proportional to the square of the incident average optical power are the same as well. A dramatic decrease however, in the monitoring range can be seen for the increased bit rates. When the incident bit rate doubles the monitoring range divides by a factor of four. It can be seen that for each scenario the influence of the additional channel also remains the same, since the channel spacing is proportional to the monitored signal bandwidth. The influence for each scenario was calculated to be 0.37 dB. Since both signals were dispersed simultaneously the influence remains invariable with introduced dispersion.

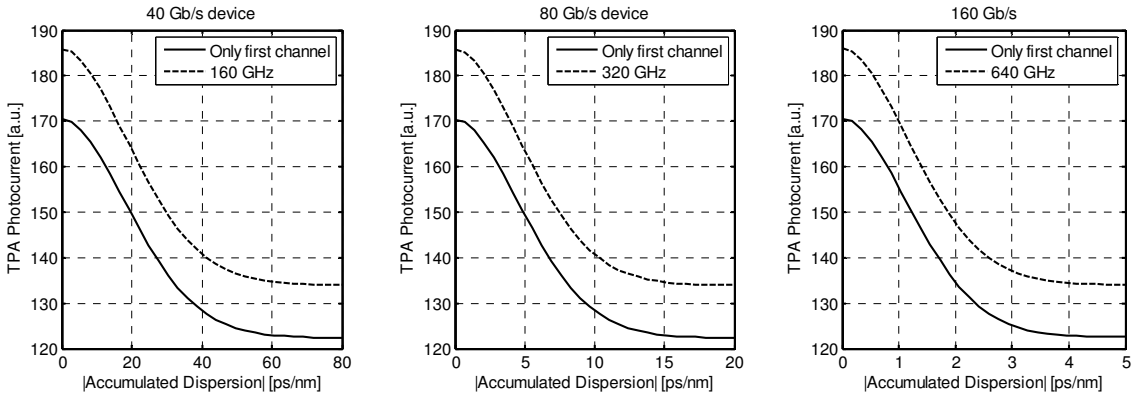

Figure 4-23 Modeling of CD monitoring for 40 Gb/s, 80 Gb/s and 160 Gb/s signals for single channel (solid) and with additional channel spaced by 4 times of the channel bit rate.

4.9. Optical Sampling

TPA photodetection can be applied for high speed all-optical, temporal characterization. It is ideally suited for real time CD fluctuation monitoring, resulting from change in environmental conditions. Direct detection however provides limited information, and requires additional knowledge of the monitored signal (e.g. pulse shape). More accurate signal characterization can be carried out involving autocorrelation, optical sampling, FROG and other techniques. In this section a prototype design of all-optical, wavelength selective, sampling oscilloscope based on TPA microcavity photodetector will be described.

Optical sampling, as was described in section 2.5, is realized by nonlinear detection of a periodic signal under test overlapped with a significantly shorter sampling signal. By varying a delay between tested and sampling signals a unique cross-correlation signal representation can be measured. Unless high (sub-wavelength) stability between the signals is maintained only the intensity cross-correlation components are measured with the interferometer fringes being lost. The nonlinear response for incident signal under test E_t, and sampling signal E_s electric fields can be written as:

$$S(\tau) \propto \int_{-\infty}^{\infty} \left| E_t(t) + E_s(t-\tau) \right|^4 dt \propto \int_{-\infty}^{\infty} p_t(t)^2 dt + \int_{-\infty}^{\infty} p_s(t-\tau)^2 dt + 2\int_{-\infty}^{\infty} p_t(t)\, p_s(t-\tau) dt \qquad (4\text{-}17)$$

where $p_{t/s}(t)=|E_{t/s}|^2$ are the tested/sampling signals optical power envelopes and τ is the temporal delay between the signals. First and second components on the right hand side of the equation (4-17) results in a constant background proportional to the incident signals powers squared. The third cross-correlation term however, depends on the signals relative temporal delay τ. The sampling pulses commonly operate at the same or sub-harmonic repetition rate as the signal under tests. The pulse duration should be shorter than the signal under test for accurate measurement. By varying the optical delay τ the signal under test can be scanned across by the sampling pulses as visualized in Figure 4-24 a). The resulting cross correlation signal with the constant background is plotted versus the delay τ in Figure 4-24 b). The cross-correlation signal amplitude is proportional to the product of both signals optical powers and can be easily improved by increasing the sampling signal peak power. A significant peak power increase can be achieved by reducing the sampling signal repetition rate to the lower sub-harmonic frequency. In the experimental work the signal under test was operating at 10 GHz rate and sampling signal at 10 MHz. Lower repetition rate however, also increases the constant background. A condition for a maximum contrast between the cross-correlation signal and the constant background can be written as:

$$\frac{pp_s}{pp_t} = \sqrt{\frac{d_t}{d_s}} \tag{4-18}$$

where $pp_{s/t}$ and $d_{s/t}$ are sampling/tested signals peak powers and generalized duty-cycles respectively. Usually for a given signal duty cycle the peak power of the sampling signal is varied to obtain the maximum contrast. The contrast change for varied sampling signal peak power is plotted in Figure 4-24 c) for 5 dBm average optical power 10 GHz, 2ps Gaussian pulses scanned by a 10 MHz sequence of 0.8 ps Gaussian pulses (similar parameters were used latter in experiment). The maximum contrast occurs for sampling signal peak power of 7W which corresponds to the average power of approximately -13 dBm, which can be easily achieved using the laboratory equipment available.

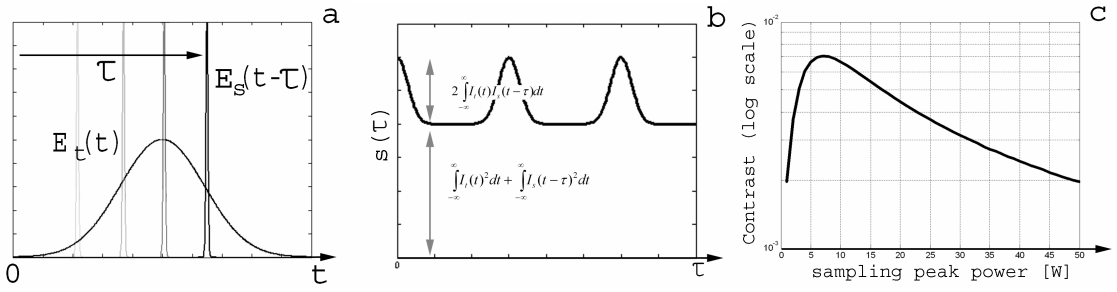

Figure 4-24 Optical Sampling: a) sampling signal scanned across signal under test, b) resulting cross-correlation signal, c) cross-correlation signal to the background contrast for varied sampling peak power

The temporal delay between signals can be controlled by introducing a manually or periodically varied temporal delay element, or alternatively by introducing a small difference between test and sampling signal repetition rates. In the last approach successive pulses from both signals reach the nonlinear photodetector at a slightly different time. Whenever the sampling pulse approaches the nonlinear detector a cross-correlation product between the overlapped signals is generated proportional to the tested signal instant optical power. The scanning frequency corresponds to the tested and sampling signals frequency detuning. Performance of the TPA microcavity sample (E, no.2) was tested experimentally using the setup shown in Figure 4-25. Signal under test operating at 10 GHZ repetition rate was scanned by 0.7 ps pulses operating at a sub-harmonic frequency of 10 MHz with 1 kHz detuning. According to the previous discussion cross-correlation product between test and sampling signal is measured every 100 ns with 1 kHz scanning frequency. The measured signal was displayed on a low bandwidth oscilloscope not capable of tracking every single scanning event thus an averaged signal was recorded.

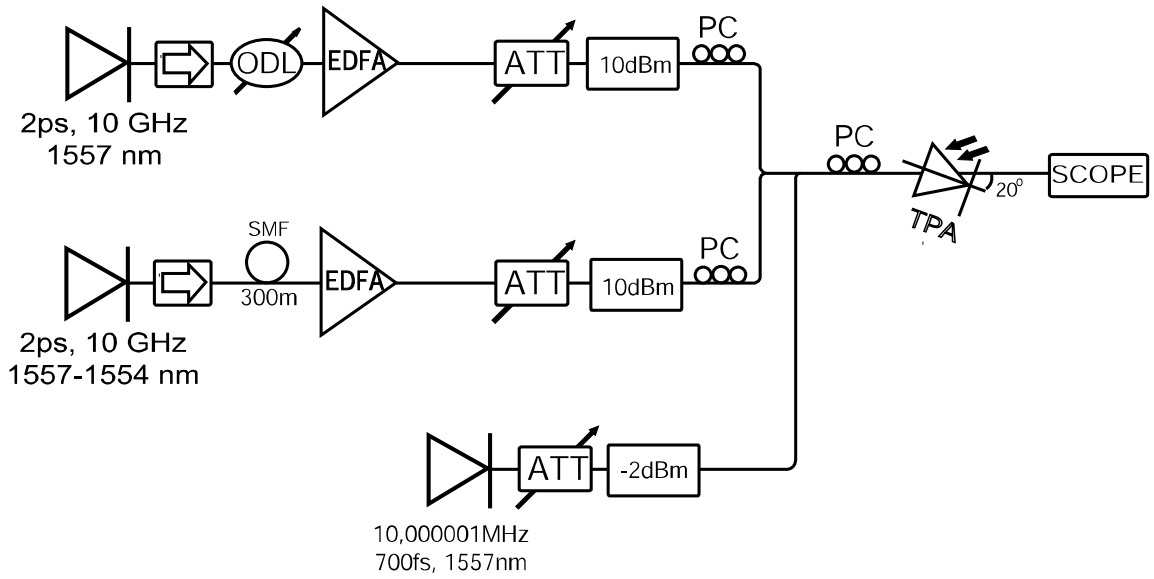

Figure 4-25 Experimental setup used to investigate TPA microcavity performance for optical sampling

In the experiment two parallel channels operating at the same 10 dBm average optical power were sampled simultaneously. The second channel was passed through 300 m SMF for easier differentiation between the signals. Measured cross-correlation sampling traces are plotted in Figure 4-26.

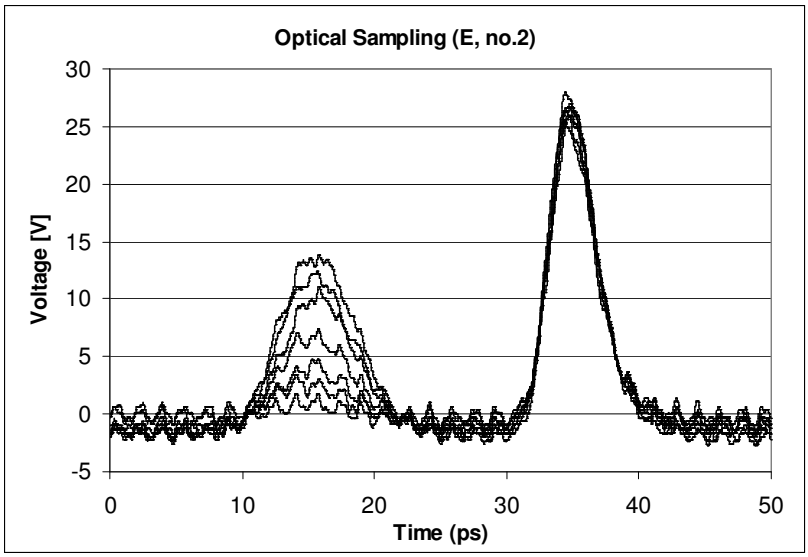

Figure 4-26 Cross-correlation trace of two wavelength channels. First (narrow) channel was operating at fixed resonance wavelength while second channel (wide) was tuned off resonance

Initially both sampled signals were operating at the same 1557 nm chosen to match the sampling pulse source wavelength, and the TPA microcavity was rotated by 20° which corresponds to 1557 nm resonance wavelength and approximately 280 GHz bandwidth. The second channel was

successively tuned off resonance with decreased sampling signal amplitude recorded on the scope. The generated pulses in both channels are best described by $sech^2$ power envelope profile with 1.4 ps FWHM (FTL). Due the initial prechirp the first channel pulses were approximately 2 ps long when coupled into the TPA microcavity. The second channel pulses were broadened due to propagation through 300 m SMF to approximately 12 ps. Measured on the oscilloscope pulse widths were 3.8 ps and 7 ps for the first and second channels respectively. This inaccuracy can be easily explained by considering the cavity filtering effects on the monitored and sampling signals. The optical bandwidth associated with 1.4 ps FTL $sech^2$ pulses is 228 GHz. The initial 2 ps pulses would be though minimally broadened to 2.2 ps due to the cavity filtering property. Similarly the sampling pulses having approximately 875 GHz bandwidth will broaden within the cavity resulting in minimum 0.81 ps pulses. In practice due to the initial nonlinear prechirp, and additional SPM experienced during propagation through the experimental setup, sampling pulses within the cavity would be expected to be around 1.5 ps. This cavity broadening effects resulted in measured the first channel 3.8 ps width.

On the other hand the second channel was measured to be narrower then expected 12 ps. This is due to described before in section 4.4, cavity-induced dispersed pulse narrowing. Dispersion experienced by the second channel during the propagation within 300 SMF, was partially canceled due to the cavity filtering effect. This resulted in measured 7 ps width of the second channel pulses.

Consequently the sampling resolution is significantly limited by the cavity filtering effects. The main limiting factors are sampling pulse temporal broadening by the cavity and the cavity influence on the signal under test. In addition test and sampling signals were generated from separate sources driven by separate signal generators. The generators were synchronized using 10 MHz external clock signal resulting in pure signals temporal stability. This imposed an additional temporal jitter between test and sampling signals causing additional sampling signal broadening.

To carry out accurate optical sampling measurements TPA device with a wide bandwidth, comparable to the sampling signal bandwidth, should be used. In addition to maximize the temporal stability the sampling pulses should be driven by a clock signal retrieved directly from the signal under test.

4.10. Summary

Chromatic dispersion (CD) is a critical limiting factor for high-speed transmission. High-bit rate systems require wide bandwidth signals which are more sensitive to dispersion broadening. At the same time with increased data rate, acceptable dispersion limit shrinks due to a shorter bit period

and faster pulse overlapping effects. Consequently, overall system resistance to CD reduces proportionally to the square of the incident bit rate. Dispersion management is a common way to design transmission link with nearly zero net dispersion between networking nodes. In practice however additional environmental factors, such as temperature change, influence the net dispersion of the link. High-speed systems, due to limited tolerance to CD, are likely to require additional adaptive compensation schemes with continuous dispersion monitoring capabilities. TPA microcavity is an ideal candidate for nonlinear signal quality monitoring of WDM channels.

This chapter presented an experimental investigation of the TPA microcavities performance for CD monitoring. Experimental results confirmed the devices sensitivity to the incident RZ signal broadening due to CD. The devices wavelength selectivity due to resonance cavity enhancement was investigated both experimentally and theoretically. A simple model allowing for device performance modeling, based on initially measured characteristics, has been developed. The theoretical model successfully described device performance for various incident pulse shapes and different cavity bandwidths. CD monitoring is limited due to pulse overlapping effect, and this has been discussed in a great detail. According to the experimental results CD monitoring of 160 Gb/s signal can be performed within ±5 ps/km.nm accumulated dispersion range. The influence of an additional channel was measured for various channel spacing, for different bandwidth devices. An optimal performance would be achieved for the device bandwidth exactly matching the monitored signal bandwidth. In such a case the influence of an additional channel, assuming channel spacing equal to four times of the channel bandwidth, would be 0.36 dB.

An alternative optical sampling technique allowing for temporal signal characterization was demonstrated using a TPA microcavity device. The measurement accuracy has been shown to be severely limited by the cavity filtering property. For accurate characterization a device with greater bandwidth compared to the sampling signal should be used. Nevertheless a potential of TPA microcavity for optical sampling has been shown.

References

[1] E. A. Golovchenko, Neal S. Bergano, and C. R. Davidson, "Four-Wave Mixing in Multispan Dispersion-Managed Transmission Links," *IEEE Photonics Technology Letters*, vol. 10, no. 10, October 1998

[2] L. Garrett, R. Vodhanel, S. Patel, R. Tkach, and A. Chraplyvy, "Dispersion Management in Optical Networks," *in European Conference on Optical Communication* (ECOC'97)., Edinburgh, Scotland, 1997.

[3] Sascha Vorbeck and Ralph Leppla, "Dispersion and Dispersion Slope Tolerance of 160-Gb/s Systems, Considering the Temperature Dependence of Chromatic Dispersion," *IEEE Photonics Technology Letters*, vol.15, no.10, 2003

[4] T.Kato, Y.Koyano and M.Nishimura, "Temperature Dependence of Chromatic Dispersion in Various Types of Optical Fibers," *in Conference on Optical Fiber Communication* 2000, vol.1, pp 104-106, paper TuG7

[5] http://lw.pennnet.com/Articles/Article_Display.cfm?Section=ARTCL&SubSection=Display&PUBLICATION_ID=13&ARTICLE_ID=343292&dcmp=LWDENL

[6] J.Azana, M.A. Muriel, "Technique for multiplying the repetition rates of periodic trains of pulses by means of a temporal self-imaging effect in chirped fiber gratings," *Optical Letters*, vol.24, no.23, pp. 1672-1674, (1999)

[7] D.Pudo, M.Depa, L.R. Chen, "Single and Multiwavelength All-Optical Clock Recovery in Single-Mode Fiber Using the Temporal Talbot Effect," Journal of Lightwave Technology, vol. 25, no. 10, pp. 2898-2903, Oct. 2007

CHAPTER 5. Conclusion and Future Outlook

With the introduction of a new generation of broadband services such as High Definition (HD) television, network operators face both opportunities and challenges. The shift towards HD programming and all-digital production techniques rapidly reshapes broadcast industries creating a demand for a high-bandwidth delay-sensitive content transmission. The majority of today's backbone networks are not prepared to meet the capacity, quality-of-service (QoS), and flexibility demands of a new era HD media production, contribution, and distribution. Novel approaches are required to maximize core network bandwidth efficiency, enable rapid provisioning of end-to-end service capacity, and ensure the guaranteed performance levels.

As was discussed in chapter 1 a way to better exploit the bandwidth offered by the optical fiber is to use multiplexing schemes to transmit multiple data channels simultaneously. Wavelength Division Multiplexing (WDM) technology which is globally used presently, benefits from simple implementation. The speed of individual wavelength channels however is limited by the electronic processing speed limits. Thus in current systems, to accommodate increasing bandwidth requirements new wavelength channels have to be added within the optical bandwidth available. A large number of WDM channels may result in complex system design and difficult network management. Alternatively the capacity can be improved by increasing the individual channel rates. This high-speed transmission requires signal processing carried out in the optical domain.

The ability of optics to be the most cost effective solution for ultra-high capacity transmission motivates a development of ultra-short pulse generation techniques and novel all-optical signal processing techniques. With increased transmitted data rates the system tolerance for fiber impairments significantly decreases. This includes Chromatic Dispersion (CD), Polarization Mode Dispersion (PMD), nonlinear signal distortion, nonlinear channel cross-talk and other effects. Thus novel techniques are investigated to allow for continuous signal performance monitoring and adaptive compensation within existing infrastructures. In particular CD is considered as one of the main high speed systems limiting factors. Additional fluctuations imposed by environmental conditions changes became difficult to mitigate against problem when transforming towards ultra-fast transmission.

All-optical techniques based on optical nonlinearities are potential candidates for a number of future networking operations. In chapter 2 example configurations allowing for nonlinear timing extraction, high-speed switching, wavelength conversion and other operations have been discussed. The applicability for high-speed RZ signal performance monitoring was explained in great detail. In

principle the nonlinear detection averaged over the incident signal period provides information about the incident pulse duration. This technique is inherently asynchronous and requires no additional timing extraction. Due to nearly instantaneous nonlinear response it can be applied for ultra high-speed signal monitoring. Another important property of the nonlinear detection is intrinsic sensitivity for the incident Optical Signal to Noise Ratio (OSNR). Due to the statistical nature of the optical noise an average nonlinear response for the incident ASE signal would be two times that of the incident Continuous Waveform of the same optical power. This property can be utilized for in-band OSNR measurements.

The nonlinear process of Two-Photon Absorption (TPA) introduced in chapter 3 is a potential candidate for high-speed applications. The TPA process within a semiconductor medium results in the generation of a nonlinear TPA photocurrent. A TPA photodetector in a pin configuration can be designed, in order to combine both optical nonlinear process and optical-to-electrical conversion within a single device. This offers a significant simplification over commonly used all-optical techniques based on SHG nonlinearity. The TPA photodetector can replace the SHG nonlinear crystal and the following linear detector without the requirement for additional phase matching adjustments. Such a device benefits from high-speed nonlinearity, for example all-optical switching of 10 Gb/s channel from 160 Gb/s OTDM signal can be carried out using 10 GHz clock signal. The only requirement for the TPA photodetector electrical bandwidth would be to operate at the switched 10 Gb/s electrical signal rate. To achieve the required electrical bandwidth with satisfactory device sensitivity a Resonance Cavity Enhancement (RCE) technology can be utilized. In this approach the interaction time between the light and the active region increases (cavity life-time), however the most limiting factor, electrical bandwidth is improved. The increased interaction time limits the optical speed of the device since the incident signal bit period should not exceed the cavity life-time.

An additional advantage of the RCE detector is the resonance characteristic. Incident signals operating around the resonance wavelength experience significant enhancement within the cavity while off-resonance incident wavelengths are severely suppressed. The cavity optical bandwidth measured is inversely proportional to the cavity life time. Another benefit of the RCE structure is the possibility of resonance wavelength tuning by rotating the incident angle.

Various prototype TPA microcavities were fabricated according to three different designs. Experimental work presented in chapter 3 included the devices initial characterization demonstrating a nonlinear response over nearly five orders of magnitude dynamic range. Resonance characteristics and corresponding optical bandwidths for three different TPA microcavity designs

were measured. According to the design, optical bandwidths of various samples were measured ranging from 124 GHz to 640 GHz. The resonance wavelength tuning and corresponding resonance characteristics change due to the incident angle tuning was demonstrated. The resonance wavelength was tuned by 60 nm when rotating the device by 60°. The electrical bandwidth of selected TPA microcavity was measured to be 5 GHz, using impulse response technique.

The TPA microcavity device can be used for high-speed RZ signal CD monitoring utilizing direct nonlinear detection. According to the discussion given in chapter 4, nonlinear TPA response will be maximum for fully compensated, Fourier Transform Limited (FTL) incident pulses. Since the maximum speed of the monitored incident signal is limited only by the cavity life-time (inverse of the cavity optical bandwidth) the fabricated devices could be applied for CD monitoring of signals above 100 Gb/s range. A theoretical model allowing for performance investigation of various incident bit rate signals and different devices bandwidths was presented. The cavity wavelength-selectivity effects limiting the processing speed were observed both in experimental work and theoretical simulations. The wavelength selective CD monitoring was investigated in quasi multi-wavelength high-speed system for various channel spacings. According to the results an optimal performance would be achieved for a device with optical bandwidth matching the incident signal bandwidth. The influence of an additional channel in a typical WDM system utilizing RZ modulation format was estimated as 0.36 dB. The ability of selective wavelength monitoring was demonstrated utilizing the resonance wavelength tuning by incident angle change.

A prototype compact device combining optical nonlinearity and optical-to-electrical conversion was elaborated and tested in a practical application. The devices sensitivity is expected to be significantly improved by integration with a Trans-Impedance Amplifier (TIA), ensuring TPA photocurrent amplification and device impedance matching with measurement instrumentation. The fabricated device performance offers a wide area for potential applications. Further device performance optimization might be possible. Two orthogonal incident polarization modes TE and TM can be distinguished for the TPA microcavity photodetector. Depending on the incident light polarization state the devices would have different resonance characteristics. This might be helpful to minimize the bandwidth change with increased incident angle by precise control of the incident polarization state. This property also offers a potential for PMD impairment measurements, recognized as another crucial high-speed system limiting factor. A wavelength selective TPA microcavity in conjunction with linear detector can be used for a frequency scanning of the incident signal. The ratio between the linear and nonlinear responses can provide information about the signal in-band OSNR. This could be an attractive feature for optical spectrum analyzers. The demonstrated CD monitoring could be extended by analyzing TPA microcavity device performance

for more complicated optical modulation formats utilizing phase and polarization multiplexing. Integration of the TPA microcavity with commercially available tunable, linearly and nonlinearly chirped Fiber Bragg Gratings (FBG) can be used to design a compact all-optical adaptive CD compensation module.

This type of CD monitoring has not been performed before to the best of our knowledge. As outlined in the first chapter adaptive compensation for temporal impairment fluctuations is required to accommodate existing networks for high-speed transmission in a cost-effective manner. A key element for impairment compensating devices will be an accurate signal performance monitoring module, operating preferably on channel-by-channel basis. A prototype device allowing for a wavelength selective CD monitoring was designed, fabricated and tested in an experimental environment.

Appendix A. Matlab Code

In this work the theoretical simulations were carried out within MatLab language for technical computing, utilizing a theoretical model described in section 3.5.2. All simulation results were obtained basing on the simplified code described below. The code is divided into *main body* code and *itpafft* function. The main body code calls *itpafft* function with varied parameters to obtain in return a TPA photocurrent. The *itpafft* function is designed to calculate TPA photocurrent response of a microcavity device, for two incident wavelength channels, with the first channel being dispersed.

MAIN BODY CODE:

```
-------------------------------------------------------------------------
clear all
clc

c=299792458;    %speed of light [m/s]
N=30;           %number of simulation points

AD=linspace(0,5,N);     %accumulated dispersion [ps/nm]
spacing=[10000,4*160];    %frequency detuning between channels

for a=1:length(spacing)
    for b=1:N
        Titpa(a,b)=itpafft(AD(b),2,0.96,160,1550,15,spacing(a));
    end
end

set(0,'DefaultAxesLineStyleOrder',{'-','--'})

figure(1)
plot(AD,Titpa,'k')
xlabel('|Accumulated Dispersion| [ps/nm]')
ylabel('TPA Photocurrent [a.u.]')
legend([num2str(spacing(1)),' GHz spacing'],[num2str(spacing(2)),' GHz
spacing'],'location','NorthEast')
title('160 GHz incident signal')
axis([0 5 110 190])
grid on

set(0,'DefaultAxesLineStyleOrder','remove')
set(0,'DefaultAxesColorOrder','remove')
-------------------------------------------------------------------------
```

The *itpafft* function requires on its input the first channel accumulated dispersion (AD), FTL FWHM of both channels pulses, geometric average reflectivity of the microcavity device (R), incident signal bit rate (rate), incident signal wavelength, even number of periods required for pulse overlapping modeling (Pnumb) and frequency detuning between two channels. The mirrors geometric average reflectivity (and FSR) can be found by carrying out initial device resonance

characteristics. The *itpafft* function returns calculated TPA photocurrent assuming that the proportionality constant including coupling efficiency, TPA/SPA parameters, device volume etc. is known. The proportionality constant can be found simulating TPA response for incident CW light and by comparison it with measured previously PI curve and/or resonance characteristic. In the simulation described here SPA process is neglected assuming TPA process is dominant for simplicity. The function calculates average TPA photocurrent response for incident sequence of $sech^2$ pulses consisting of "one" bits only. The average response for incidence PRBS sequence operating at bit rate B is equivalent to the incidence sequence of "ones" operating at twice lower rate. Thus to simulate TPA photocurrent generated by e.g. 160 Gb/s incidence sequence, an incident train of ones operating at 80 GHz rate can be simulated. The pulse overlapping effects were modeled assuming power combining of pulses (no interference effects). The overlapping scheme used in the simulation can be viewed in Figure I-1. Initially FTL pulse was generated over a number of periods defined by Pnumb (Pnumb=3 in Figure I-1). Next the pulse broadening due to CD and cavity filtering was simulated and pulse fragments from neighboring periods were combined together non-coherently.

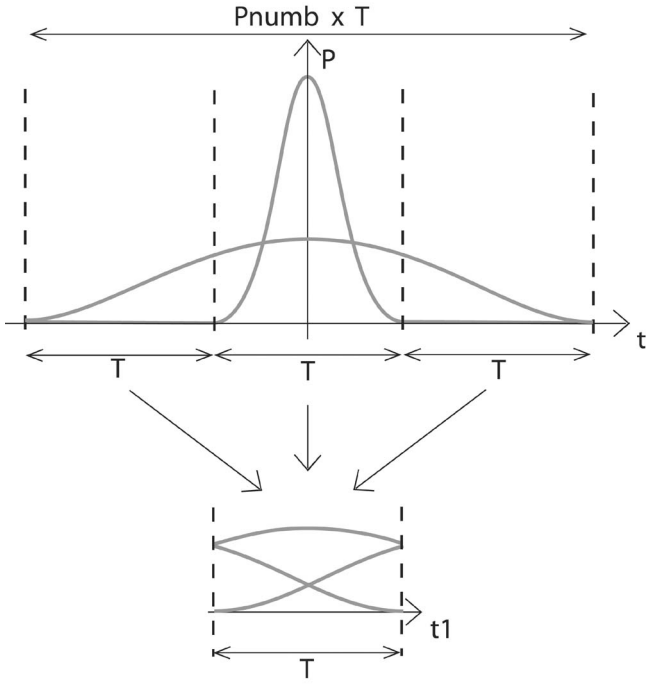

Figure I-1 pulse overlapping simulation scheme

A complete code of *itpafft* function is given below.

itpafft function:

```
--------------------------------------------------------------------------

function avitpa=itpafft(AD,TLFWHM,R,rate,incident_wavelength,Pnumb,det)

%input:*****************************************************************
% AD - 1st channel accumulated dispersion [ps/nm]
% TLFWHM - incident pulses (both channels) Fourier Transform Limited Full
Width at Half Maximum [ps]
% R - geometric average of mirrors reflectivities
% rate - incident sequence bit rate [GHz]
% incident_wavelength
% Pnumb - even number of neighboring pulses (to simulate pulse
overlapping)
% det frequency detuning between channels [GHz]
%************************************************************************

%constants
c=299792458;        %speed of light [m/s]
N=2^10;             %number of sampling points [-]

%Variables
bL=-AD*((incident_wavelength)^2/(2*pi*c))*10^3; % GVD*distance [ps^2/km]
df=rate*10^9/Pnumb; %frequency step [Hz]
T=1/df/Pnumb;       %period [s]
dt=T/N;             %temporal step [s]
fFSR=20*10^12;      %frequency Free Spectral Range [Hz]
detf=det*10^9;      %frequency spacing between channels [Hz]

%SCALES
t=(-Pnumb*N/2:Pnumb*N/2-1)*dt;      % time scale [s]
f=(-Pnumb*N/2:Pnumb*N/2-1)*df;      % frequency scale[Hz]

%sech incident%%%%%%%%%%%%%%%%%%%%%%%%%%%%%%%%%%%%%%%%%%%%%%%%%%%%%%%%%%
tal=(TLFWHM*10^-12)/(2*asech(1/sqrt(2))); %pulse width parameter [ps]
e=sech(t/tal);            %FTL Secant Hiperbolic pulse electric field
%%%%%%%%%%%%%%%%%%%%%%%%%%%%%%%%%%%%%%%%%%%%%%%%%%%%%%%%%%%%%%%%%%%%%%%%

FTF =1./(1+R/(1-R)*(1-exp(i*2*pi*f/fFSR)));
                                    %1st channel Field Transfer function

FTF2=1./(1+R/(1-R)*(1-exp(i*2*pi*(f-detf)/fFSR)));
                                    %2nd Channel Field transfer function

E=fftshift(fft(fftshift(e)));              % frequency representation
E1=E.*exp(i*bL*(2*pi*f*10^-12).^2/2).*FTF; % dispersion and filtering
e1=ifftshift(ifft(ifftshift(E1)));         % temporal representation
E2=E.*FTF2;                                % 2nd channel filtering
e2=ifftshift(ifft(ifftshift(E2)));         % temporal representation

combined_power=abs(e1).^2+abs(e2).^2;      %combined powers
```

```
%PULSE OVERLAPPING (see Fig I-1) %%%%%%%%%%%%%%%%
t1=(-N/2:N/2-1)*dt;       %new timescale
for a=1:N
    power(a)=combined_power(a);
    for b=1:Pnumb-1
        power(a)=power(a)+combined_power(b*N+a);
    end
end
%%%%%%%%%%%%%%%%%%%%%%%%%%%%%%%%%%%%%%%%%%%%%%%%%%%%

power=power/Pnumb;  % time averaging
const=3*10^5;       % constant describing device response

%OUTPUT: average TPA photocurrent
avitpa=const*sum((power).^2)*dt/T;
-------------------------------------------------------------------------
```

The above codes generate a plot of TPA photocurrent versus accumulated dispersion for two channel spacing as shown in Figure I-2. Large 10 THz (½ FSR) channel spacing corresponds to the case when only first channel is incident on the cavity and 640 GHz spacing correspond to the 4 times of the channel bandwidth.

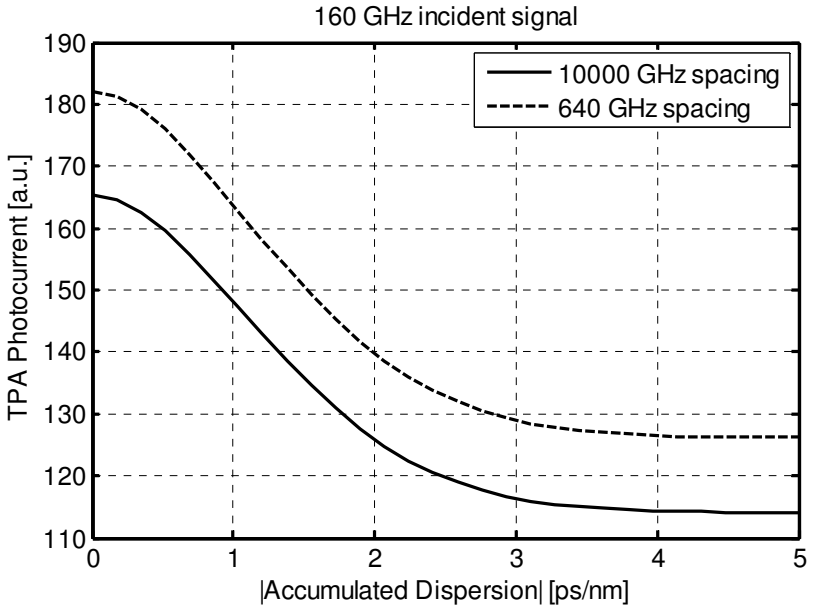

Figure I-2 Simulated with the example code TPA photocurrents versus incident accumulated dispersion for two channel spacing.

All the simulations carried out within this work are based on the same principle, described with the above example.

Appendix B. List of Publications Arising from this Work

Full text of key publications is included at the end of this section.

Referred journals:

K. Bondarczuk, P.J. Maguire, D. Reid, L.P. Barry, J. O'Dowd, W.H. Guo, M. Lynch, A.L. Bradley, J.F. Donegan, "Chromatic Dispersion Monitoring for high-speed WDM systems using Two-Photon Absorption in a Semiconductor Microcavity," *IEEE Journal of Quantum Electronics*, vol. 45, no.1, pp.90-99 2008

B.F. Kennedy, **K. Bondarczuk** and L.P. Barry, "Experimental analysis of phase conjugation properties of four-wave mixing in an SOA after probe broadening due to fibre dispersion," *Optics Communications*, vol. 281, no 8, pp. 2046-2049, 2008

B.F. Kennedy**, K. Bondarczuk**, L.P. Barry, "Pulse Pedestal Suppression Using Four-Wave Mixing in an SOA," *IEEE Photonics Technology Letters*, vol. 20, no.5, pp: 327 – 329, 2008

W.H. Guo, J. O'Dowd, E. Flood, T. Quinlan, M. Lynch, A.L. Bradley, J.F. Donegan, **K. Bondarczuk**, P.J. Maguire, L.P. Barry, "Suppression of Residual Single-Photon Absorption Relative to Two-Photon Absorption in High Finesse Planar Microcavities," *IEEE Photonics Technology Letters*, vol. 20, no.16, pp: 1426 - 1428, 2008

B.F. Kennedy, **K. Bondarczuk**, L.P Barry, "Pump-Probe Detuning Dependence of Four-Wave Mixing Pulse in an SOA," *IEEE Photonics Technology Letters*. vol. 19, pp: 2033-2036, 2007

K. Bondarczuk, P.J.Maguire, L.P.Barry, J.O'Dowd, W.H.Guo, M.Lynch, A.L.Bradley, J.F.Donegan, H.Folliot, "Chromatic Dispersion Monitoring of 80-Gb/s OTDM Data Signal via Two-Photon Absorption in a Semiconductor Microcavity," *IEEE Photonics Technology Letters,* vol. 1, pp: 21-23, 2007

Conference papers

L.P. Barry, **K. Bondarczuk**, K.J. Dexter, P.J. Maguire, D.A. Reid, J. O'Dowd, W.H. Guo, M. Lynch, A.L. Bradley, J.F. Donegan, "All-optical pulse processing for advanced photonic communication system", Invited paper, *IEEE 10th Anniversary International Conference on Transparent Optical Networks*, vol.2, pp. 92 – 95, 2008

K. Bondarczuk, P.J.Maguire, L.P.Barry, J.O'Dowd, W.H.Guo, M.Lynch, A.L.Bradley, J.F.Donegan, "High-Speed Chromatic Dispersion Monitoring of a Two-Channel WDM System using a single TPA Microcavity," *2008 Conference on Lasers and Electro-Optics (CLEO'08)*, San Jose, CA, USA, May 2008

K. Bondarczuk, K.J. Dexter, P.J. Maguire, D.A. Reid, L.P. Barry, J. O'Dowd, W.H. Guo, M.Lynch, A.L. Bradley, J.F. Donegan, "All-optical Chromatic Dispersion Monitoring and Multiple Access Interference Reduction via. Two-Photon Absorption," *China-Ireland International Conference on Information and Communications Technologies*, paper ID 295, Beijing, China, 2008

K. Bondarczuk, P.J.Maguire, L.P.Barry, J. O'Dowd, W.H. Guo, M.Lynch, A.L.Bradley, J.F.Donegan, H.Folliot, "Wavelength Tuneable Pulse Monitoring Using a Two-Photon-Absorption Microcavity," *in Conference on Lasers and Electro-Optics (CLEO'07)*, Munich, Germany, 2007

K. Bondarczuk, P.J.Maguire, L.P.Barry, J. O'Dowd, W.H. Guo, M.Lynch, A.L.Bradley, J.F.Donegan, H.Folliot, "All-optical signal processing via Two-Photon Absorption in a semiconductor micro-cavity," *IX International Workshops on Nonlinear Optics Applications,* 2007

B.F. Kennedy, **K. Bondarczuk**, L.P. Barry, "Experimental Analysis of Four-Wave Mixing in a Semiconductor Optical Amplifier Using Frequency Resolved Optical Gating," *IEEE 9th International Conference on Transparent Optical Networks*, vol.4, pp.263-266, 2007

K. Bondarczuk, P.J. Maguire, L.P.Barry, J. O'Dowd, W.H. Guo, M. Lynch, A.L. Bradley, J.F. Donegan, H. Folliot, "Nonlinear all-optical signal processing via Two-Photon Absorption semiconductor microcavity," *in Photonics Ireland Conference,* 2007

P.J. Maguire, **K. Bondarczuk**, L.P. Barry, C. Tian, Z. Zhang, M. Ibsen, D.J. Richardson, P. Petropoulos, "Reduction of Multiple Access Interference in a DS-OCDMA System via Two-Photon Absorption," EEE/OSA *in Optical Fiber Communications Conference and Exhibit* (OFC2007), paper no. OVW6, Anaheim, California, USA, 25-29th March 2007

P.J.Maguire, **K.Bondarczuk**, L.P.barry, J.O'Dowd, W.H.Guo, M.Lynch, A.L.Bradley, J.F.Donegan and H.Folliot, "Dispersion Monitoring for High-Speed WDM Networks via Two-Photon Absorption in a Semiconductor Microcavity," *IEEE 8th International Conference on Transparent Optical Networks*, vol. 4, pp.138 – 141, 2006

This content has been removed due to third party copyright.

This content has been removed due to third party copyright.

This content has been removed due to third party copyright.

This content has been removed due to third party copyright.